

University of Alberta

Cyclic Deformation of an Epoxy Resin: Experiments and Constitutive Model Predictions

by

Xinghe Shen



A thesis submitted to the Faculty of Graduate Studies and Research in partial fulfillment of
the

requirements for the degree of Master of Science

Department of Mechanical Engineering

Edmonton, Alberta
Fall 2004



Library and
Archives Canada

Bibliothèque et
Archives Canada

Published Heritage
Branch

Direction du
Patrimoine de l'édition

395 Wellington Street
Ottawa ON K1A 0N4
Canada

395, rue Wellington
Ottawa ON K1A 0N4
Canada

Your file *Votre référence*

ISBN: 0-612-95853-1

Our file *Notre référence*

ISBN: 0-612-95853-1

The author has granted a non-exclusive license allowing the Library and Archives Canada to reproduce, loan, distribute or sell copies of this thesis in microform, paper or electronic formats.

L'auteur a accordé une licence non exclusive permettant à la Bibliothèque et Archives Canada de reproduire, prêter, distribuer ou vendre des copies de cette thèse sous la forme de microfiche/film, de reproduction sur papier ou sur format électronique.

The author retains ownership of the copyright in this thesis. Neither the thesis nor substantial extracts from it may be printed or otherwise reproduced without the author's permission.

L'auteur conserve la propriété du droit d'auteur qui protège cette thèse. Ni la thèse ni des extraits substantiels de celle-ci ne doivent être imprimés ou autrement reproduits sans son autorisation.

In compliance with the Canadian Privacy Act some supporting forms may have been removed from this thesis.

Conformément à la loi canadienne sur la protection de la vie privée, quelques formulaires secondaires ont été enlevés de cette thèse.

While these forms may be included in the document page count, their removal does not represent any loss of content from the thesis.

Bien que ces formulaires aient inclus dans la pagination, il n'y aura aucun contenu manquant.

Canada

Table of Contents

1. Introduction	1
1.1 Epoxy resin	3
1.2 Nonlinear viscoelastic and time-dependent behavior	5
1.2.1 Viscoelasticity, time-dependence and linearity	5
1.2.2 Experimental measurements	7
1.2.3 Temperature, physical aging and other considerations	10
1.3 Viscoelastic constitutive Modeling	12
1.4 Overview of the current study	15
Figures — Chapter 2	17
Bibliography	19
2. Uniaxial Cyclic Deformation Behavior of an Epoxy Polymer	
: Experimental Investigations	23
2.1 Introduction	23
2.2 Specimen and test set-up	26
2.3 Experimental procedure and test results	27
2.3.1 Cyclic tensile loading with various stress amplitudes	27
2.3.2 Strain recovery test	29
2.3.3 Stress rate effect	30
2.3.4 Compressive cyclic loading	30
2.3.5 Fully reversed cyclic loading	31
2.3.6 Strain controlled cyclic loading	32
2.4 Conclusions	33
Tables — Chapter 2	34
Figures — Chapter 2	35
Bibliography	48
3. Uniaxial Cyclic Deformation Behavior of an Epoxy Polymer	
: Predictions of Viscoelastic Constitutive Models	50
3.1 Introduction	50

3.2. Constitutive models	53
3.2.1. Deferential representation	53
3.2.2 Integral representation	56
3.2.3 Material parameters	57
3.3 Comparison of model predictions with experimental data	58
3.3.1 Uniaxial tensile loading/unloading test	58
3.3.2 Cyclic loading with different stress ranges	58
3.3.3 Accumulation and recovery of the ratcheting strain	59
3.3.4 The effect of loading rate	60
3.3.5 Anisotropy in tension and compression	60
3.3.6 Fully reversed cyclic loading	61
3.3.7 Strain controlled cycling with different strain amplitudes	61
3.4 Conclusions	62
Figures — Chapter 3	64
Bibliography	77

4. Biaxial Cyclic Deformation of an Epoxy Resin

: Experiments and Constitutive Modeling	79
4.1 Introduction	79
4.2 Test set-up	81
4.2.1 Specimen and testing equipment	81
4.2.2 Experimental program and testing procedure	81
4.3 Test results	82
4.3.1 Proportional (equi-biaxial) cyclic loading under strain-control	82
4.3.2 Proportional (equi-biaxial) cyclic loading under stress-control	84
4.3.3 Non-proportional quarter-circle sectorial cyclic loading under strain-control	85
4.3.4 Non-proportional quarter-circle sectorial cyclic loading under stress-control	86
4.4 Constitutive modeling and predictions	87
4.4.1 Description of constitutive model	87

4.4.2 Comparison with experimental data	89
4.5 Conclusions	92
Tables — Chapter 4	94
Figures — Chapter 4	95
Bibliography	112
5. Conclusions	114
Appendix	118

List of Tables

Table 2.1	Loading conditions of the uniaxial test program.	34
Table 4.1	Loading conditions of the biaxial cyclic test program.	94

List of Figures

Figure 1.1	Schematic representations of molecular structures.	17
Figure 1.2	Illustration of linear viscoelastic behavior of materials.	17
Figure 1.3	Creep and recovery curves at different stress levels.	18
Figure 1.4	Creep compliance curves at different stress levels.	18
Figure 2.1	Geometry of solid cylindrical specimen and end tabs.	35
Figure 2.2	Stress-strain loops for the applied stress range of 45 MPa with a mean stress of 22.5 MPa.	36
Figure 2.3	Stress-strain loops for the applied stress range of 55 MPa with a mean stress of 27.5 MPa.	37
Figure 2.4	Stress-strain loops for the applied stress range of 66 MPa with a mean stress of 33 MPa.	38
Figure 2.5	Cyclic creep and recovery of residual strain (a) stress-strain loops for the 20 cycles pre-loading (b) residual strain versus time after 20 cycles of preloading.	39
Figure 2.6	Stress-strain loops for a faster loading rate of 24 MPa/s with the applied stress range of 55 MPa and a mean stress of 27.5 MPa.	41
Figure 2.7	Stress-strain loops for a compressive cyclic loading with the applied stress range of 55 MPa and a mean stress of 27.5 MPa.	42
Figure 2.8	Stress-strain loops for a fully reversed cyclic loading with the stress amplitude of 60 MPa.	43
Figure 2.9	Stress-strain loops for a fully reversed cyclic loading with the stress amplitude of 38 MPa.	44

Figure 2.10	Stress-strain loops for the applied strain range of 3% with a mean strain of 1.5%.	45
Figure 2.11	Stress-strain loops for the applied strain range of 1.5% with a mean strain of 0.75%.	46
Figure 2.12	Mean stress versus the number of cycles for the applied strain range of 3% with a mean strain of 1.5%.	47
Figure 3.1	Uniaxial representation of the differential model: combination of an elastic spring and a number of Kelvin (Voigt) elements in series.	64
Figure 3.2	Schematic representation of a current memory surface and the loading/unloading criterion.	65
Figure 3.3	Creep and recovery curves at different stress levels (adopted from Hu <i>et al.</i> [17]).	66
Figure 3.4	A comparison between the experimental result and the predicted uniaxial loading-unloading curves.	67
Figure 3.5	Stress-strain responses to a cyclic loading with a stress range of 45 MPa and a mean stress of 22.5 MPa (a) test data, (b) differential model predictions and (c) integral model predictions.	68
Figure 3.6	Stress-strain responses to a cyclic loading with a stress range of 55 MPa and a mean stress of 27.5 MPa (a) test data, (b) differential model predictions and (c) integral model predictions.	69
Figure 3.7	Stress-strain curves for 20 cycles of <i>preloading</i> under a cyclic stress with a maximum of 60 MPa and a mean stress of 30 MPa test data, (b) differential model predictions and (c) integral model predictions.	70

Figure 3.8	Ratcheting <i>strain recovery</i> after 20 cycles of preloading (a) test data, (b) differential model predictions and (c) integral model predictions.	71
Figure 3.9	Stress-strain curves of stress-controlled test with a maximum applied stress of 55 MPa with a mean stress of 27.5 MPa and a stress rate of 24 MPa/s (a) test data, (b) differential model predictions and (c) integral model predictions.	72
Figure 3.10	Stress-strain curves for a <i>compressive</i> cyclic loading with a stress range of 55 MPa and a mean stress of 27.5 MPa (a) test data, (b) differential model predictions and (c) integral model predictions.	73
Figure 3.11	Stress-strain curves for a <i>fully reversed</i> cyclic loading with stress amplitude of 60 MPa (a) test data, (b) differential model predictions and (c) integral model predictions.	74
Figure 3.12	Stress-strain curves for a <i>strain-controlled</i> test with a maximum strain of 3% and a mean strain of 1.5% (a) test data, (b) differential model predictions and (c) integral model predictions.	75
Figure 3.13	Stress-strain curves for a <i>strain-controlled</i> test with a maximum strain of 1.5% and a mean strain of 0.75% (a) test data, (b) differential model predictions and (c) integral model predictions.	76
Figure 4.1	Geometry of tubular specimen with aluminum end tabs.	95
Figure 4.2	Non-proportional loading paths and the corresponding input signals for axial and hoop directions: (a) quarter-circle sectorial cyclic loading path, (b) Axial input signal wave and (c) Hoop input signal wave.	96

Figure 4.3 Strain-controlled proportional (equi-biaxial) cyclic loading with strain range of $\Delta\varepsilon_a = \Delta\varepsilon_h = 1.5\%$: (a) experimental axial stress-strain response, (b) experimental hoop stress-strain response, (c) predicted axial stress-strain response and (d) predicted hoop stress-strain response. 97

Figure 4.4 Strain-controlled proportional (equi-biaxial) cyclic loading with strain range of $\Delta\varepsilon_a = \Delta\varepsilon_h = 3\%$: (a) experimental axial stress-strain response, (b) experimental hoop stress-strain response, (c) predicted axial stress-strain response and (d) predicted hoop stress-strain response. 98

Figure 4.5 The first and the fifteenth stress-strain loops of the strain-controlled proportional (equi-biaxial) cyclic loading with strain range of $\Delta\varepsilon_a = \Delta\varepsilon_h = 3\%$: (a) experimental axial stress-strain loops, (b) experimental hoop stress-strain loops, (c) predicted axial stress-strain loops and (d) predicted hoop stress-strain loops. 99

Figure 4.6 Mean stress relaxation vs. number of cycles for the strain-controlled proportional (equi-biaxial) cyclic loading with strain range of $\Delta\varepsilon_a = \Delta\varepsilon_h = 3\%$. Asterisk solid line: axial mean stress relaxation. Circle solid line: hoop mean stress relaxation. 100

Figure 4.7 Stress-controlled proportional (equi-biaxial) cyclic loading with stress range of $\Delta\sigma_a = \Delta\sigma_h = 40MPa$: (a) experimental axial stress-strain response, (b) experimental hoop stress-strain response, (c) predicted axial stress-strain response and (d) predicted hoop stress-strain response. 101

101

Figure 4.8 Stress-controlled proportional (equi-biaxial) cyclic loading with stress range of $\Delta\sigma_a = \Delta\sigma_h = 60MPa$: (a) experimental axial stress-strain response, (b) experimental hoop stress-strain response, (c) predicted axial stress-strain response and (d) predicted hoop stress-strain response.

102

Figure 4.9 The first, the sixtieth and the seventieth hysteresis loops of stress-controlled proportional (equi-biaxial) cyclic loading with stress range of $\Delta\sigma_a = \Delta\sigma_h = 60MPa$: (a) experimental axial stress-strain loops, (b) experimental hoop stress-strain loops, (c) predicted axial stress-strain loops and (d) predicted hoop stress-strain loops.

103

Figure 4.10 Strain-controlled non-proportional quarter-circle sectorial cyclic loading with strain range of $\Delta\varepsilon_a = \Delta\varepsilon_h = 1.5\%$: (a) experimental axial stress-strain response, (b) experimental hoop stress-strain response, (c) predicted axial stress-strain response and (d) predicted hoop stress-strain response.

104

Figure 4.11 Strain-controlled non-proportional quarter-circle sectorial cyclic loading with strain range of $\Delta\varepsilon_a = \Delta\varepsilon_h = 3\%$: (a) experimental axial stress-strain response, (b) experimental hoop stress-strain response, (c) predicted axial stress-strain response and (d) predicted hoop stress-strain response.

105

Figure 4.12 The first and the twenty-fifth hysteresis loops of strain-controlled non-proportional quarter-circle sectorial cyclic loading with strain range of $\Delta\varepsilon_a = \Delta\varepsilon_h = 3\%$: (a) experimental axial stress-strain loops, (b)

experimental hoop stress-strain loops, (c) predicted axial stress-strain loops and (d) predicted hoop stress-strain loops. 106

Figure 4.13 Strain-controlled non-proportional quarter-circle sectorial cyclic loading with strain range of $\Delta\varepsilon_a = \Delta\varepsilon_h = 1.5\%$: (a) experimental cyclic strain path, (b) experimental stress response and (c) predicted stress response. 107

Figure 4.14 Stress-controlled non-proportional quarter-circle sectorial cyclic loading with stress range of $\Delta\sigma_a = \Delta\sigma_h = 40MPa$: (a) experimental axial stress-strain response, (b) experimental hoop stress-strain response, (c) predicted axial stress-strain response and (d) predicted hoop stress-strain response. 108

Figure 4.15 Stress-controlled non-proportional quarter-circle sectorial cyclic loading with stress range of $\Delta\sigma_a = \Delta\sigma_h = 60MPa$: (a) experimental axial stress-strain response, (b) experimental hoop stress-strain response and (c) predicted axial stress-strain response, (d) predicted hoop stress-strain response. 109

Figure 4.16 Stress-controlled non-proportional quarter-circle sectorial cyclic loading with stress range of $\Delta\sigma_a = \Delta\sigma_h = 40MPa$: (a) experimental cyclic stress path, (b) experimental strain response and (c) predicted strain response. 110

Figure 4.17 Schematic representations of a current memory surface and the loading/unloading criterion. 111

Chapter 1

Introduction

Composites are material forms which consist of two or more constituents. The constituents are combined in such a way that they keep their individual physical states and are not soluble in each other and they do not form a new chemical compound. The most common composite materials are polymer matrix composites. They consist of a polymer as matrix (e.g., epoxy, polyester) and thin-diameter fibers as reinforcement (e.g., glass, carbon, aramid). Compared with conventional materials such as steel and aluminum, polymeric composites offer many advantages including high stiffness-to-weight ratio and high strength-to-weight ratio, superior corrosion resistance, faster assembly, design flexibility, etc. This has led to a wide and expanding application of polymeric composites in various industries, such as aircraft, aerospace, petrochemical and sporting goods. Some examples are: helicopter blades, antenna for the space station, pressure vessels for chemical plants, bicycles and golf clubs to mention a few [1].

However, the polymeric composites exhibit complex nonlinear viscoelastic and time-dependent properties. Experimental determination and theoretical characterization of these properties have attracted considerable attention. For example, a special symposium on time-dependent and nonlinear effects in polymers and composites was held recently, and the papers presented in the symposium appear in an ASTM special technical publication [2]. In polymeric composites viscoelasticity originates from the

polymer matrix because the fiber reinforcement is generally linear elastic, showing little time-dependent behavior. In addition, a successful stress or deformation analysis of polymeric composite usually requires accurate descriptions of the constitutive relation of each constituent. It is evident that to understand and to model the inelastic behavior of composites, one must understand and be able to model this behavior of the polymer matrix.

In the composite industry, polymer matrices include epoxy, unsaturated polyester, phenolic, acrylic, polyurethanes, etc. [3]. However, the most commonly used matrices in advanced polymer composites are epoxy resins. More than two thirds of the polymer matrices used in aerospace applications are epoxy based [1].

The material to be studied in the current investigation is Epon 826/Epi-Cure Curing Agent 9551, a bisphenol-A epoxy resin and a non-MDA (methylene dianiline) polyamine system, a product of Resolution Performance®. The liquid resin and the curing agent form low-viscosity, easy-to-process system which is suitable for high performance composite parts manufactured by filament winding or resin transfer molding. This system provides good mechanical and thermal properties, such as high elongation and toughness even at low temperature, low moisture sensitivity and good resistance to chemical erosion [4]. Because of these, this epoxy resin system has been selected and used as polymer matrix for fiber reinforced composites in the Advanced Composite Materials Engineering Group (ACME) at the University of Alberta.

The current research focuses on the cyclic deformation behavior of the aforementioned epoxy resin and on the viscoelastic constitutive model predictions. To get an overall picture of the research background, the following three sub-sections are

devoted to epoxy polymers (structures and properties); the nonlinear viscoelastic, time-dependant behavior; and viscoelastic constitutive modeling. Previous investigations on these issues are reviewed where necessary and work to be done is pointed out. The objectives and scope of the current study are outlined in the fourth sub-section.

1.1 Epoxy Resin

In a broad sense, the term epoxy refers to a chemical group consisting of an oxygen atom bonded with two carbon atoms already united in some other way. Reaction of these resins with a variety of curing agents leads to highly cross-linked plastics [5]. Although there are a variety of epoxies, approximately 75% of the epoxy resins currently used worldwide is derived from the diglycidyl ether of bisphenol A (DGEBA). This market dominance of epoxy resins is a result of a combination of their low cost and adequate-to-superior performance in many applications [4].

Polymers may be divided into four groups according to the structure of their molecular chains: linear polymers in which the mers are joined together end to end in single chains; branched polymers in which side-branch chains are connected to the main ones; crosslinked polymers in which adjacent linear chains are joined one to another at various positions by covalent bonds, and network polymers where multi-functional mer units form three-dimensional networks. Epoxies belong to the network group. The schematic diagram of the molecular structure of each type is illustrated in Fig. 1.1.

One important factor that influences the mechanical and thermal properties of polymers is the arrangement of molecular chains, for example, polymer crystallinity. Crystallinity refers to the packing of atomic (molecular) chains so as to produce an

ordered atomic (molecular) array. The degree of polymer crystallinity may range from completely amorphous to almost entirely crystalline. Usually, linear polymer like polyethylene could be crystalline because the linear molecular chains have no restrictions to prevent their alignment, whereas the network polymers such as epoxy are almost totally amorphous due to the complex irregular, random and three-dimensional entanglement of molecular chains. Therefore, epoxy polymers show isotropic properties.

According to their mechanical response at elevated temperatures, polymers may also be divided into two categories: thermosets and thermoplastics. Thermoset polymers are insoluble and infusible after cure, while thermoplastics can be formed and reformed at high temperatures. Epoxy is a typical thermosetting polymer. Once cured it becomes a permanently hard solid and does not soften upon subsequent heating. This could be attributed to its network molecular structures, where the chains are rigidly joined by strong covalent bonds. Once the atomic bonds are broken, they cannot be reformed.

The molecular characteristics, such as the chemical composition, molecular chain structure and chain arrangement, give epoxy resin properties superior to other polymers as engineering materials. One of the most advantageous properties of epoxy resins is their low shrinkage during cure. Low shrinkage rate minimize the tendency of gaining large shear stresses of the bond between epoxy and its reinforcement that otherwise would weaken the mechanical structures. Another unique property of epoxy is the high adhesive strengths. Because of the chemical makeup, chiefly the presence of polar hydroxyl and ether groups, the epoxy resins are excellent adhesives. The resins cure with low shrinkage, so that the various surface contacts set up between the liquid epoxy-resin formulation and the adherents are not disturbed during cure. Owing to this,

epoxy resins have been widely used as adhesives in structural application in addition to the matrix of advanced composite components [6].

1.2 Nonlinear Viscoelastic and Time-dependant Behavior

1.2.1 Viscoelasticity, Time-dependence and Linearity

Viscoelasticity has been an active research field for more than five decades. This research endeavor has been mainly stimulated by the vast types and quantities of the polymeric materials utilized in various applications. The experimental characterizations and development of viscoelastic theories have been documented in several treatises, see, e.g. [7-11]. These comprehensive works are the main references of this section.

For a pure elastic material, the mechanical behavior is described by the Hooke's law, i.e. stress is always directly proportional to strain in small deformations but independent of the rate of strain. The energy of deformation is completely stored and can be recovered in its entirety upon removal of the stress. In contrast, for a totally viscous material, in accordance with Newton's law of viscosity, the stress is proportional to the rate of strain but independent of the strain itself. The energy of deformation is instantly and completely dissipated and none of it can be recovered. Viscoelastic materials, as the name implies, respond to external excitations (force or deformation) in a manner intermediate between the behavior of elastic solid and viscous liquid. Some of the energy input is stored and can be recovered, some is dissipated as heat.

The characteristic feature of viscoelastic behavior is the time dependence evinced by the mechanical properties of a material. The constitutive equations of these

materials must include time as a variable in addition to the stress and strain variables. Even under a simple loading program such as a creep test, the shape of the strain-time curve may be rather complicated. Since time cannot be kept constant, reversed or eliminated during an experiment, the experimental study of the mechanical behavior of such materials is much more difficult than the study of time-independent materials [7].

The material is said to be linearly viscoelastic if stress is proportional to strain at a given time, and the linear superposition principle holds. In mathematical representations:

$$\varepsilon[c\sigma(t)] = c\varepsilon[\sigma(t)] \quad (1.1)$$

$$\varepsilon[\sigma_1(t) + \sigma_2(t - t_1)] = \varepsilon[\sigma_1(t)] + \varepsilon[\sigma_2(t - t_1)] \quad (1.2)$$

where ε and σ are the strain output and stress input, respectively, and c is a constant. Equation (1.1) states that the strain response to a stress input $c\sigma(t)$ equals the scalar c times the strain output due to a stress input $\sigma(t)$; Equation (1.2) states that the strain output due to the combination of two arbitrary but different stress inputs applied at different times, $\varepsilon[\sigma_1(t) + \sigma_2(t - t_1)]$, equals the sum of the strain outputs resulting from $\sigma_1(t)$ and $\sigma_2(t - t_1)$ each acting separately [7]. These two requirements are illustrated in Figs. 1.2 (a) and 1.2 (b).

Although the linear theory of viscoelasticity is well-developed and well-documented, see, e.g. treatise [11], it is valid only in the limit of small ranges of variables, i.e. stress, strain, time, temperature. Over large ranges of some variables, the polymeric material would exhibit nonlinear response. The linear response range is often small compared to the total range available prior to fracture or yield. In fact, some

polymers even do not show linear behavior, nonlinearity begins as early as the stress is applied [12-13]. For an efficient design of structures or components made of these materials, nonlinear material behavior must be accounted for.

1.2.2 Experimental Measurements

Experimental tests are essential in characterization of material properties. From measurements of viscoelastic properties, information can be obtained about the nature of the mechanical behavior for a given polymer. In general, the most commonly employed and most important means of experiments for viscoelastic material characterization include: step responses (creep or relaxation), slope responses (constant stressing or straining), dynamic responses (oscillating excitation) and repeated excitations (periodic, cumulative non-cyclic excitation or cyclic tests), cf. [14].

Step responses are obtained by applying a constant strain, ε_0 or a constant stress, σ_0 , respectively. They are also commonly known as creep (slow continuous deformation under constant stress) and relaxation (gradual decreasing stress under constant strain). Creep and relaxation tests provide the simplest and most direct means of obtaining the time-dependent properties involved in viscoelastic materials. Experimental data of these tests are often used to evaluate material constants or functions in many viscoelastic constitutive models, see, e.g. [15-16]

Following an experimental program advocated by Tuner [17-18], Hu et al. [16] carried out a series of creep tests at different stress levels to investigate the nonlinear viscoelastic behavior of the Epon 826 system that is also the material under current

study. Their test results are depicted in Fig. 1.3, which show a typical time-dependent viscoelastic behavior for this material. Specifically, the creep strains increase continuously with a decreasing rate. At low stress levels (less than 20 MPa) creep strains are relatively small, but they increase appreciably at higher stress levels. If, following load removal, a measurable portion of the deformation does not vanish after a long period of time, the deformation is commonly called viscoplastic. The recovery curves of this epoxy system show a complete recovery of strains, signifying a viscoelastic material without exhibiting viscoplasticity.

The creep data can also be converted to yield compliance curves in order to determine the linear range beyond which non-linear theory should apply for a more accurate constitutive description. The creep compliance, $D(\sigma_0, t)$, is defined as the ratio of creep strain, $\varepsilon_a(t)$, to the constant stress, σ_0 , i.e. $D(\sigma_0, t) = \varepsilon_a(t) / \sigma_0$. From the compliance curves shown in Fig. 1.4, the rough boundary between linear (where linear theory holds) and nonlinear could be approximately 20MPa. Below this stress level, the compliance curves collapse onto one, manifesting a linear behavior. For the stress levels higher than 20 MPa, the creep compliance curves are distinct from each other. This signifies a nonlinear behavior since the linear Eq. (1.1) does not hold any more.

Slope responses refer to the response to the imposition of a constant rate straining or stressing [19-20]. In general, the stress level would increase with the increase of strain rate. This type of experiments was also performed on Epon 826 resin

by Hu et al., and the stress-strain curves to failure with various strain rates under tensile, compressive, or shear loading can be found in reference [16].

Dynamic responses are commonly generated to study viscoelastic behavior and material response subject to impact or very high rate deformation. The responses are elicited by the imposition of sinusoidally oscillating excitations. Dynamic modulus values measured using such perturbations are functions of the frequency rather than time. For a viscoelastic body, upon reaching a steady state, the excitation (input) is not exactly in phase with the response (output), as it would be for a perfectly elastic solid. Neither they are 90° out of phase, as it would be for a perfectly viscous liquid. The output response falls in between $0-90^\circ$ phase angles. Some of the energy input is stored and recovered in each cycle, and the remaining is dissipated as heat and initiation of damage [8]. For different frequencies, different mechanical responses can be obtained and the frequency-dependence is actually a reflection of time-dependent behavior of viscoelasticity [21]. Another type of dynamic responses are generated by impact loading using a split Hopkinson pressure bar to apply a strain rate as high as over $10^3 s^{-1}$. Such experimental studies on Epon 828/T-403 have been performed by Chen et al. [20, 22]. This type of tests examines the material response over a very short time in millisecond which may be of practical importance, such as aircraft/automobile components subjected to impact loading.

Cyclic tests are the major means to study the material response under repeated excitations. This type of experiments has practical significance, because the structural components in engineering applications are likely subjected to multiaxial stress state with complex loading histories and paths, and in many cases, loading is of a cyclic nature in their service life. Although there have been numerous papers published concerning the multiaxial cyclic loading behavior of metals and alloys [23-26], the influence of such a loading condition on polymers has not been fully investigated. Experimental investigations on polymer behavior under cyclic loading were reported in refs. [27-30]. However, almost all of these investigations were for uniaxial cyclic tests on thermoplastic polymers. To the best of the author's knowledge, experimental data on the cyclic deformation behavior of thermosetting polymers are not available in the open literature.

1.2.3 Temperature, Physical Aging and Other Considerations

The mechanical properties of viscoelastic materials are very sensitive to temperature changes [31]. It has been found that the time-temperature superposition principle satisfactorily accounts for the effect of temperature effect, such as WLF equations, see Ferry [8]. There is no widely accepted general theory of temperature effect on nonlinear viscoelastic behavior. Admittedly, the temperature variable is important; however, it is beyond the scope of the current study, since this research is primarily concerned with material property under isothermal conditions.

Another important factor is physical aging, i.e. the dependence of viscoelastic behavior on the time that has elapsed since cooling to a fixed temperature [32]. After a

quick transition from a temperature above T_g to a temperature below T_g , the amorphous phase of polymers is no longer in thermodynamic equilibrium. In order to reach equilibrium, a continuous structural transformation takes place in the material. This transformation relates to the steady reduction of the free volume and to the decrease in molecular mobility, which leads to an increase of retardation times. This transformation would alter the mechanical properties such as stiffness, strength and toughness. In fact, physical aging has been reported as a thermodynamically reversible process: if the polymer is heated above T_g , it reaches thermodynamic equilibrium and all the previous ageing history will be erased [33]. Such experiments have been reported by some researchers. For example, the samples of amorphous PEN were first heated to 125° C for 30 min to thermally erase prior aging in the material [34].

Physical aging was encountered in this investigation. It was found that the length of time intervals between sample casting and specimen testing influenced the cyclic mechanical properties of this epoxy system. To stabilize the mechanical response of the material system, in this study each specimen was thermally activated at 80° C for 12 hours and then cooled in the oven for a day or two prior to testing. Through this thermal conditioning it was found that stable and repeatable test data can be obtained.

Other considerations such as multiaxial loading and loading paths effect of the Epon-826 system under quasi-static loading conditions were investigated by Hu et al., and the results can be found in ref. [16]. In this investigation, the multiaxial loading and loading path effect are studied in the cyclic loading regime, and they are addressed in detail in Chapter 4.

1.3 Viscoelastic Constitutive Modeling

As indicated before, although the linear viscoelastic theory is well developed, it is valid and applicable only to a small portion of the total range of epoxy polymer deformation. Thus it is necessary to account for the nonlinear behavior instead of assuming a linear approximation. There has been considerable effort to develop a general constitutive equation for nonlinear viscoelastic materials. Owing to the vast differences in polymer materials; hence, the nature of nonlinearity, a single nonlinear theory has not been developed which is capable of describing all polymers. In general, the fundamental idea of constructing a general or a specific nonlinear viscoelastic constitutive model may follow one of the three approaches: mechanical element models, thermodynamic formulations and free volume theory.

The first class is physically based and rheological in nature. It is also referred to as mechanical element analogue, because the model consists of certain combination of mechanical elements, i.e. springs and dashpots, which reproduce the viscoelastic response of real material systems. A representative model of this type is a differential formulation developed by Xia et al. [34]. In a uniaxial representation it can be viewed as a combination of one linear spring and several nonlinear Kelvin (Voigt) elements in series. The description of the nonlinear behavior in this model is achieved by letting E_i , the spring stiffness for the i -th Kelvin (Voigt) element, to be a function of the current 'equivalent' stress. The predictive capability of the model has been validated with various quasi-static multiaxial loading tests, see ref. [35]. In this study, the model is

employed to simulate the cyclic loading behavior, and the loading/unloading rule of the model is further modified based on the cyclic experimental observations. The detailed description of the nonlinear viscoelastic model and its simulation of cyclic tests will be given in the chapters to follow.

Another approach to characterizing nonlinear viscoelastic materials was based on the non-equilibrium thermodynamics. This approach has been found helpful in constructing constitutive relations and been investigated by many researchers, see, for example [36-39]. The free energy is expressed as a function of current values of strain (stress), temperature and other variables such as moisture and physical aging, which presumably could be incorporated through the shift factor in the reduced time. Among them, Shapery's single-integral constitutive model seems to be a more realistic and practical in applications, and has been applied with various degrees of success to some polymers, for example, see [40]. A modified Shapery single-integral model will be briefly reviewed in chapter 3 and the predictions by the model to the uniaxial cyclic loading will be compared to that of the differential model and test results.

Free volume is defined as the difference between the apparent volume of the material and that actually occupied by the atomic structure. It is identified with molecular packing irregularities, which are distributed non-homogeneously throughout the material. The nonlinear free volume approach is based on the concept that the "free volume" controls the mobility of polymer molecules and thus affects the inherent time scale of the material. Knauss-Emri constitutive model is the typical example [41-42]. The constitutive formulation is based on linear viscoelastic behavior for small

strains, except that the time scale is adjusted at any instant in time to the current volume state, thereby, introducing nonlinearity into the constitutive equation, i.e.

$$\sigma(t) = \int_{-\infty}^t E(\xi - \xi') \frac{\partial \varepsilon(\tau)}{\partial \tau} d\tau \quad (1.3)$$

where real times t and τ in linear viscoelastic theory (Boltzmann superposition integral) are replaced by the reduced times ξ and ξ' , which are related to the original real times t and τ by:

$$\xi(t) = \int_0^t \frac{ds}{a} \quad \text{and} \quad \xi'(\tau) = \int_0^\tau \frac{ds}{a} \quad (1.4)$$

The dependence of the volumetric effects of temperature [8], solvent concentration [43], mechanical pressure [44], stress-induced dilatation and distortion [45], and physical aging [46], which have all been shown to influence the time scale, can be attributed to the change of free volume, hence the free volume serves as a unifying parameter in describing the nonlinearity through the reduced time, i.e.

$$\log a = -\frac{B_d}{2.303 f_d} \left(\frac{\alpha_v \Delta T + \beta_v \Delta c + \delta \theta}{f_d + \alpha_v \Delta T + \beta_v \Delta c + \delta \theta} \right) - \frac{B_s}{2.303 f_s} \left(\frac{\varepsilon_{eff}}{f_s + \varepsilon_{eff}} \right) \quad (1.5)$$

where B_d and f_d are associated with dilatational effects and B_s and f_s are associated with distortional effect, f is the fractional free volume, α_v is the volumetric thermal expansion of the free volume, β_v is the volumetric expansion due to a change in moisture content, Δc and δ relates the change in free volume due to mechanical

volume changes, θ , resulting from hydrostatic stresses, and ε_{eff} account for distortional effect and defined by $\varepsilon_{eff} = \sqrt{2e_{ij}e_{ij}}/3$. The combination of Eqs. 1.3-1.5 constitute a modified free volume model proposed by Popelar and Liechti [45].

1.4 Objectives and Outline of the Present Study

The objective of the present study was two-fold: (a) to investigate the cyclic deformation behavior of the epoxy resin through a comprehensive experimental program, including uniaxial and multiaxial cyclic loadings; (b) to evaluate, verify and compare the predictive capabilities of viscoelastic constitutive models on the basis of the experimental data.

The uniaxial cyclic tests included stress- or strain-controlled cyclic loading with/without mean stress or mean strain at various amplitudes and loading rates. Experiments were also carried out to study the cyclic creep strain and anisotropy in cyclic tension and compression. These test results are presented and discussed in Chapter 2.

In Chapter 3, experimental data are used to evaluate the predictions by two nonlinear viscoelastic constitutive models, one in differential representation by Xia et al. [35], another being the modified Shapery's integral representation by Lai and Bakker [47]. Based on the cyclic test data and to suit more general cyclic loadings, the loading/unloading criterion and the switch rule of Xia's model were further modified

herein. Conclusions were drawn on the predictive capability of the two constitutive models.

An effort to investigate multiaxial cyclic deformation behavior and loading path effect is reported in Chapter 4. Biaxial (proportional and non-proportional) cyclic tests were performed. The focus of experiments is placed on the biaxial stress-strain response and their dependency on the load control mode, stress or strain range and loading path. The experimental data were used to validate Xia et al. constitutive model. The predictions of the model are compared with the test results.

Finally, general conclusions are given in Chapter 5.

This thesis is written in a paper-based format. Chapters 2, 3 and 4 each are each papers written and submitted to relevant journals recently.

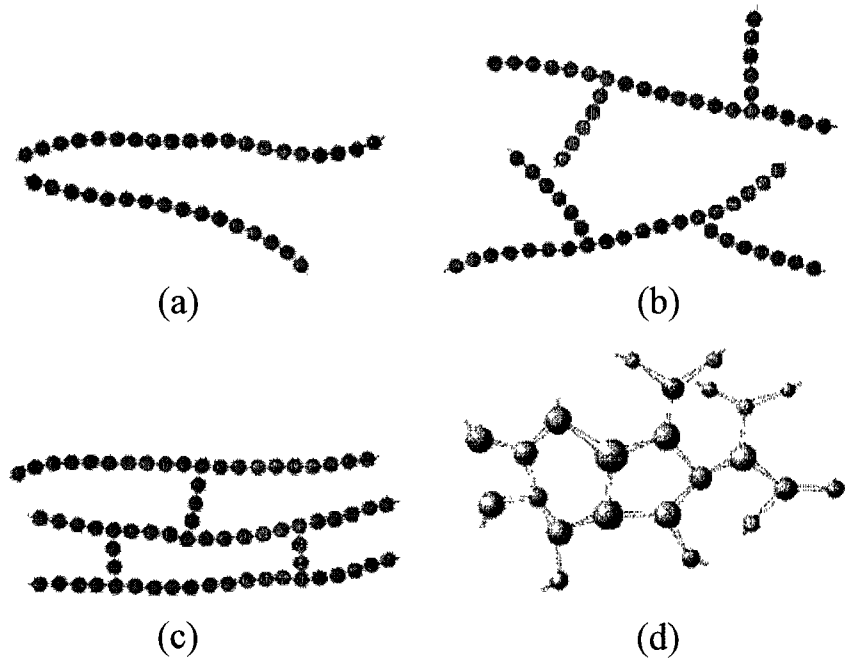


Figure 1.1 Schematic representations of molecular structures: (a) linear, (b) branched, (c) crosslinked and (d) network

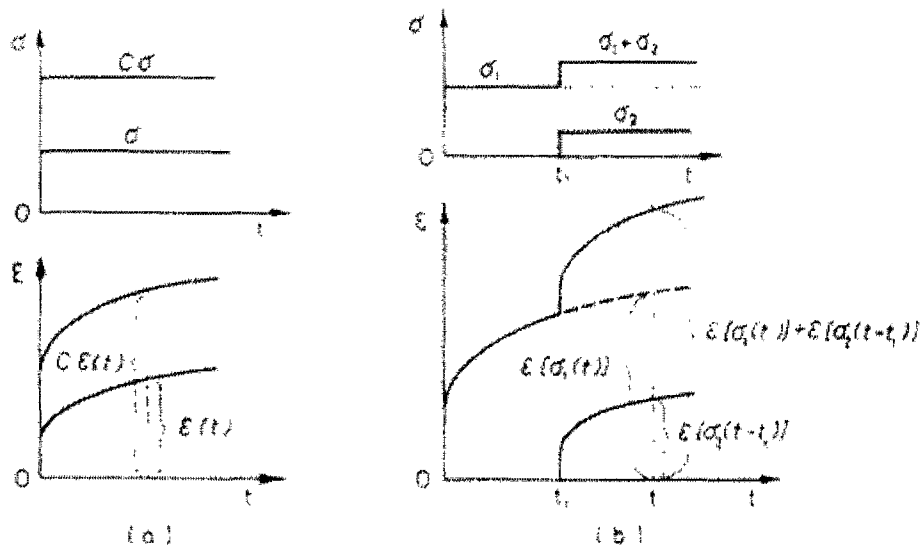


Figure 1.2 Illustration of linear viscoelastic behavior of materials
(adopted from Findley [7])

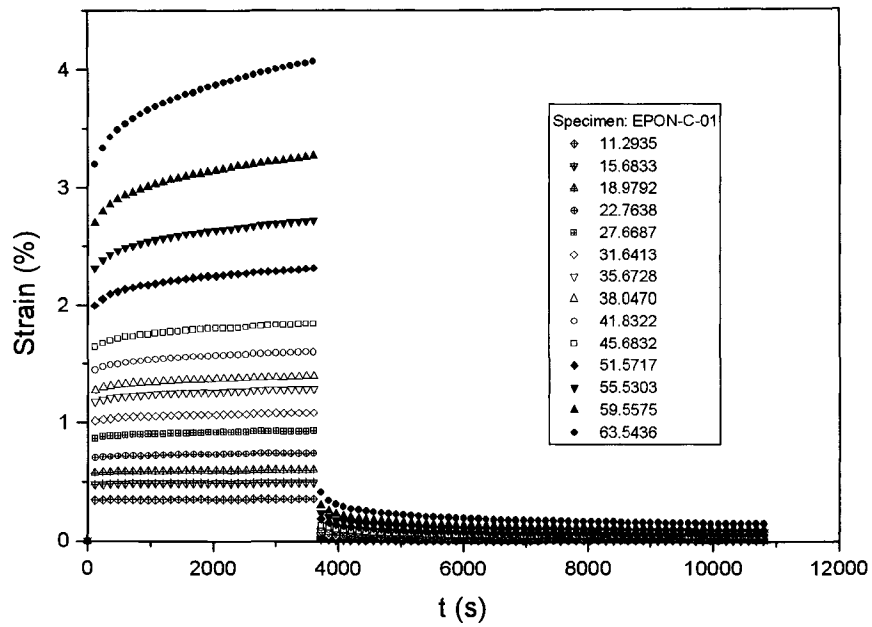


Figure 1.3 Creep and recovery curves at different stress levels (adopted from Hu et al. [16])

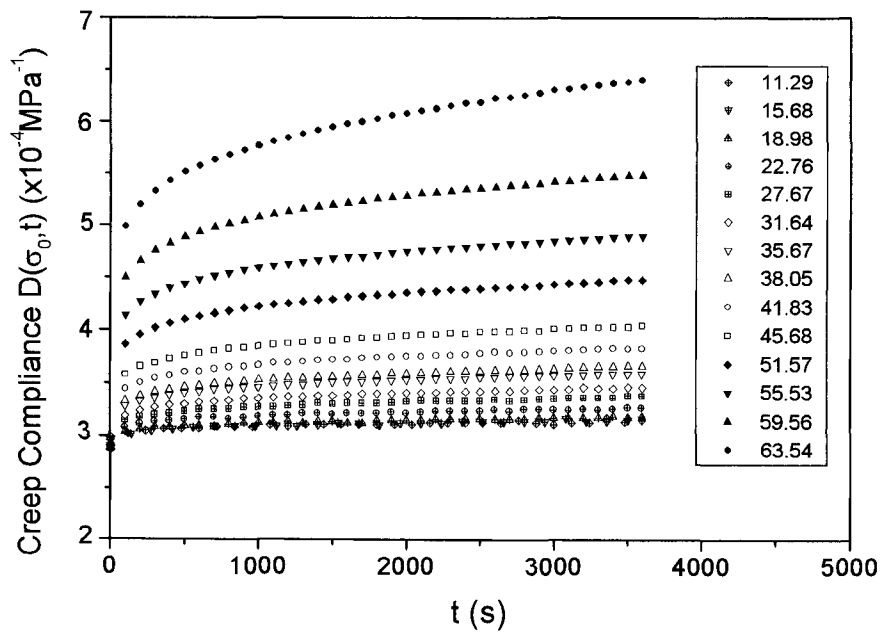


Figure 1.4 Creep compliance curves at different stress levels (adopted from Hu et al. [16])

Bibliography

1. A. K. Kaw, *Mechanics of composite materials*, CRC Press, 1997.
2. R. A. Schapery and C. T. Sun, editors, *Time dependent and nonlinear effects in polymers and composites*, ASTM STP 1357, 1998.
3. M. Biron, *Thermosets and composites: technical information for plastic users*, Oxford, New York, Elsevier, Chapter 6, 2004.
4. Y. Hu, *Multiaxial behavior and viscoelastic constitutive modeling of epoxy polymers*, Ph. D. dissertation, University of Alberta, 2002.
5. R. W. Ranney, *Epoxy resins and products: recent advances*, Park Ridge, N.J., Noyes Data Corp., 1977.
6. P. J. Moss, *Structural use of epoxy resin adhesives*, Wellington, N.Z. : Road Research Unit, National Roads Board, 1984.
7. W.N. Findley, J.S. Lai, and K. Onaran, *Creep and relaxation of nonlinear viscoelastic materials, with an introduction to linear viscoelasticity*, North-Holland, Amsterdam, 1976.
8. J.D. Ferry, *Viscoelastic Properties of Polymers*, 3rd ed., Wiley and Sons, New York, 1980
9. R. M. Christensen, *Theory of Viscoelasticity*, 2nd ed., Academic Press, New York, 1982
10. J. J. Aklonis and W. J. MacKnight, *Introduction to polymer Viscoelasticity*, 2nd ed., Wiley and Sons, New York, 1980
11. N. W. Tschoegl, *the Phenomenological theory of linear viscoelastic behavior*, Springer-Verlag, Heidelberg, 1989.
12. D.G. Fotheringham and B.W. Cherry, *The role of recovery forces in the deformation of linear polyethylene*, *J. Mater. Sci.*, **13**, 951 (1978).
13. J. Lai and A. Bakker, *Analysis of the non-linear creep of high-density polyethylene*, *Polymer*, **36**, 93 (1995)
14. N. W. Tschoegl, *Time dependence in material properties: an overview*, *Mech. of Time-dependent Mater.*, **1**, 3 (1997).
15. Y. C. Lou and R. A. Schapery, *Viscoelastic characterization of a nonlinear fiber-reinforced plastic*, *J. of Composite Mater.*, **5**, 208 (1971).

16. Y. Hu, Z. Xia, and F. Ellyin, Deformation behavior of an epoxy resin subject to multiaxial loadings, Part I: experimental investigations. *Polym. Eng. Sci.*, **43**, 721 (2003).
17. S. Turner, The strain response of plastics to complex stress histories, *Polym. Eng. & Sci.*, **6**, 306 (1966).
18. S. Turner, *Mechanical Testing of Plastics*, Longman, New York, 1973.
19. C.M. Bordonaro and E. Krempl, The effect of strain rate on the deformation and relaxation behavior of 6/6 nylon at room temperature, *Polym. Eng. & Sci.*, **32**, 1066 (1992).
20. W. Chen and B. Zhou, Constitutive behavior of Epon 828/T-403 at various strain rates, *Mech. of Time-dependent Mater.*, **1**, 103 (1998).
21. J.R. Fried, *Polymer science and technology*, Prentice-Hall, New Jersey, 1995.
22. W. Chen and X. Zhang, Dynamic response of Epon 28/T403 under multiaxial loading at various temperatures, *J. Eng. Mater. & Tech.*, **119**, 305 (1997).
23. Y. Jiang and H. Sehitoglu, Cyclic ratcheting of 1070 steel under multiaxial stress state. *Int. J. Plast.*, **10**, 579 (1994).
24. Z. Xia and F. Ellyin, Nonproportional multiaxial cyclic loading: experiments and constitutive modeling. *J. Appl. Mech.*, **58**, 317 (1991).
25. G. Meijer, Z. Xia and F. Ellyin, Biaxial cyclic analysis of $Al_2O_3/p - 6061 Al$ composite. *Acta mater.*, **45**, 3237 (1997).
26. F. Ellyin, *Fatigue Damage, Crack Growth, and Life Prediction*, Chapman & Hall, London, UK, (1997).
27. S. Rabinowitz and P. Beardmore, Cyclic deformation and fracture of polymers. *J. Mater. Sci.*, **9**, 81 (1974).
28. D. J. Kizypow and C. M. Rimnac, Cyclic steady state stress-strain behavior of UHMW polyethylene. *Biomaterials*, **21**, 2081 (2000).
29. T. Ariyama, Cyclic deformation and relaxation characteristics in polypropylene. *Polym. Eng. Sci.*, **33**, 18 (1993).
30. R. J. Scavuzzo, Oscillating stress on viscoelastic behavior of thermoplastic polymers. *J. Press. Vesel Tech.*, **122**, 386 (2000).

31. F. Schwarzl and A. J. Staverman, Time-temperature dependent of linear viscoelastic behavior, *J. of Appl. Physics*, **23** 838 (1952).
32. R. A. Schapery, Nonlinear viscoelastic solids. *Int. J. Solids & Structures*, **37**, 359 (2000).
33. I. D. Skrypnik, J. L. Spoormaker, and P. A. Kandacha, constitutive model for long-term behavior of polymers, in *Time dependent and nonlinear effects in polymers and composites*, ASTM STP 1357, R. A. Schapery and C. T. Sun, eds., (1998).
34. M. L. Cerrada, G. B. McKenna, Creep behavior in amorphous and semicrystalline PEN, in *Time dependent and nonlinear effects in polymers and composites*, ASTM STP 1357, R. A. Schapery and C. T. Sun, eds., 47 (1998).
35. Z. Xia, Y. Hu and F. Ellyin, Deformation behavior of an epoxy resin subject to multiaxial loadings. Part II: constitutive modeling and predictions. *Polym. Eng. Sci.*, **43**, 734 (2003).
36. R. A. Shapery, On the characterization of nonlinear viscoelastic materials. *Polym. Eng. Sci.*, **9**, 295 (1969).
37. R.A. Schapery, Nonlinear viscoelastic and viscoplastic constitutive equations based on thermodynamics, *Mech. Time-dependent Mater.*, **1**, 209 (1997).
38. K. C. Valanis, Thermodynamics of large viscoelastic deformations, *J. Math. Phys.* **45**, 179 (1966).
39. S. R. Lustig, R. M. Shay Jr, and J. M. Caruthers, Thermodynamic constitutive equations for materials with memory on a material time scale. *J. Rheol.* **40**, 69 (1996).
40. D. Peretz and Y. Weitsman, Nonlinear viscoelastic characterization of FM-73 adhesives, *J. Rheol.*, **26**, 245 (1982).
41. W.G. Knauss and I.J. Emri, Non-linear viscoelasticity based on free volume consideration, *Comput. & Struct*, **13**, 123 (1981).
42. W.G. Knauss and I.J. Emri, Volume change and the nonlinearly thermo-viscoelastic constitution of polymers, *Polym. Eng. Sci.*, **27**, 86 (1987).
43. W.G. Knauss and V.H. Kenner, On the hygrothermomechanical characterization of polyvinyl acetate, *J. Appl. Phys.*, **51**, 5131 (1980).
44. R. W. Fillers, and N. W. Tschoegl, Effect of pressure on mechanical-properties of polymers, *Tans. Soc. Rheol.*, **21**, 51 (1977).

-
45. C.F. Popelar and K.M. Liechti, Multiaxial nonlinear viscoelastic characterization and modeling of a structural adhesive, *J. Eng. Mate. & Tech.*, **119**, 205 (1997).
 46. L.C.E. Struik, *Physical aging in amorphous polymers and other materials*, Elsevier, Amsterdam, 1978
 47. J. Lai and A Bakker, 3-D schapery representation for non-linear viscoelasticity and finite element implementation, *Comput. Mech.*, **18**, 182 (1996).

Chapter 2

Uniaxial Cyclic Deformation Behavior of an Epoxy Polymer : Experimental Investigation

2.1 Introduction

Solid polymers are widely used in load bearing applications, both in the homogeneous state or as a matrix phase in fiber-reinforced polymeric composites. Polymers and plastics are typical materials with viscoelastic properties, and the majority of them exhibit complex nonlinear and time-dependent response prior to fracture. To facilitate the application of these materials in critical components, an adequate understanding of their deformation and failure behavior is a pre-requisite.

The material to be studied in this investigation is Epon 826/Epi-Cure Curing Agent 9551, a bisphenol-A epoxy resin and a non-MDA (methylene dianiline) polyamine system suitable for high performance composite parts manufactured by filament winding or resin transfer moulding. This epoxy system was chosen because it provides high strength, elongation and toughness, and therefore, is an appropriate matrix for high performance composite materials [1].

The deformation behavior of this epoxy resin when subjected to quasi-static multiaxial loading, was investigated experimentally in ref. [1]. The predictions by a nonlinear viscoelastic constitutive model recently developed by Xia et al. were found to be in good agreement with the test data [2]. However, the response of this epoxy resin

under cyclic loading has not been investigated. Experimental studies have indicated that the cyclic stress-strain behavior of polymers, as with most metals, is not the same as that of quasi-static loading [3]. It is also well recognized that crack initiation and accumulation in polymer matrix is usually the first form of damage process in composite structures. For example, as reported by Kaynak and Mat in [4], the cyclic damage development of composite tubes mostly initiates from matrix cracks. Hence the cyclic loading behavior of polymers is of practical significance and is an important consideration in the design of industrial products made of these materials.

Reported investigations on polymer behavior under cyclic loading are relatively few in the open literature. A brief review is provided as follows. Rabinowitz and Beardmore [3] studied the cyclic deformation and fracture of a variety of rigid polymers including polycarbonate, poly(methylmethacrylate) and nylon among others, through fully reversed uniaxial cyclic straining tests. They reported cyclic softening and a marked decrease in deformation resistance prior to crack formation of ductile thermoplastic polymers (e.g. polycarbonate). They also found that brittle or semi-brittle polymers are essentially stable in cyclic deformation and their fatigue resistance is strain amplitude sensitive. However, the cyclic deformation behavior of the thermoplastic polymers under other loading conditions, for instance, stress-controlled loading with or without mean stress, was not investigated. Kizypow and Rimnac [5] examined the stable cyclic stress-strain behavior of the ultra high molecular weight polyethylene (UHMWPE) and suggested a material constitutive relationship for finite element analyses of UHMWPE components by a modified stress-strain relationship. Nishitani and Yamashita [6] studied the cyclic deformation behavior of nonlinear

viscoelastic cellulose nitrate and found that the stress amplitude and the stress rate significantly affected the stress-strain curves. The cyclic hysteresis loops presented were those under stress-controlled with mean stress only. Extensive investigations on the cyclic deformation and stress relaxation response of polypropylene as well as the effects of strain rate, number of cycles, mean strain and strain amplitude on the constitutive curves can be found in refs. [7-8].

The literature survey revealed that experimental data on the cyclic deformation behavior of thermosetting polymers is rather limited. The dynamic properties (mainly the dynamic shear modulus) of an epoxy resin under oscillatory torsion with different frequencies, strain amplitudes and testing temperatures were reported in ref. [9]. Unfortunately, the constitutive stress-strain curves during the cyclic process were not presented.

It is the objective of this chapter to present experimental results of various uniaxial cyclic loading conditions of the Epon 826 / Epi-Cure 9551 epoxy system. Emphasis is placed on the evolution of the stress-strain hysteresis loops in the cyclic process, as well as on effects of amplitude, loading rate and mean stress/strain. Anisotropy behavior in tension and compression is also investigated. The results to be presented not only give an insight into the cyclic deformation behavior of the aforementioned epoxy resin, but also provide a data source for development and/or verification of constitutive models for epoxy polymers.

2.2 Specimen and Test Set-up

Epon 826 and the hardener were mixed with the ratio of 2.3:1 (volume) or 100:36 (weight), stirred thoroughly and poured into a plastic tubular mold. The sample was then cured for 2 hours at 50⁰C with subsequent post cure for 2.5 hours at 120⁰C and cooled to room temperature in the oven. The cast samples were then machined on a computer numerical controlled (CNC) lathe. Aluminum tabs were bonded to the specimen ends to insert the specimen into the gripping system of the testing machine. Figure 2.1 shows the geometry of the solid cylindrical specimen with the aluminum end tabs. The specimen geometry was designed based on the recommended low-cycle fatigue specimen by ASTM [10].

It was found that the length of time intervals between sample casting and specimen testing influenced the cyclic mechanical properties of this epoxy system, i.e. physical aging effect. Physical aging of polymers has been widely studied e.g. see ref. 11-14 among others. To stabilize the mechanical response of the material system, in this study, each specimen was thermally activated at 80⁰C for 12 hours and then cooled in the oven for a day or two prior to testing. Through this thermal conditioning it was found that stable and repeatable test data can be obtained.

All experiments were performed in a servo-controlled electro-hydraulic system, a modified MTS system. The system is capable of applying axial force and the internal/external differential pressure separately or simultaneously to apply either uniaxial or biaxial stress state on the specimen. Detailed description of the test system can be found in ref. [15]. The axial strain was measured with an axial extensometer. A triangular waveform was used for all the tests. The loading rates for the tests were

selected in the range that they allowed for the manifestation of the time-dependent behavior of the material yet avoided the excessive heating of the specimen during cycling. All the tests were conducted at room temperature under the laboratory environment. For each cyclic test, the stress-strain hysteresis loops were recorded for the initial 10 cycles after which they were recorded at each 10-cycle interval until specimen failure.

2.3 Experimental Procedure and Test Results

The loading conditions for each type of test are summarized in Table 2.1. Generally, two tests were carried for the same loading condition to ensure data reliability. The cyclic loading rates were chosen such that the applied strain rates were of the order of 10^{-4} per second for most of the tests and at a rate of two orders higher (10^{-2} s^{-1}) for the fast rate tests. Most of the cyclic tests were carried out until fracture of the specimens. Although small pieces of cloth were glued to the surface of the specimen to prevent damage caused by the extensometer knife edges, the location of fracture was mostly where the extensometer was mounted. Therefore, the recorded cycles to failure may not represent the actual fatigue life of the material.

2.3.1 Cyclic Tensile Loading with Various Stress Amplitudes

The stress amplitude effect on the stress-strain response was investigated through cyclic tensile loading with three different stress ranges, $\Delta\sigma = 45, 55$ and 66 MPa, respectively (stress amplitude = $\Delta\sigma / 2$). The stress rates were chosen to achieve

an approximately equivalent strain rate of $1.1 \times 10^{-4} \text{ s}^{-1}$ for the three tests. The stress-strain curves of these tests are shown in Figs. 2.2-2.4.

It is seen from Fig. 2 that at the maximum applied stress level of 45 MPa, the hysteresis loops are almost linear in shape throughout the test. The ratcheting deformation (cyclic creep) accumulates from the very beginning of cyclic loading. The data indicate that the ratcheting rate, or the ratcheting strain per cycle, decreases with the increasing number of cycles, and after about 300 cycles the ratcheting rate tends to zero and a saturated stress-strain response is attained. It was also noticed that during the entire cycling process, the slope of the elastic loading and unloading did not decrease appreciably, i.e. the stiffness reduction was very small. The specimen failed after 400 cycles.

Figure 3 shows the cyclic stress-strain curves for an applied stress range of 55 MPa. It is noted that initially the hysteresis loops exhibit some non-linear response. However, with the increase of number of cycles, the loops become slimmer and more linear. With the increasing cycles the ratcheting strain accumulates with a decreasing rate, and after about 220 cycles, a saturated stress-strain response is attained. Again only a small amount of stiffness reduction was observed. The number of cycles to failure was 250 cycles.

The nonlinear stress-strain response was more noticeable when the applied maximum stress was increased to 66 MPa, as depicted in Fig. 4. Due to the high cyclic stress amplitude, the specimen failed after only 10 cycles. It is seen that the ratcheting strain reached approximately 1% after 10 cycles. In contrast at the same number of cycles, the ratcheting strains were only 0.12% at the applied maximum stress of 45 MPa,

and 0.2% at that of 55MPa. In addition, neither a decreasing ratcheting rate nor saturated stress-strain response was observed during the test with the applied stress range of 66 MPa.

From the test results presented in Figs. 2.2-2.4, it is seen that the stress-strain response is amplitude dependent. The higher the cyclic stress amplitude, the higher is the nonlinearity of the stress-strain hysteresis loops. At low stress amplitudes, the accumulated ratcheting strain and the hysteresis loops reach a stable state while at a large amplitude, e.g. $\Delta\sigma/2 = 33$ MPa, a significant amount of the ratcheting strain accumulates and it contributes to damage initiation and propagation.

2.3.2 Strain Recovery Tests

In a stress-controlled cycling with mean stress, the maximum strain increases with the increasing numbers of cycles. This process of a continuous increase in strain is called cyclic creep (or ratcheting strain). To study the nature of the cyclic creep strain, a specimen was cyclically loaded with a maximum stress of 60 MPa and a loading rate of 0.24 MPa/s for 20 cycles. Upon completion of the 20th cycle of preloading, the load was removed and the residual strain recovery was monitored. The recovery process was recorded for the initial 3 hours using a digitized oscilloscope (Tektronix TDS 410A), and subsequently monitored every hour up to 24 hours. Figure 2.5 shows the experimental data of the cyclic preloading and the subsequent residual strain recovery.

It is seen that the accumulated ratcheting strain reached 0.46% after 20 cycles of preloading as shown in Fig. 2.5 (a). The subsequent residual strain vs. time curve in Figure 2.5 (b) indicates that the accumulated residual strain is recovered at a continuously

decreasing rate. After 24 hours of recovery, the residual strain reached a small value of 0.08% and it was still decreasing at a very slow rate. This time-dependent full recovery of deformation following load removal confirms that the cyclic creep strain is a viscous strain and the material shows a typical viscoelastic behavior.

2.3.3 Stress Rate Effect

A further cyclic test with a maximum stress of 55 MPa and a fast loading rate of 24 MPa/s was performed to investigate the stress rate effect. The stress-strain curves for this case are depicted in Fig. 2.6. When compared with Fig. 2.3, it is noted that at the higher stress rate, the stress-strain loops have less nonlinearity and are stable during the entire cyclic process. The ratcheting strain accumulated with a decreasing rate. A saturated stress-strain state was attained after about 200 cycles, which is comparable to that with a stress rate of two orders of magnitude less, i.e. 0.24 MPa/s. However, the amount of ratcheting after attainment of cyclic stable state was considerably different, i.e. with a higher loading rate of 24 MPa/s, the cyclic stable ratcheting strain was 0.18% in comparison to that of 0.61% residual strain with a lower loading rate of 0.24 MPa/s.

2.3.4 Compressive Cyclic Loading

It has been noted that for many polymers, the tensile and compressive creeps are not necessarily identical, and in general the resistance to creep in uniaxial compression is superior to that in tension [16-18]. Hence, the tensile cyclic loading may not reflect the compressive cyclic behavior of this epoxy resin. A further compressive cyclic test at the applied stress range of $\Delta\sigma = 55$ MPa with a stress rate of 0.24 MPa/s was performed

to compare the response of the epoxy polymer in tension and compression. Figure 2.7 shows that ratcheting strain in compression increases with a decreasing rate, and a saturated state is reached after 210 cycles, which is comparable with that of the tensile cyclic test shown in Fig. 2.3. However, the material shows a superior cyclic creep resistance in compression to that in tension. It was noted that the final ratcheting strain in this case was only 0.24%, which is nearly one third of the residual strain of 0.64% recorded in the case of tensile cycling at the same stress amplitude, loading rate and number of cycle $N=240$. It was also found that the elastic modulus (linear slope of the stress-strain curves) was slightly higher than that obtained from the tensile cyclic loading. At the first cycle $N=1$, the elastic modulus was $E=2,760$ MPa in the tensile cycling, and $E=2,840$ MPa in the compressive cyclic loading. At the stable state, i.e. $N=220$, $E=2,650$ MPa in tensile cycling compared to $E=2739$ MPa in compressive loading.

2.3.5 Fully Reversed Cyclic Loading

Figures 2.8 and 2.9 depict the stress-strain curves under fully reversed stressing with different stress amplitudes of 60 MPa and 38 MPa, respectively. It was observed that under the stress amplitude of 60 MPa the ratcheting in tension was evident and noticeable, while ratcheting in compression appeared to be insignificant during the recorded 20 cycles. The reason for this could be attributed to the anisotropic behavior of the material in tension and compression as demonstrated in the previous cyclic tension and cyclic compression tests. The stress-strain curves assume nonlinear shape, especially in tension. Due to the high stress level, the specimen failed after relatively

few cycles, $N=30$. In the case of small stress amplitude, Fig. 2.9, a less nonlinear stress-strain response was observed throughout the cycling process. The specimen lasted for over 400 cycles, and a small amount of ratcheting occurred in both tension and compression while the ratcheting strain in tension was higher than that in compression.

2.3.5 Strain Controlled Cyclic Loading

Further tests were carried out under strain control with two different strain amplitudes. Again, the test frequencies were chosen to yield an equal strain rate for the two tests ($1.2 \times 10^{-4} \text{ s}^{-1}$). Figures 2.10 and 2.11 show the test results with two strain ranges respectively. For the cyclic straining with a maximum strain of 3%, the stress-strain loops exhibit nonlinear response and become slimmer with the increasing number of cycles as seen in Fig. 2.10. The stress-strain response tends to stabilize after 70 cycles. The mean stress relaxation was observed and the mean stress appeared to approach an asymptotic value of 21.0 MPa, while the mean stress at the first cycle was approximately 29.3 MPa, see Fig. 2.12. The specimen lasted over 100 cycles prior to fracture. When the strain range was reduced to 1.5%, the stress-strain loops became nearly linear for most of the cycles as depicted in Fig. 2.11. It was also noted that the mean stress relaxation was very small, about 2 MPa. The specimen did not fail at this strain range even after over 600 cycles. The observed longer life under cyclic straining with a mean strain compared to that of cyclic stressing with a mean stress could be attributed to the stress relaxation phenomenon in the former and accumulation of ratcheting strains in the latter case.

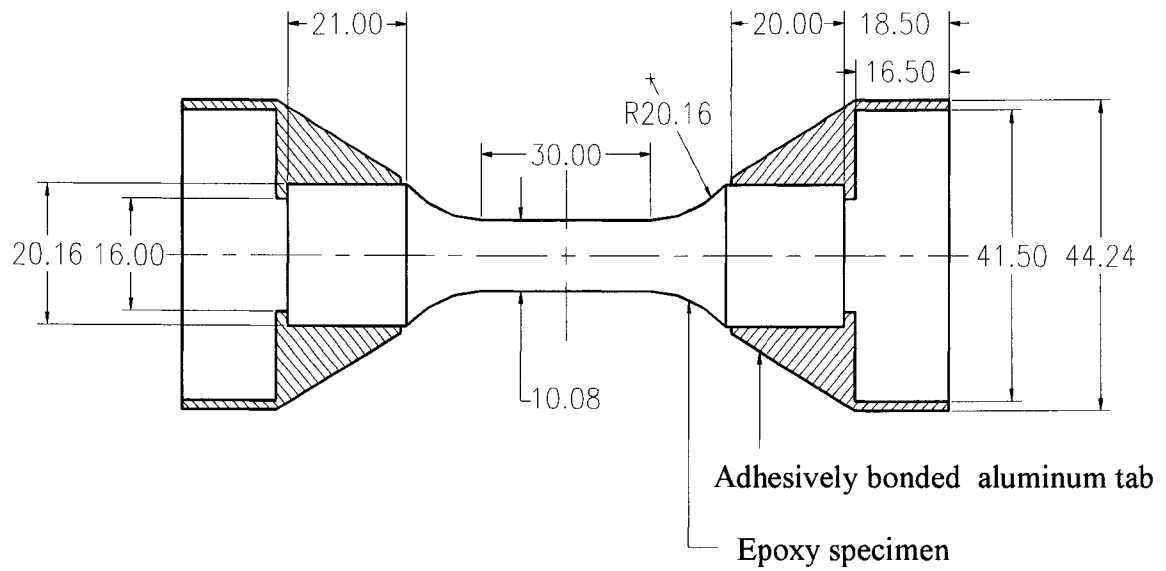
2.4 Conclusions

From the experimental results, the behavior of the epoxy polymer under cyclic loading can be summarized as follows:

1. The cyclic stress-strain response of this material is amplitude-dependent. At a low stress level, it is mainly a linear response. A nonlinear stress-strain hysteresis loop is observed at high cyclic stress levels. The nonlinearity is usually more pronounced in the first loading cycle. With increasing cycles, hysteresis loops become slimmer and less nonlinear except at very high stress levels.
2. Ratcheting strain is accumulated under stress controlled cyclic loading with mean stress. For small stress ranges, the ratcheting rate decreases with the increasing number of cycles and an asymptotic value of the ratcheting strain is reached. The observation of the full recovery of the ratcheting strain after stress removal, confirms the viscoelastic nature of the ratcheting strain.
3. The cyclic behavior of this material is also rate-dependent. With increasing loading rates, the stress-strain response becomes less nonlinear which results in less accumulated ratcheting strain and more stable stress-strain response.
4. Anisotropic response to tensile and compressive cyclic loading was noted. It was found that the material shows a better creep resistance in compression than in tension.
5. Mean stress relaxation was observed in strain controlled cyclic loading with mean strain. The mean stress of the cyclic straining as well as the stress-strain hysteresis loop reach a stable state with increasing number of cycles. For sufficiently small strain range, the mean stress relaxation was found to be negligible.

Control mode	Maximum stress or strain	Mean stress or strain	Stress/strain rate	Description
Stress control	45 MPa	22.5 MPa	0.24 MPa/s	Stress amplitude effect
	55 MPa	27.5 MPa	0.24 MPa/s	
	66 MPa	33.0 MPa	0.20 MPa/s	
Stress control	60 MPa	30.0 MPa	0.24 MPa/s	20 cycles of preloading followed by residual strain recovery
Stress control	55 MPa	27.5 MPa	24 MPa/s	Stress rate effect
Stress control	0 MPa	-27.5 MPa	0.24 MPa/s	Cyclic compression
Stress control	60 MPa	0 MPa	0.48 MPa/s	Fully reversed cyclic stressing
	38 MPa	0 MPa	0.61 MPa/s	
Strain control	3 %	1.5 %	$1.2 \times 10^{-4} \text{ s}^{-1}$	Strain-controlled tests and strain amplitude effect
	1.5 %	0.75 %	$1.2 \times 10^{-4} \text{ s}^{-1}$	

Table 1.1 Loading conditions of the test program



Dimensions in mm

Figure 2.1 Geometry of solid cylindrical specimen and end tabs

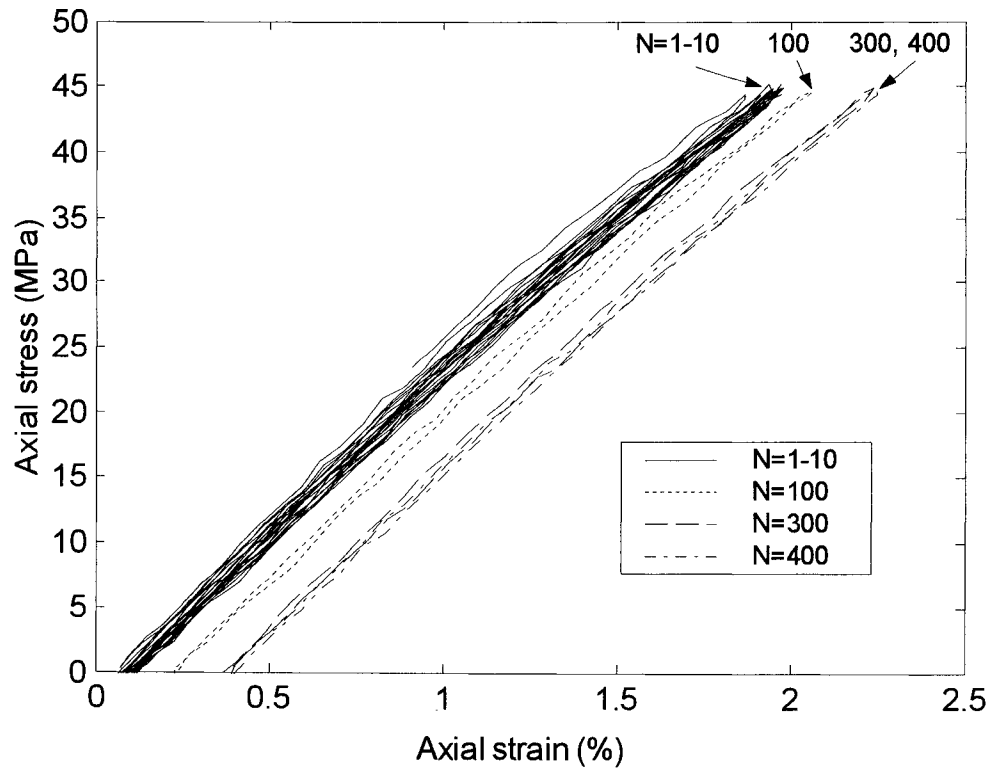


Figure 2.2 Stress-strain loops for the applied stress range of 45 MPa with a mean stress of 22.5 MPa

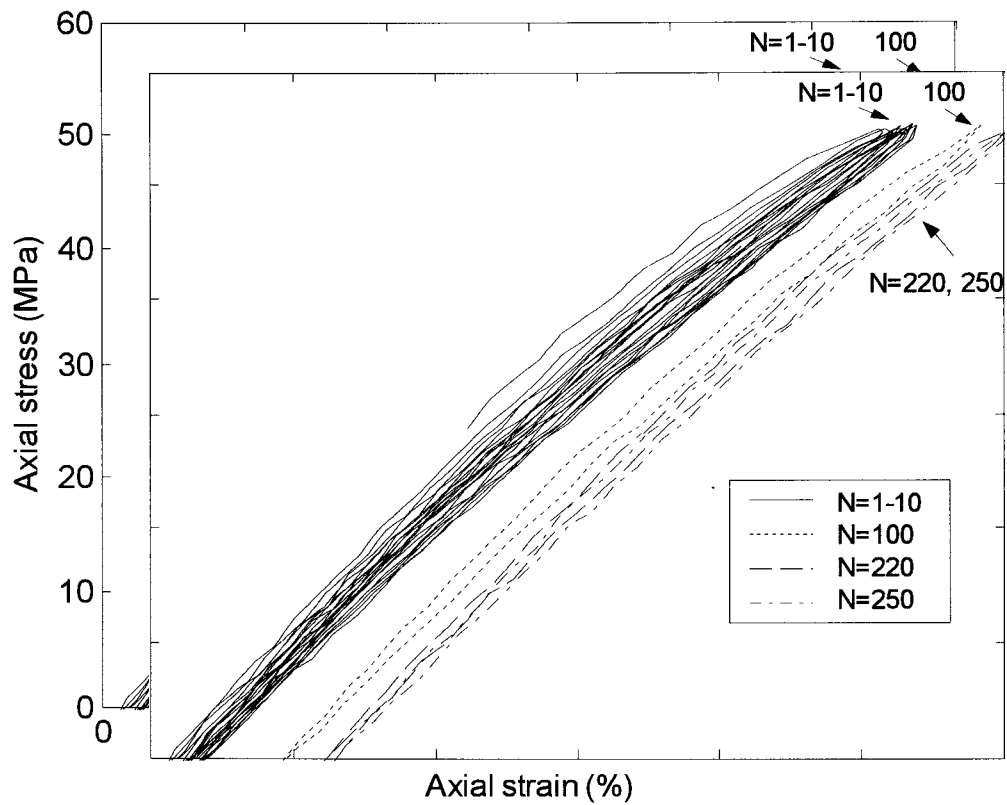


Figure 2.3 Stress-strain loops for the applied stress range of 55 MPa with a mean stress of 27.5 MPa

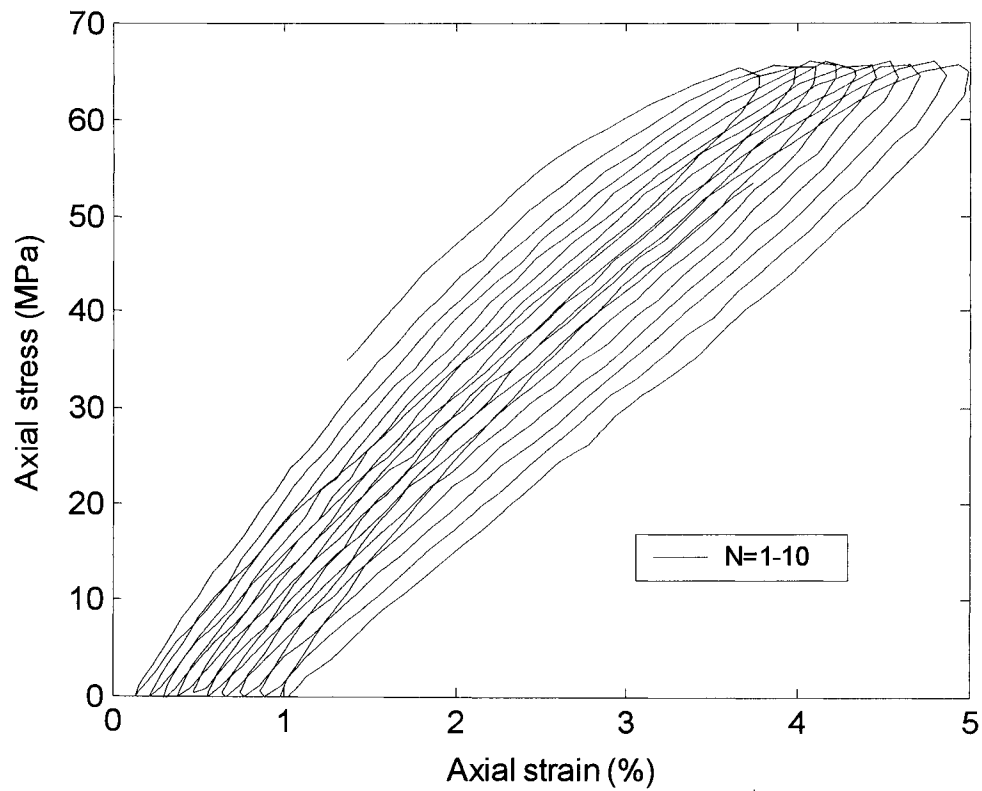


Figure 2.4 Stress-strain loops for the applied stress range of 66 MPa with a mean stress of 33 MPa

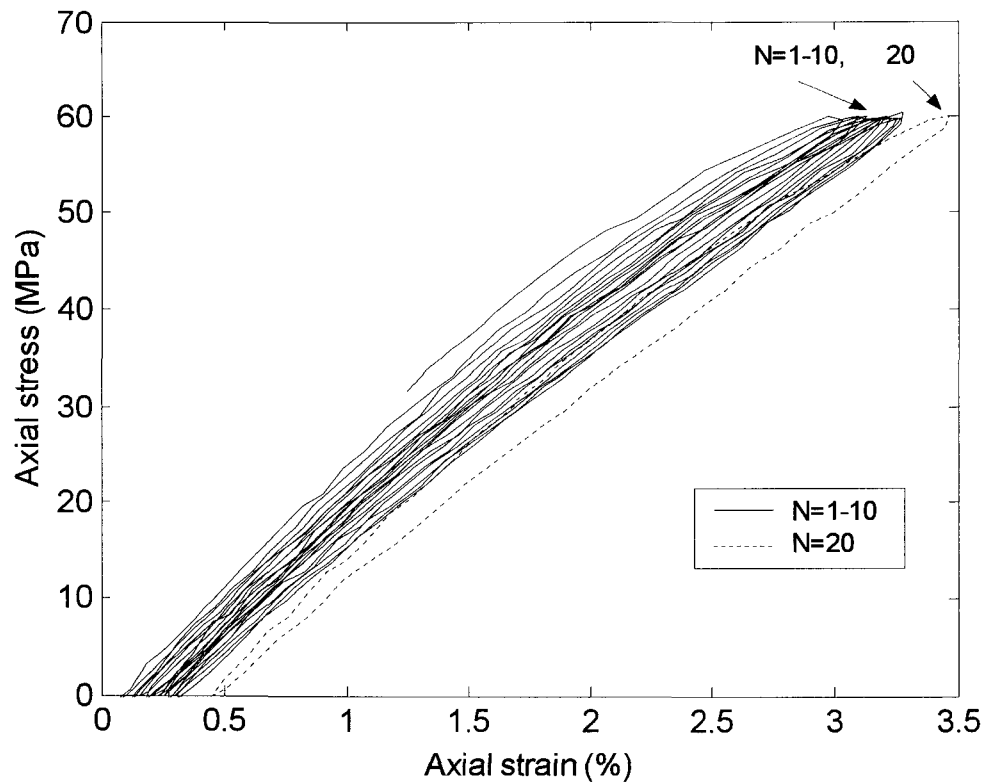


Figure 2.5 (a) Cyclic creep and recovery of residual strain: stress-strain loops for the 20 cycles pre-loading

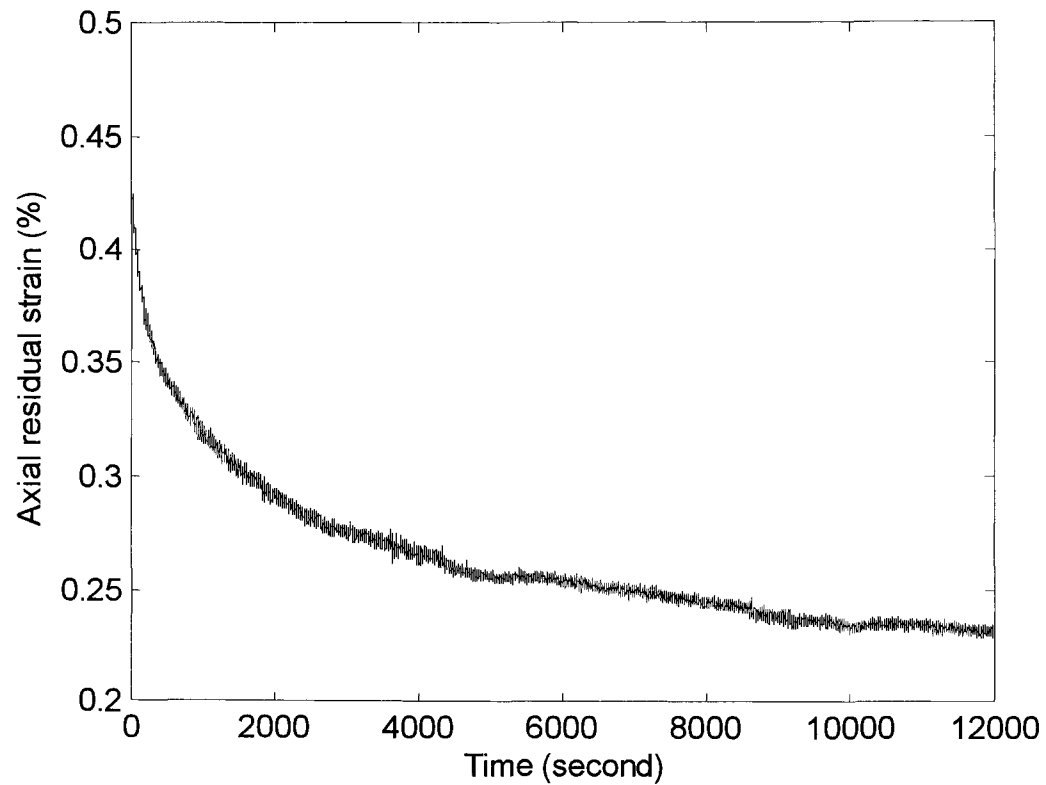


Figure 2.5 (b) Cyclic creep and recovery of residual strain: residual strain versus time after 20 cycles of preloading

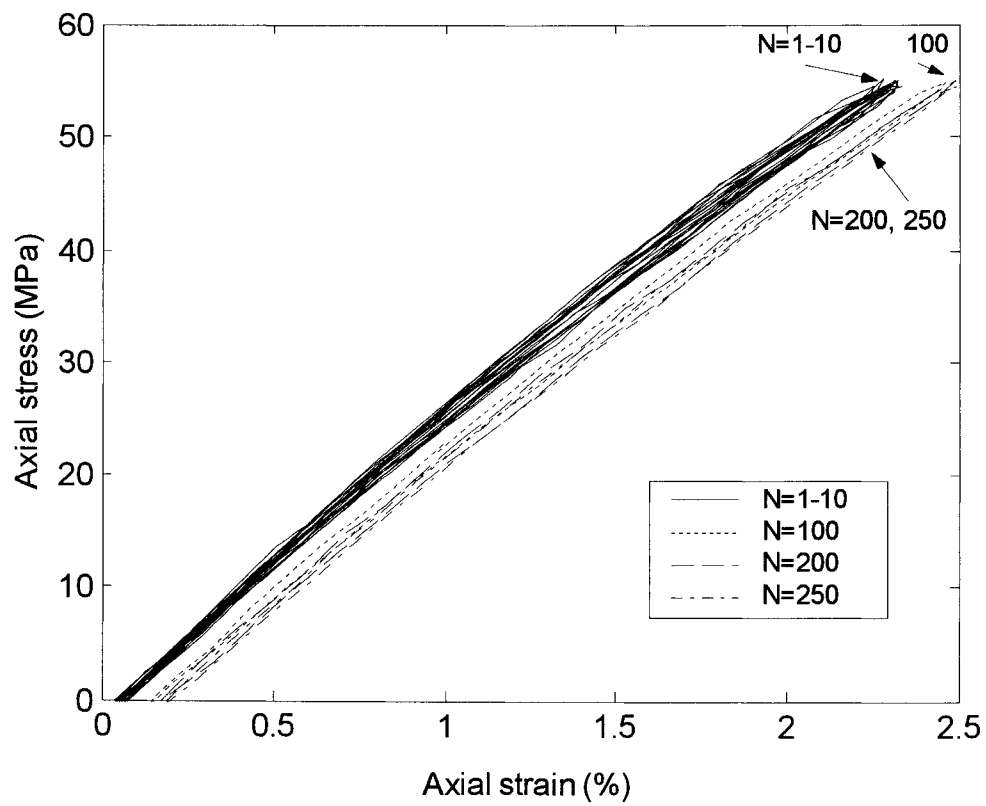


Figure 2.6 Stress-strain loops for a faster loading rate of 24 MPa/s with the applied stress range of 55 MPa and a mean stress of 27.5 MPa

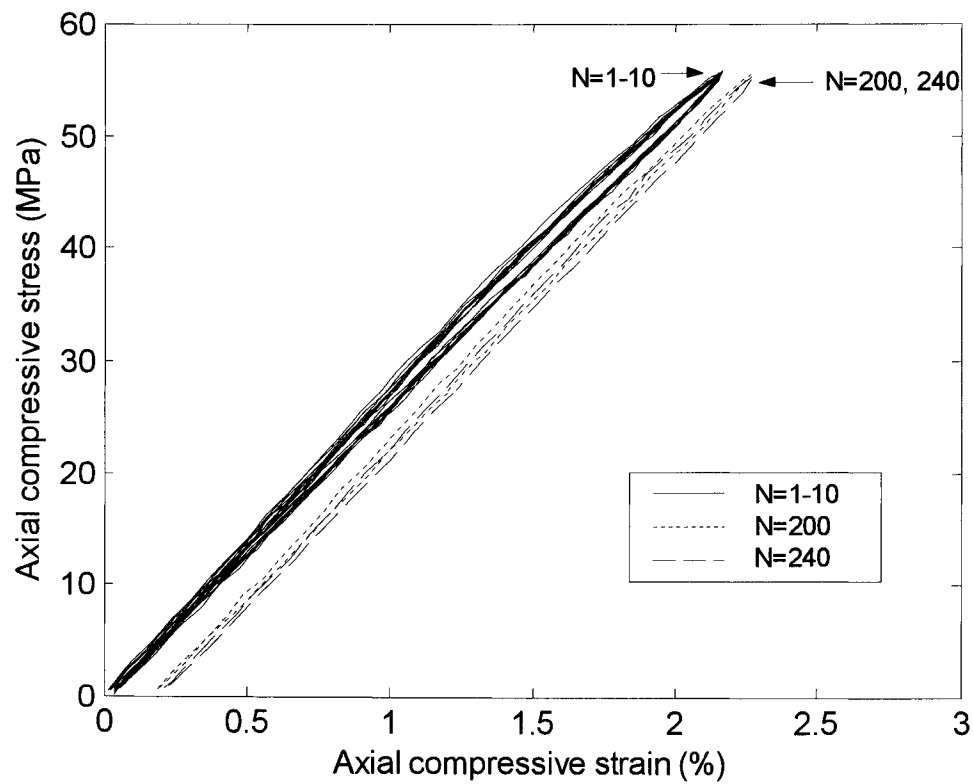


Figure 2.7 Stress-strain loops for a compressive cyclic loading with the applied stress range of 55 MPa and a mean stress of 27.5 MPa

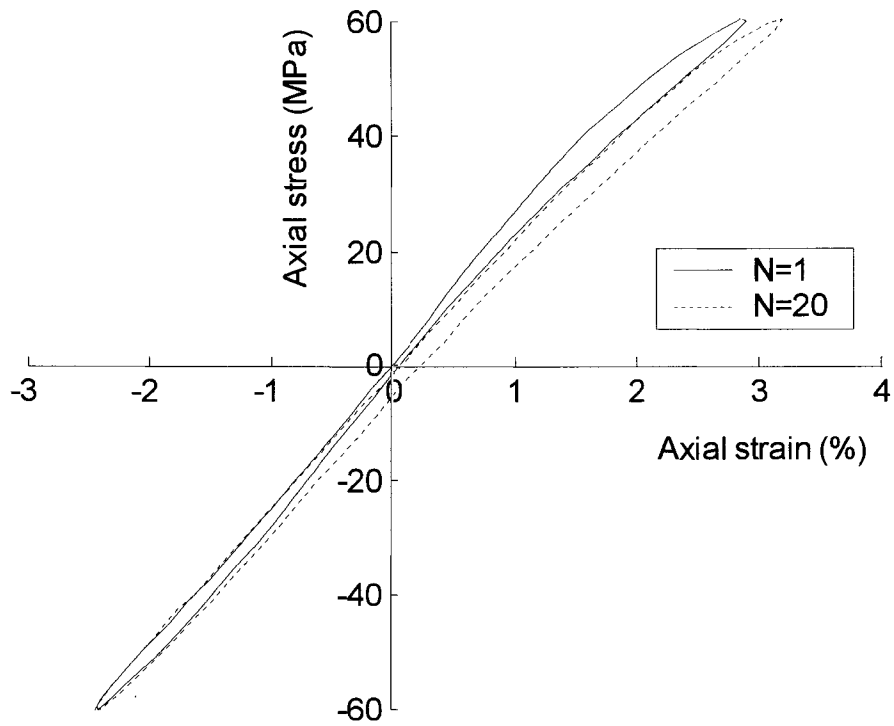


Figure 2.8 Stress-strain loops for a fully reversed cyclic loading with the stress amplitude of 60 MPa

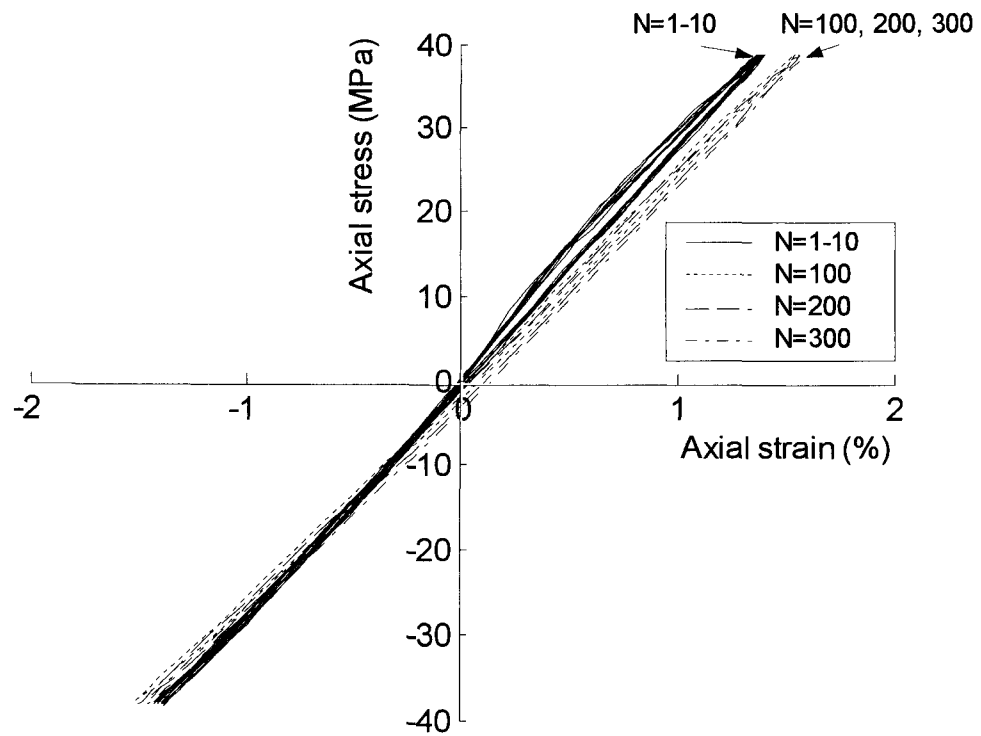


Figure 2.9 Stress-strain loops for a fully reversed cyclic loading with the stress amplitude of 38 MPa

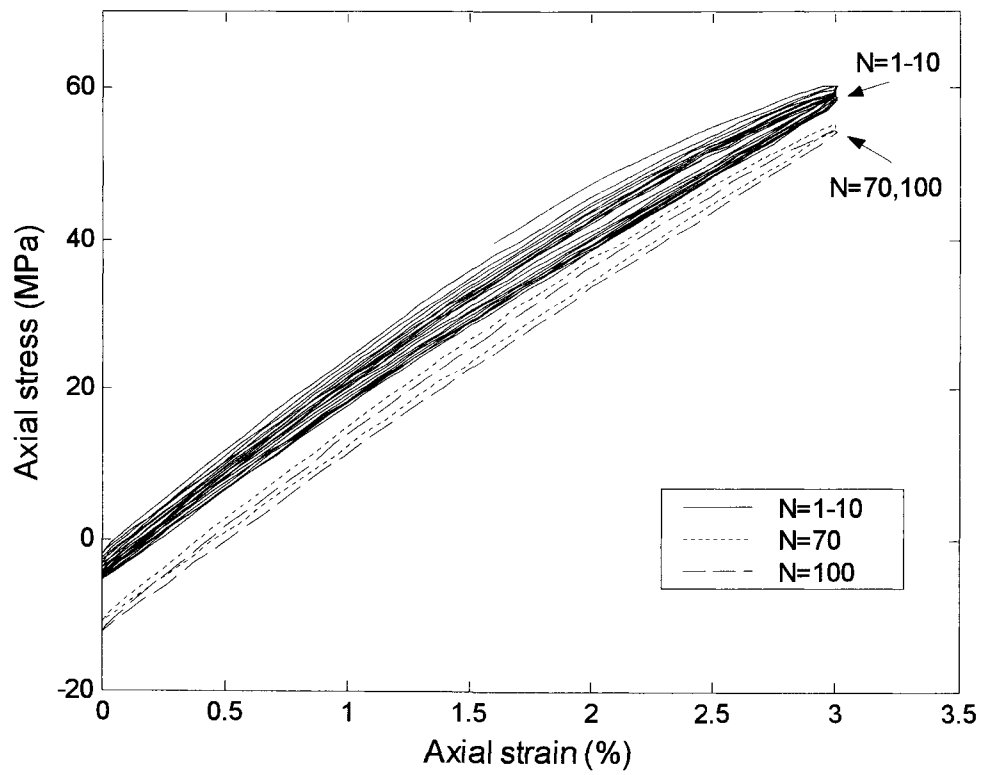


Figure 2.10 Stress-strain loops for the applied strain range of 3% with a mean strain of 1.5%

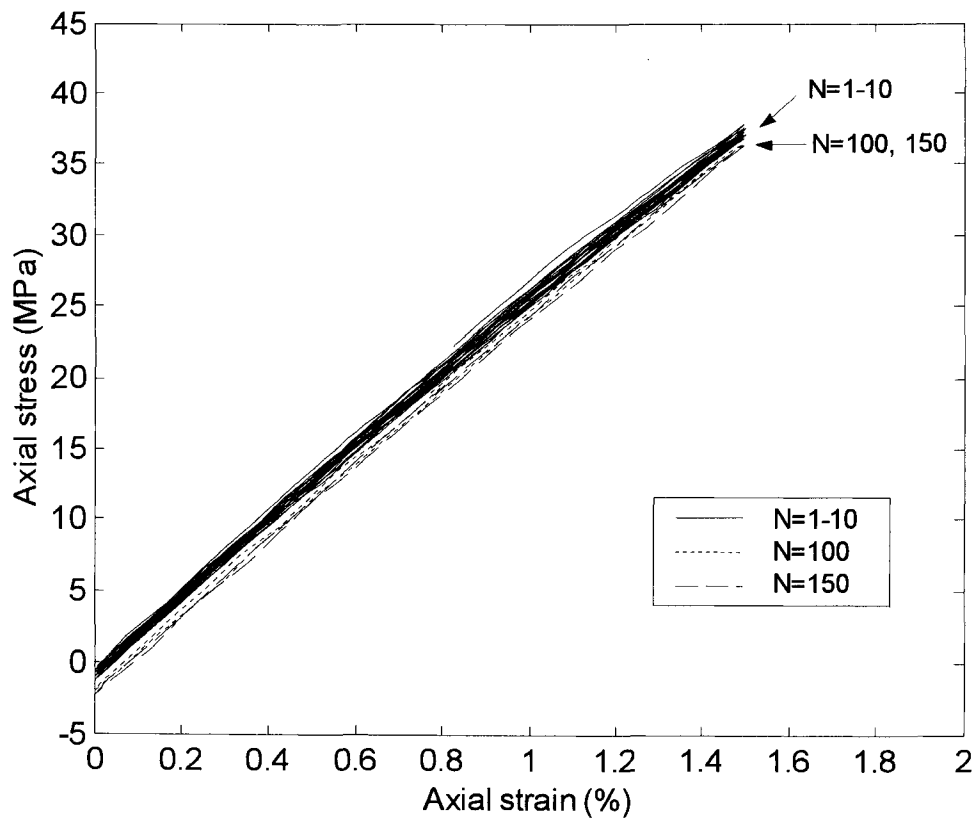


Figure 2.11 Stress-strain loops for the applied strain range of 1.5% with a mean strain of 0.75%

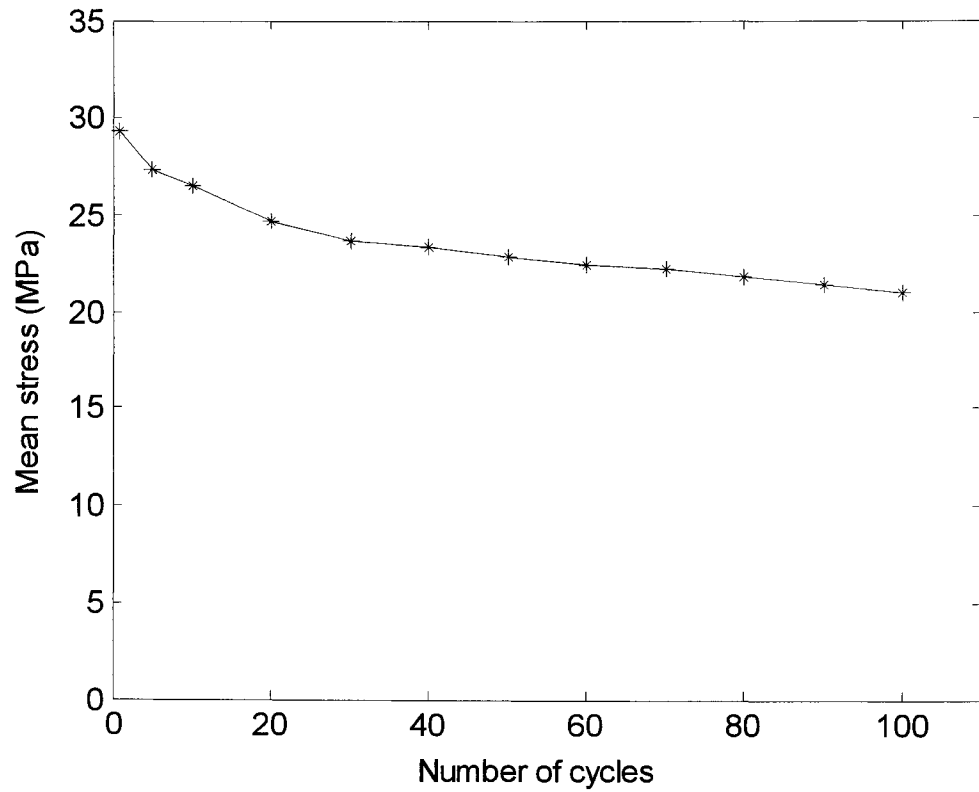


Figure 2.12 Mean stress versus the number of cycles for the applied strain range of 3% with a mean strain of 1.5%

Bibliography

1. Y. Hu, Z. Xia, and F. Ellyin, Deformation behavior of an epoxy resin subject to multiaxial loadings. Part I: experimental investigations. *Polym. Eng. Sci.*, **43**, 721 (2003).
2. Z. Xia, Y. Hu, and F. Ellyin, Deformation behavior of an epoxy resin subject to multiaxial loadings. Part II: constitutive modeling and predictions *Polym. Eng. Sci.*, **43**, 734 (2003).
3. S. Rabinowitz and P. Beardmore, Cyclic deformation and fracture of polymers. *J. Mater. Sci.*, **9**, 81 (1974).
4. C. Kaynak and O. Mat, Uniaxial fatigue behavior of filament-wound glass-fiber/epoxy composite tubes. *Compos. Sci. Technol.* **61** 1833 (2001).
5. D. J. Kizypow and C. M. Rimnac, Cyclic steady state stress-strain behavior of UHMW polyethylene. *Biomaterials*, **21**, 2081 (2000).
6. T. Nishitani and T. Yamashita, Mechanical behavior and formulation of stress-strain relation for non-linear viscoelastic cellulose nitrate under cyclic loadings. *J. Mater. Sci.*, **21**, 2830 (1986).
7. T. Ariyama, Cyclic deformation and relaxation characteristics in polypropylene. *Polym. Eng. Sci.*, **33**, 18 (1993).
8. T. Ariyama, Viscoelastic-plastic behavior with mean strain changes in polypropylene. *J. Mater. Sci.*, **31**, 4127 (1996).
9. A. I. Isayev, D. Katz and Y. Smooha, Dynamic properties of crosslinked epoxy resin at large cyclic and static deformation. *Polym. Eng. Sci.*, **21**, 566 (1981).
10. Designation: E 606-92, Annual book of ASTM Standards, **03.01**, (2003).
11. J. M. Hutchinson, Physical aging of polymers. *Prog. Polym. Sci.*, **20**, 703 (1995).
12. R.D. Bradshaw and L.C Brinson, A continuous test data method to determine a reference curve and shift rate for isothermal physical aging. *Polym. Eng. Sci.*, **39**, 211 (1999).
13. G.B. McKenna, Y. Leterrier, and C.R. Schultheisz, The evolution of material properties during physical aging. *Polym. Eng. Sci.*, **35**, 403 (1995).
14. J. M. Augl, Nonlinear creep effects of physical aging, temperature and moisture of an epoxy resin. *J. Rheol.*, **31**, 1 (1987).

-
15. F. Ellyin, *Fatigue Damage, Crack Growth, and Life Prediction*, Chapman & Hall, London, UK, Chapter 5. (1997).
 16. Y. H. Pao and J. Marin, An analytical theory of the creep deformation of materials. *J. Appl. Mech.*, **20**, 245 (1953).
 17. M. J. Mindel and N. Brown, Creep and recovery of polycarbonate. *J. Mater. Sci.*, **8**, 863 (1973).
 18. E. Kontou and P. Farasoglou, Determination of the true stress-strain behavior of polypropylene. *J. Mater. Sci.*, **33**, 147 (1998).

Chapter 3

Uniaxial Cyclic Deformation Behavior of an Epoxy Polymer : Predictions of Viscoelastic Constitutive Models

3.1 Introduction

Polymers and polymeric composites in engineering service are usually subjected to multiaxial stress state with complex loading histories, and in many cases, the loading is of a cyclic nature. With increasing application of these materials in major load-carrying components, a more accurate evaluation of stress/strain states in these structures is required. Due to the nonlinear nature of the viscoelastic behavior of polymers, the stress and deformation analyses could only be realized numerically, excluding analytical solutions in closed forms. For example, the finite element method has been extensively used in the analysis of mechanical systems with material nonlinearity or geometric nonlinearity. However, the reliability of such numerical predictions is highly dependent on the accuracy of the material's constitutive model used in the analysis [1-2]. Hence the choice and verification of constitutive models is a matter of practical significance.

A number of investigations have dealt with the nonlinear viscoelastic constitutive modeling of polymers and plastics, which may be grouped into two categories. The first group adopts the differential representations based on certain physical concepts on deformation and uses the rheological elements, see e.g. [3-7]. These models are relatively simple in form, and could easily be adopted into finite element analysis codes.

The second group uses integral representations, e.g. see [8-12] among others. These models are in general phenomenologically formulated, and often lead to relatively complicated mathematical expressions which require further simplification prior to implementing into finite element codes.

Among a considerable number of investigations, the choice of an appropriate nonlinear constitutive model involves several considerations. As pointed out in ref. [6], the usefulness of a numerical model depends largely on three major features, viz., the predictive capacity, the numerical implementation and the determination of material constants or functions. To be specific, an appropriate model should be able to simulate most experimental observations for various loading histories and paths. Meanwhile the constitutive equations should be sufficiently simple to allow implementation in the software algorithms, and the parameters in the model be easily evaluated from simple experimental tests. In view of the above criteria, a number of models could be overlooked. For example, the so-called multiple-integral approach [10] requires experimental determination of three relaxation kernels, which is a rather difficult task.

A recently proposed model in differential form by Xia et al. [7] meets the above criteria. Extensive experimental verifications have already been carried out on this model, which has shown a good predictive capability for various monotonic loading histories and paths. The data reduction procedure for determination of the material constants and functions is simple and well defined. Moreover, the model can distinguish between loading and unloading cases through the definition of a current loading surface and a corresponding switch rule. In this paper, the rule is further modified to suit more general (proportional or non-proportional) cyclic loading paths.

The often-quoted Shapery's single-integral constitutive model is selected here for the comparative purpose. This constitutive equation is relatively simple and the experimental determination of the material properties in this model is not onerous; hence it is often used by various researchers, see e.g. [13-15]. However, to allow an easy application in the finite element software, the transient creep function is often expressed in terms of Prony's series rather than the form of power law that appears in the initial model representation in ref. [8]. In this way, the constitutive equation can be expressed in incremental form with the hereditary integral updated at the end of each time increment by recursive computation [9,16].

It is the objective of this chapter to explore the predictive capacities of the two aforementioned constitutive models with respect to the deformation behavior of Epon 826 resin system under cyclic loading reported in the previous chapter [18]. Relatively few cyclic experimental verifications of constitutive models have been published in the open literature, partly due to the lack of the cyclic experimental data of polymers and plastics. The basic constitutive equations of the two models are briefly described first, and the predictions of both models are then presented and compared with the experimental results. It will be seen later on that a proper criterion to distinguish the loading/unloading cases is essential to correctly predict the viscous behavior of the epoxy polymer, especially for the cyclic loading.

3.2 Constitutive Models

3.2.1 Differential Representation

The differential model in a uniaxial representation can be viewed as a combination of one linear spring and several nonlinear Kelvin (Voigt) elements in series, schematically depicted in Fig. 3.1. It is assumed that the total strain rate, $\{\dot{\varepsilon}_t\}$, is the sum of the elastic and the creep strain rates, $\{\dot{\varepsilon}_e\}$ and $\{\dot{\varepsilon}_c\}$, respectively, i.e.

$$\{\dot{\varepsilon}_t\} = \{\dot{\varepsilon}_e\} + \{\dot{\varepsilon}_c\} \quad (1)$$

the elastic strain rate is calculated through the generalized Hooke's law,

$$\{\dot{\sigma}\} = E[A]^{-1}\{\dot{\varepsilon}_e\} \quad (2)$$

where E is the elastic modulus, $[A]$ is a matrix related to the value of Poisson's ratio and defined by

$$[A] = \begin{bmatrix} 1 & -\nu & -\nu & 0 & 0 & 0 \\ -\nu & 1 & -\nu & 0 & 0 & 0 \\ -\nu & -\nu & 1 & 0 & 0 & 0 \\ 0 & 0 & 0 & 1+\nu & 0 & 0 \\ 0 & 0 & 0 & 0 & 1+\nu & 0 \\ 0 & 0 & 0 & 0 & 0 & 1+\nu \end{bmatrix} \quad (3)$$

For a number of Kelvin (Voigt) elements connected in series, creep strain rate is the sum of the strain rate of each element, i.e.

$$\{\dot{\varepsilon}_c\} = \sum_{i=1}^n \{\dot{\varepsilon}_{ci}\} = \sum_{i=1}^n \left(\frac{[A]}{E_i \tau_i} \{\sigma\} - \frac{1}{\tau_i} \{\varepsilon_{ci}\} \right) \quad (4)$$

where $\tau_i = \eta_i / E_i$ denotes the retardation time, η_i is the dashpot viscosity and E_i is the spring stiffness for the i -th Kelvin (Voigt) element, respectively. The description of the

nonlinear behavior in this model is achieved by letting E_i be a function of the current equivalent stress, σ_{eq} , and a single functional form for all E_i is assumed, i.e.

$$E_i = E_i(\sigma_{eq}).$$

To describe the different behavior in tension and compression of polymers, the equivalent stress is defined by

$$\sigma_{eq} = \frac{(R-1)I_1 + \sqrt{(R-1)^2 I_1^2 + 12RJ_2}}{2R} \quad (5)$$

which is adopted from Stassi equation, where I_1 is the first stress invariant, J_2 is the second deviatoric stress invariant and R is the ratio of the “yield” stress in compression to that in tension. Note that for an isotropic material $R=1$, and Eq. (5) reduces to the familiar von Mises equivalent stress, $\sigma_{eq} = \sqrt{3J_2}$.

A distinct feature of this constitutive model is its capacity of distinguishing between loading and unloading cases by introducing a current loading surface and a corresponding switch rule. Based on cyclic test data presented in previous chapter and in consideration of various possible multiaxial cyclic paths (cyclic paths with variable amplitudes, proportional or non-proportional cyclic loading, etc.) a modified version of the switch rule is proposed herein. It is seen from the cyclic test data that the first stress-strain hysteresis loop differs the most from the rest of hysteresis loops. That is, the shapes of hysteresis loops after the first cycle differ by much smaller value among them. Furthermore, with the gradual reduction of the amount of viscous strain, a steady state cyclic regime is reached provided the maximum applied stress is not too large. This

experimental observation indicates that the calculation of spring stiffnesses of the Kelvin elements, $E_i = E_i(\sigma_{eq})$, must follow a different rule for the cyclic loading after the first switch from loading to unloading path. To delineate the loading/unloading cases for general multiaxial loading paths including monotonic or cyclic ones, a stress memory surface is defined as

$$f_m^\sigma(\sigma_{ij}) - R_{\max}^2 = \frac{3}{2} s_{ij} s_{ij} - R_{\max}^2 = 0 \quad (6)$$

where $s_{ij} = \sigma_{ij} - \frac{1}{3} \sigma_{kk}$ is the deviatoric stress components. The radius of the memory surface, R_{mem} , is determined by the maximum von Mises stress level experienced by

the material during its previous loading history, i.e. $R_{mem} = \sqrt{\left(\frac{3}{2} s_{ij} s_{ij}\right)_{\max}}$. Therefore,

for a monotonic loading from the virgin state, the stress memory surface will expand isotropically with the increasing stress level, see Fig. 3.2. If σ_{ij}^t is the current stress

point, $d\sigma_{ij}^t$ is the stress increment at time t , and $\left(\frac{\partial f}{\partial \sigma_{ij}}\right)_{\sigma_{ij}=\sigma_{ij}^t}$ represents the direction of

the normal to the memory surface at the current stress point, then a criterion to distinguish the loading/unloading cases is introduced as follows (Fig. 3.2):

- if the current stress point is on the memory surface and $\left(\frac{\partial f}{\partial \sigma_{ij}}\right)_{\sigma_{ij}=\sigma_{ij}^t} \cdot d\sigma_{ij}^t \geq 0$, this signifies a loading case;
- if the current stress point is on the memory surface and $\left(\frac{\partial f}{\partial \sigma_{ij}}\right)_{\sigma_{ij}=\sigma_{ij}^t} \cdot d\sigma_{ij}^t < 0$, then a switch from loading to unloading occurs;

- if the current stress point is inside the memory surface, i.e. $f_m^\sigma(\sigma_{ij}^t) - R_{\max}^2 < 0$, it is then an unloading case.

For the loading case the spring stiffness of the Kelvin elements is defined as a function of the equivalent stress, $E_i = E_1(\sigma_{eq})$. For the unloading case, it is assumed that E_i remains the same value during the entire unloading process, which is equal to the value of E_i at the switch point, where unloading takes place. According to this rule, for a cyclic loading with constant stress amplitude, $E_i = E_1(\sigma_{eq})$ is applied only to the first loading branch. Following the first switch from loading to unloading, a constant value of E_i is used for the rest of the cycles. This is because the stress point remains inside the memory surface at all times as long as σ_{\max} is fixed. For a cyclic loading with variable amplitude, a switch to equation $E_i = E_1(\sigma_{eq})$ takes place as soon as the stress point goes beyond the current memory surface and the memory surface expands again with the increasing stress level.

3.2.2 Integral Representation

For the stress-strain relation under isothermal condition, the Schapery single integral representation [8,16] takes the form of:

$$\varepsilon_{ij}(t) = g_0 D_0 \sigma_{ij} + g_1 \int_0^t \Delta D_t [\psi(t) - \psi(\tau)] \frac{dg_2 \sigma_{ij}}{d\tau} d\tau \quad (7)$$

where D_0 is the instantaneous component of creep compliance, ΔD_t is the transient creep compliance which may be expressed in either of the two forms [13]:

$$\Delta D(\psi) = D_1 \psi^n \quad \text{or} \quad \Delta D(\psi) = \sum_r D_r [1 - \exp(-\lambda_r \psi)] \quad (8)$$

in which ψ is the so-called reduced time, defined by

$$\psi(t) = \int_0^t \frac{d\tau}{a_\sigma} \quad (9)$$

The material properties: g_0 , g_1 , g_2 and a_σ , are functions of stress. To account for the difference in tensile and compressive response of polymers, Lai and Bakker [9] have suggested a modification to Schapery's model in which g_0 and a_σ are assumed to be a function of the first stress invariant, $I_1 = \sigma_{kk}$, with $g_0(-\sigma_{kk}) = 1/g_0(\sigma_{kk})$, $a_\sigma(-\sigma_{kk}) = 1/a_\sigma(\sigma_{kk})$ and g_1 , g_2 are a function of von Mises equivalent stress, i.e. $g_1 = g_1(\sigma_{eq})$, $g_2 = g_2(\sigma_{eq})$, where $\sigma_{eq} = \sqrt{(3s_{ij}s_{ij})/2}$.

3.2.3 Material Parameters

The material constants or functions for both the integral and the differential models are calibrated based on the experimental data of the stepped creep test, see Fig. 3.3, which is directly taken from [7,17]. The material parameters or functions utilized for both models are listed in Appendix and detailed determination procedure can be found in refs. [7,8].

3.3 Comparison of Model Predictions with Experimental Data

3.3.1 Uniaxial Tensile Loading/unloading Test

Experimental data indicate that the first stress/strain hysteresis loop is noticeably different from the subsequent loops. It is therefore critical to evaluate different constitutive models by checking their predictive capabilities for the first loading and unloading branches of the stress/strain curves. The experimental and predicted loading/unloading curves by the two models for a uniaxial tensile test with a strain rate of $0.7 \times 10^{-5} \text{ s}^{-1}$ are shown in Fig. 3.4. This figure shows strong nonlinearity and viscoelastic response of the material. It can be seen that the prediction by the differential model is in very good agreement with the test data both for the loading and the unloading branches. The integral model provides a good prediction for the loading branch, however, for the unloading branch, the prediction is indeed poor even with an incorrect curvature. The comparison points out the importance for a constitutive model to have a capability to delineate the loading and unloading paths.

3.3.2 Cyclic Loading with Different Stress Ranges

The predictions of constitutive models for cyclic stressing with two different stress amplitudes are depicted in Figs. 3.5 and 3.6. It is observed that both the differential and integral model simulate the ratcheting trend correctly, i.e. with the increase of numbers of cycles the predicted ratcheting rate decreases and the stress-strain hysteresis loops gradually reach a saturated state, a phenomenon confirmed by experiments. However, the integral model significantly underestimates the accumulated

ratcheting strains for both loading levels cf. Figs. 3.5(c) & 3.6(c) with Figs. 3.5(a) & 3.6(a). In contrast, the prediction by the differential model is much closer to the experimental data. For example, for an applied cyclic stress range of 55 MPa (Fig. 3.6), a stable cyclic state was attained at $N=220$ cycles. The predicted ratcheting strain by the differential model is approximately 0.58%, quite close to the experimental value of 0.63%, while the integral model significantly underestimates the ratcheting strain with a predicted value of 0.27%. With reference to Fig. 3.6, where a relatively high applied stress induced pronounced nonlinear response, the integral model predicted the unloading branches with an opposite curvature to that of the experimental observation, Fig. 3.6(a). In contrast, the differential model predictions are quite satisfactory both with respect to the primary stress-strain responses (shape of stress-strain loops) and the accumulated ratcheting strains.

3.3.3 Accumulation and Recovery of the Ratcheting Strain

The experimental and predicted stress-strain curves for a cyclic preloading of 20 cycles and the subsequent recovery of the residual strain (ratcheting strain) are shown in Figs. 3.7 and 3.8. It is observed that although both models predict the full recovery of the residual strain after removal of the load, the differential model predictions are in a much better agreement with the experimental data in a quantitative sense. After 20 cycles of pre-loading, the ratcheting strain predicted by the differential model is approximately 0.6%, close to the experimental value of 0.45%, while the integral model gives a considerably underestimated value of about 0.17%. That also leads to a better

prediction by the differential model for the ratcheting strain recovery curve as shown in Fig. 3.8.

3.3.4 The Effect of Loading Rate

Figure 3.9 compares the experimental data with the predictions of constitutive models in the case of cyclic loading with a stress range of 55 MPa but with a stress rate of 24 MPa/s. This is two orders of magnitude higher than that applied in the previous test, see e.g. 0.24 MPa/s in Fig. 3.6. It was seen that both models were able to predict the hysteresis loops with a more linear and slimmer shape in the fast loading rate. Also, both constitutive models indicated the correct ratcheting trend with respect to the increased rate. The predicted accumulated ratcheting strain amplitudes by both models are smaller compared to their counterparts under the same stress amplitude but with a slower loading rate, and are in agreement with experimental observations, cf. Figs. 3.6 and 3.9. It is to be noted that integral model in this case predicted a closer ratcheting strain value to the experimental data.

3.3.5 Anisotropy in Tension and Compression

Cyclic tests were conducted in pure compression with a stress range of 55 MPa and a stress rate of 0.24 MPa/s, Fig. 3.10. In comparing these results with the similar pure tension tests (cf. Figs. 3.10a and 3.6a) one notes two differences: (a) the width of the hysteresis loops is smaller in the case of compression tests, i.e. less nonlinearity, and (b) the ratcheting strain is decreased as well. When comparing the test data with the predictions of the constitutive models, it is noted that both the differential and the

integral models do predict the difference in behavior in cyclic tension versus cyclic compression. That is, both models predict a reduced ratcheting strain, and slimmer and more linear shape of stress-strain loops cf. Figs. 3.10(b) and (c) vs. 3.6(b) and 3.6(c), respectively.

3.3.6 Fully Reversed Cyclic Loading

The predicted stress-strain loops for fully reversed cyclic loading at an applied stress amplitude of 60 MPa are depicted in Fig. 3.11(a). It is seen that at this relatively high stress level, the nonlinear stress-strain response is quite evident. In this case, the differential model gives a more satisfactory result than that by the integral model, especially for the shape of stress-strain loops and the anisotropy of accumulated ratcheting strains in tension and compression cf. Figs 3.11(b) and 3.11(c) with 3.11(a).

3.3.7 Strain Controlled Cycling with Different Strain Amplitudes

Figures 3.12 and 3.13 compare the predicted stress-strain loops with the experimental results for strain-controlled cycling with two different tensile strain ranges of 3.0% and 1.5%, respectively. It is noted that in the case of the high cyclic strain level (Fig. 3.12), both models predict a mean stress relaxation for this type of loading, and both simulations show a stable stress-strain response after 70 cycles of loading (see the identical shape of stress-strain curves at $N=70$ and $N=100$). The predicted minimum stress at the cyclic stable state decreases approximately 10 MPa compared with that at the initial cycle. This is in agreement with the experimental observation. With the strain range of 1.5 % (Fig. 3.13), both models predict almost linear stress-strain curves

throughout the cycling process, which is consistent with the experimental data. The cyclic stable curves are also in satisfactory agreement with the test result. However, the predictions by the differential model demonstrate a better agreement with the experimental data, in particular, for unloading case at the high cyclic strain range as shown in Fig. 3.12.

3.4 Conclusions

In comparing the constitutive model predictions of the differential and the integral formulations with the experimental results, the following conclusions are drawn:

1. To correctly predict the stress-strain responses under cyclic loading, it is essential for a constitutive model to have an appropriate criterion and a switching rule to delineate the loading-unloading cases. As shown in the presented comparisons, both the loading and unloading behavior is well predicted by the differential model. This is mainly because it incorporates a criterion delineating loading/unloading. In contrast, the integral model predicts the unloading case with a trend that is contrary to that observed experimentally.
2. Under stress-controlled cyclic loading with a mean stress, ratcheting strains are accumulated. In most cases, the differential model is capable of simulating the ratcheting deformation behavior, both qualitatively and quantitatively. On the other hand, the integral model predictions are not as good, especially at high stress levels.

3. Under strain-controlled cyclic loading with mean strain, there is a mean stress relaxation. Both differential and integral models are capable of simulating the stress relaxation behavior.
4. In certain loading conditions such as fast rate and cyclic loading with sufficiently small stress/strain ranges, the material response was an almost linear and much slimmer hysteresis shape. In such cases, the integral model simulated experiments quite well. However, for loading conditions where a pronounced nonlinearity was observed, the need for incorporating a rule to delineate loading/unloading became necessary.

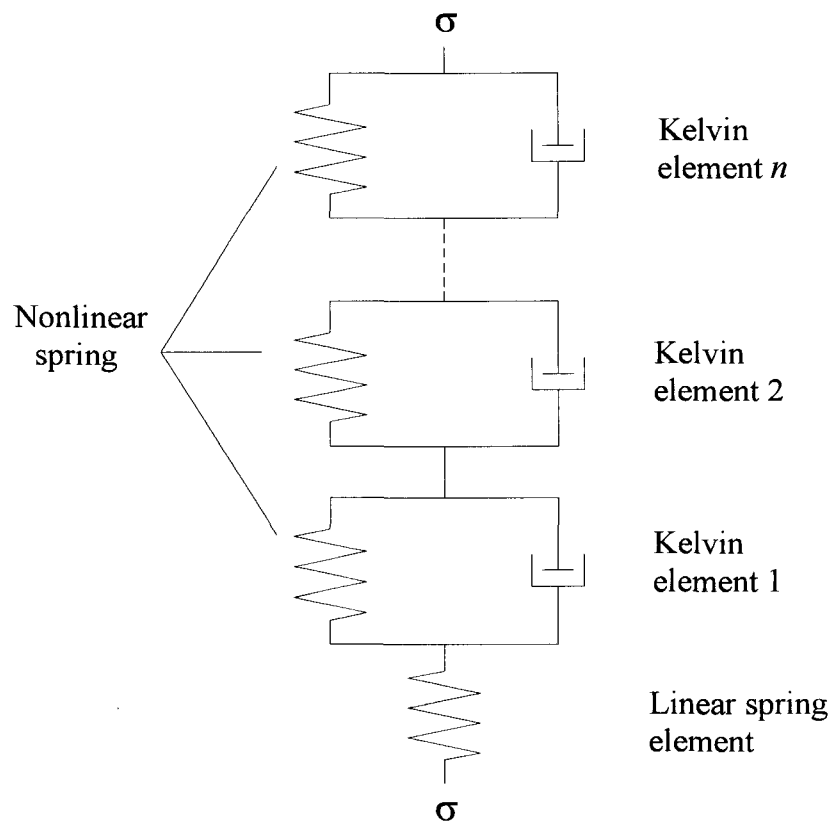


Figure 3.1 Uniaxial representation of the differential model: combination of an elastic spring and a number of Kelvin (Voigt) elements in series.

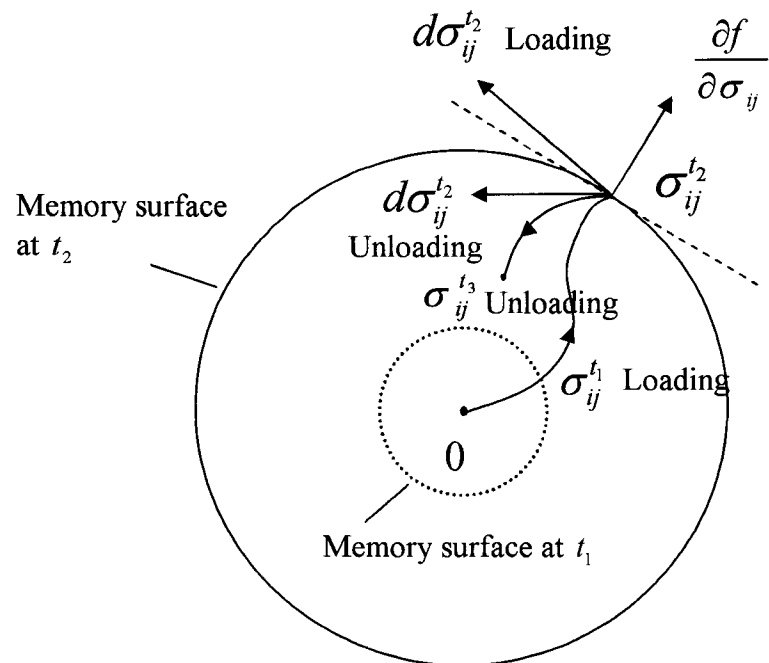


Figure 3.2 Schematic representation of a current memory surface and the loading/unloading criterion.

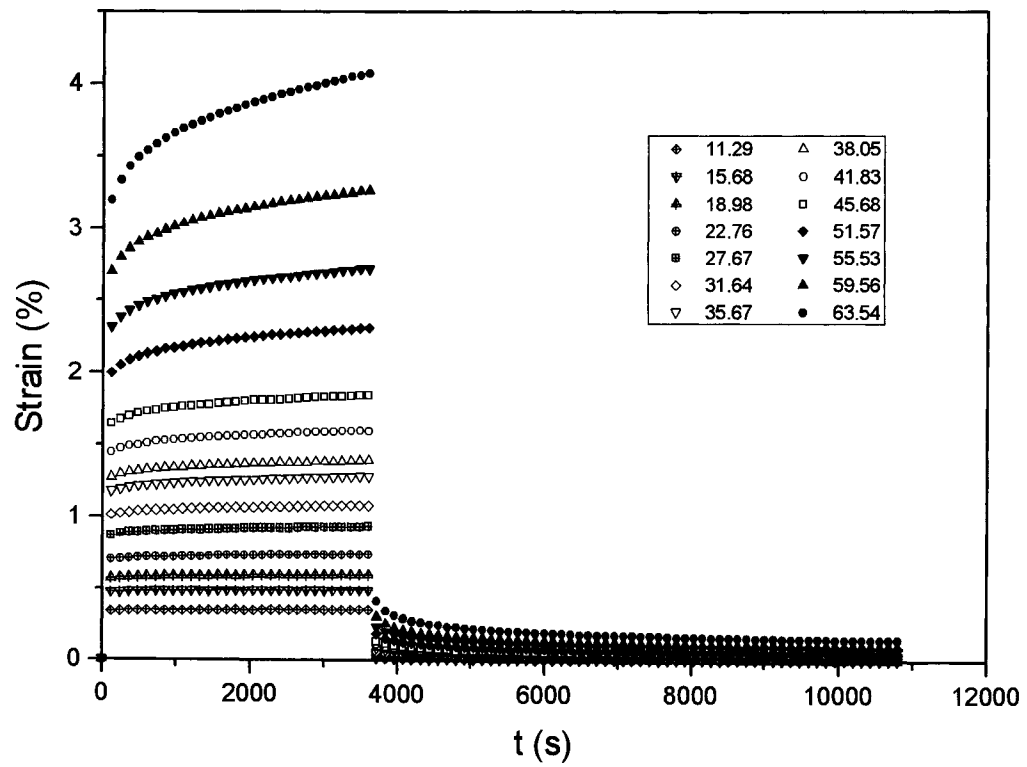


Figure 3.3 Creep and recovery curves at different stress levels (adopted from Hu et al.[17]).

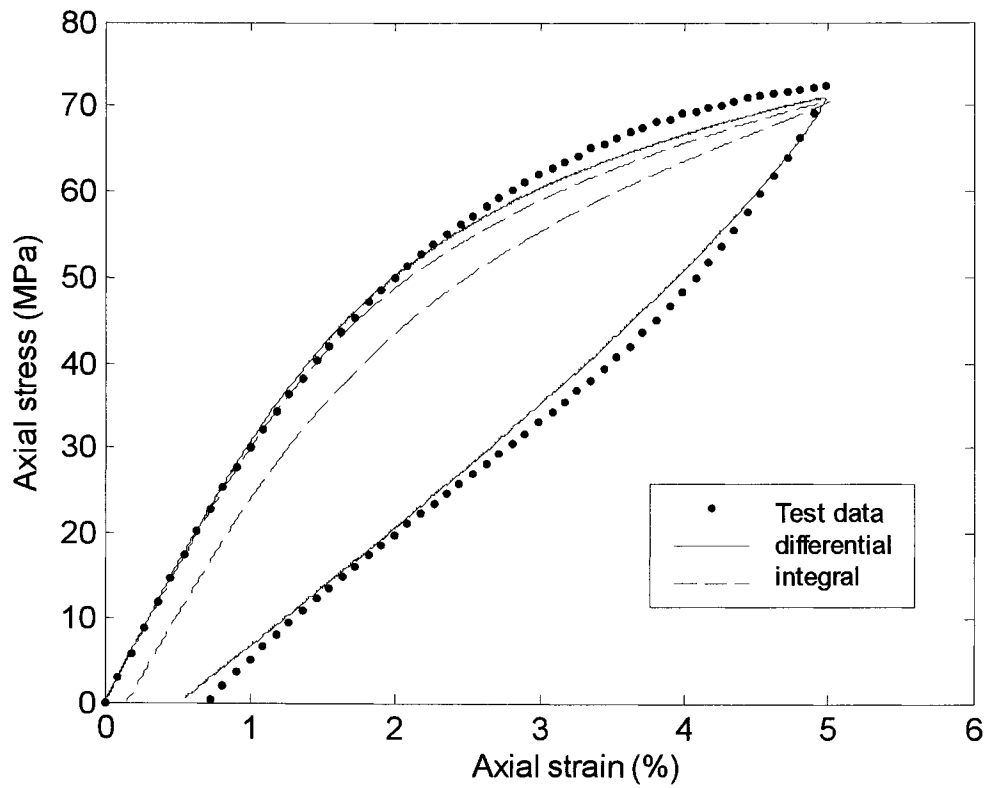


Figure 3.4 A comparison between the experimental result and the predicted uniaxial loading-unloading curves.

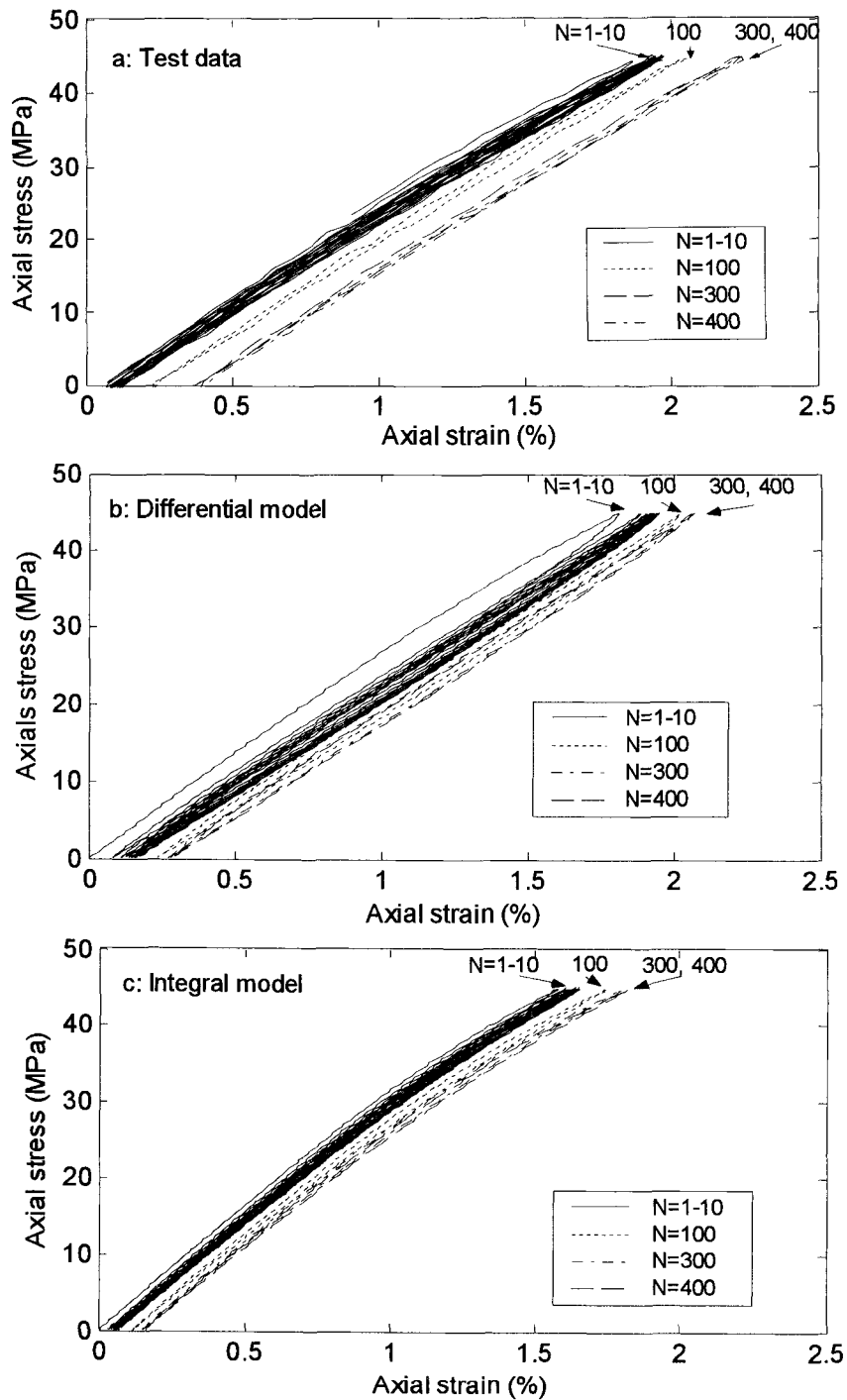


Figure 3.5 Stress-strain responses to a cyclic loading with a stress range of 45 MPa and a mean stress of 22.5 MPa (a) test data, (b) differential model predictions and (c) integral model predictions.

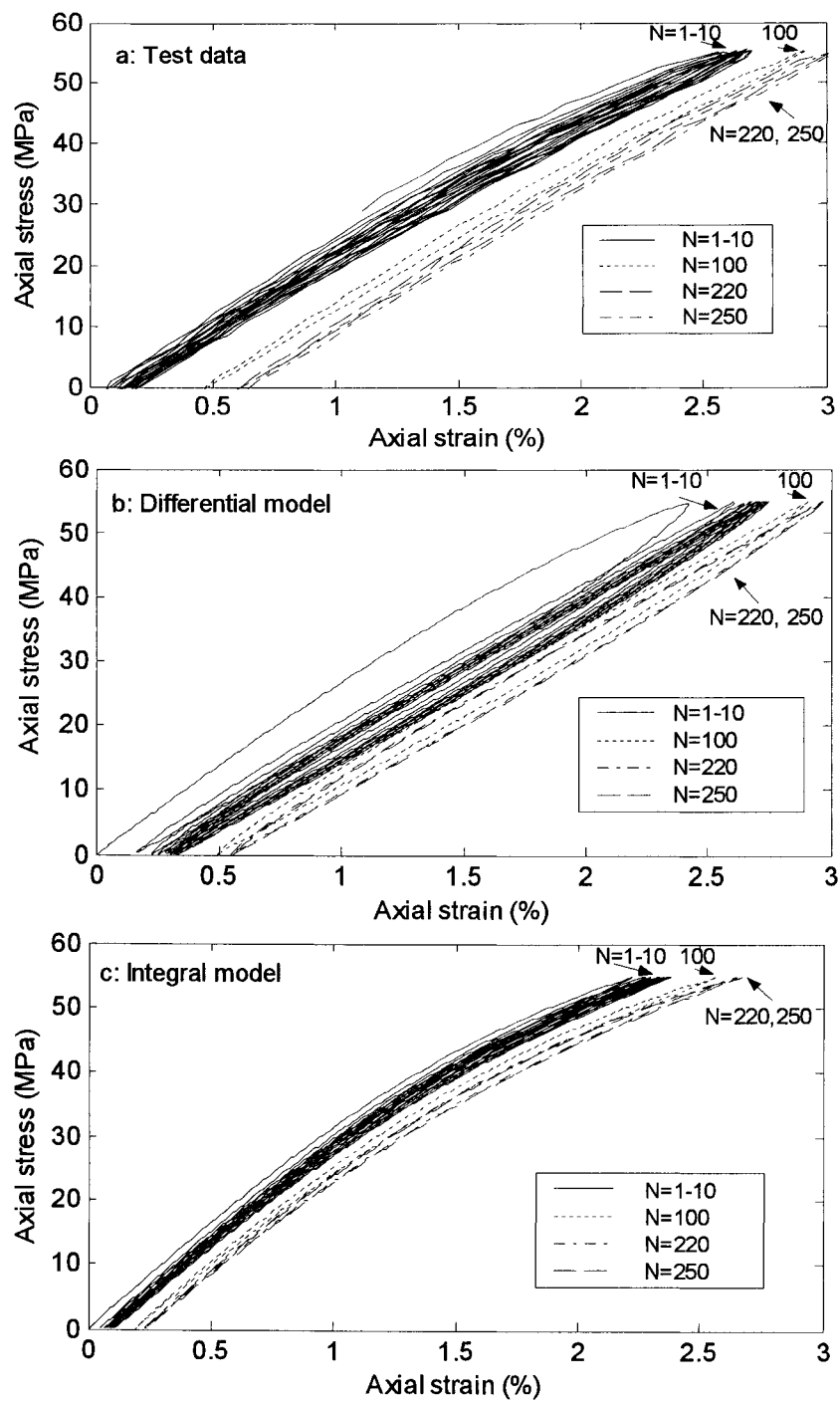


Figure 3.6 Stress-strain responses to a cyclic loading with a stress range of 55 MPa and a mean stress of 27.5 MPa (a) test data, (b) differential model predictions and (c) integral model predictions.

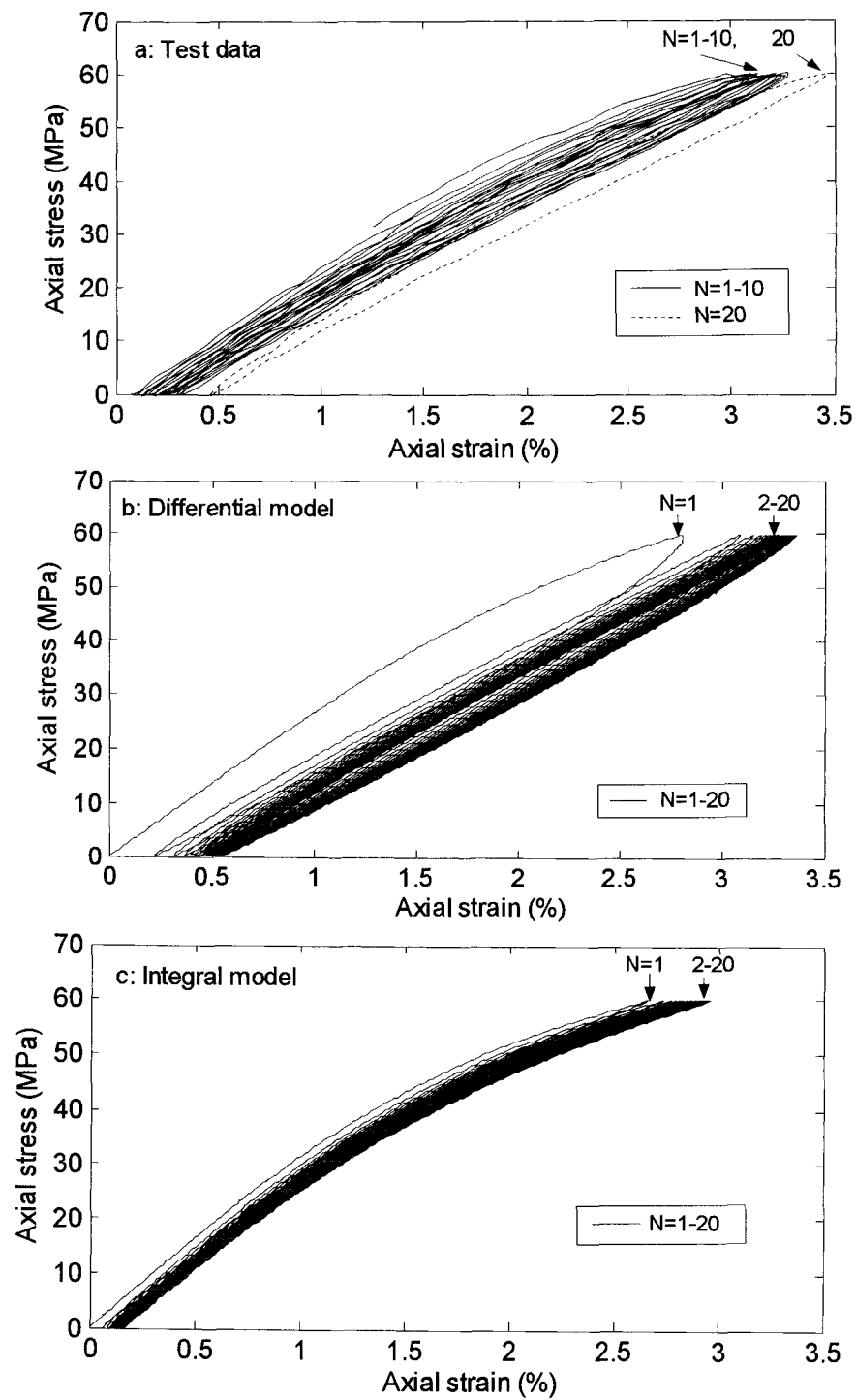


Figure 3.7 Stress-strain curves for 20 cycles of preloading under a cyclic stress with a maximum of 60 MPa and a mean stress of 30 MPa (a) test data, (b) differential model predictions and (c) integral model predictions.

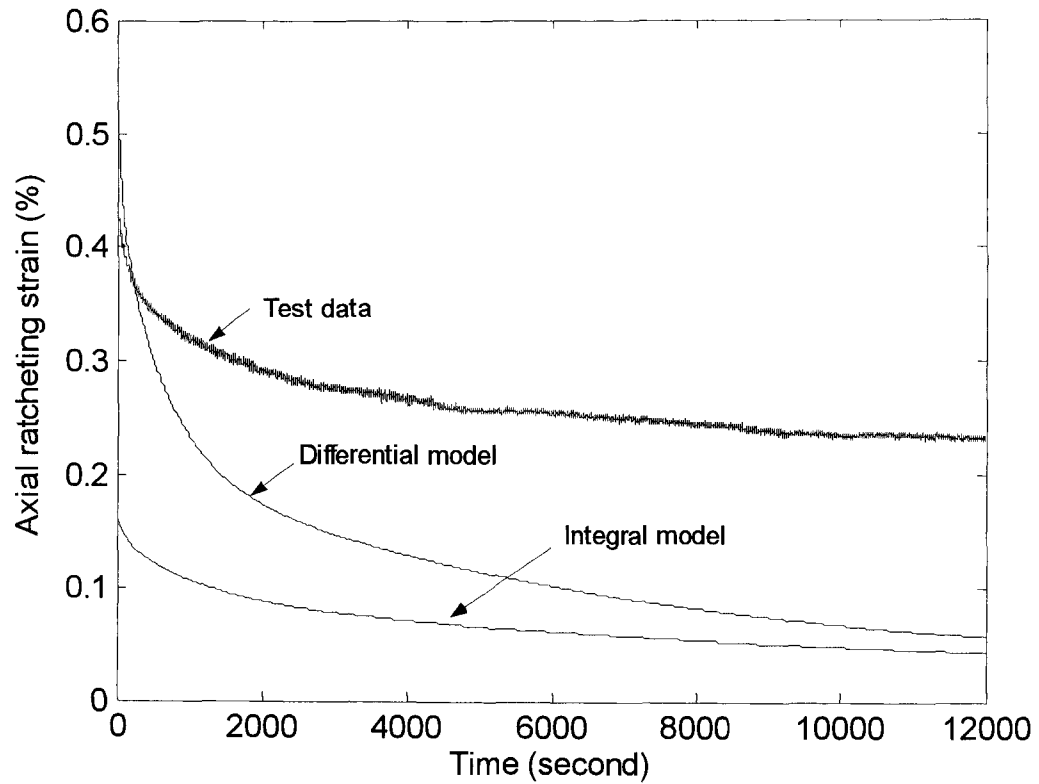


Figure 3.8 Ratcheting strain recovery after 20 cycles of preloading: comparison of test data with differential model predictions and integral model predictions.

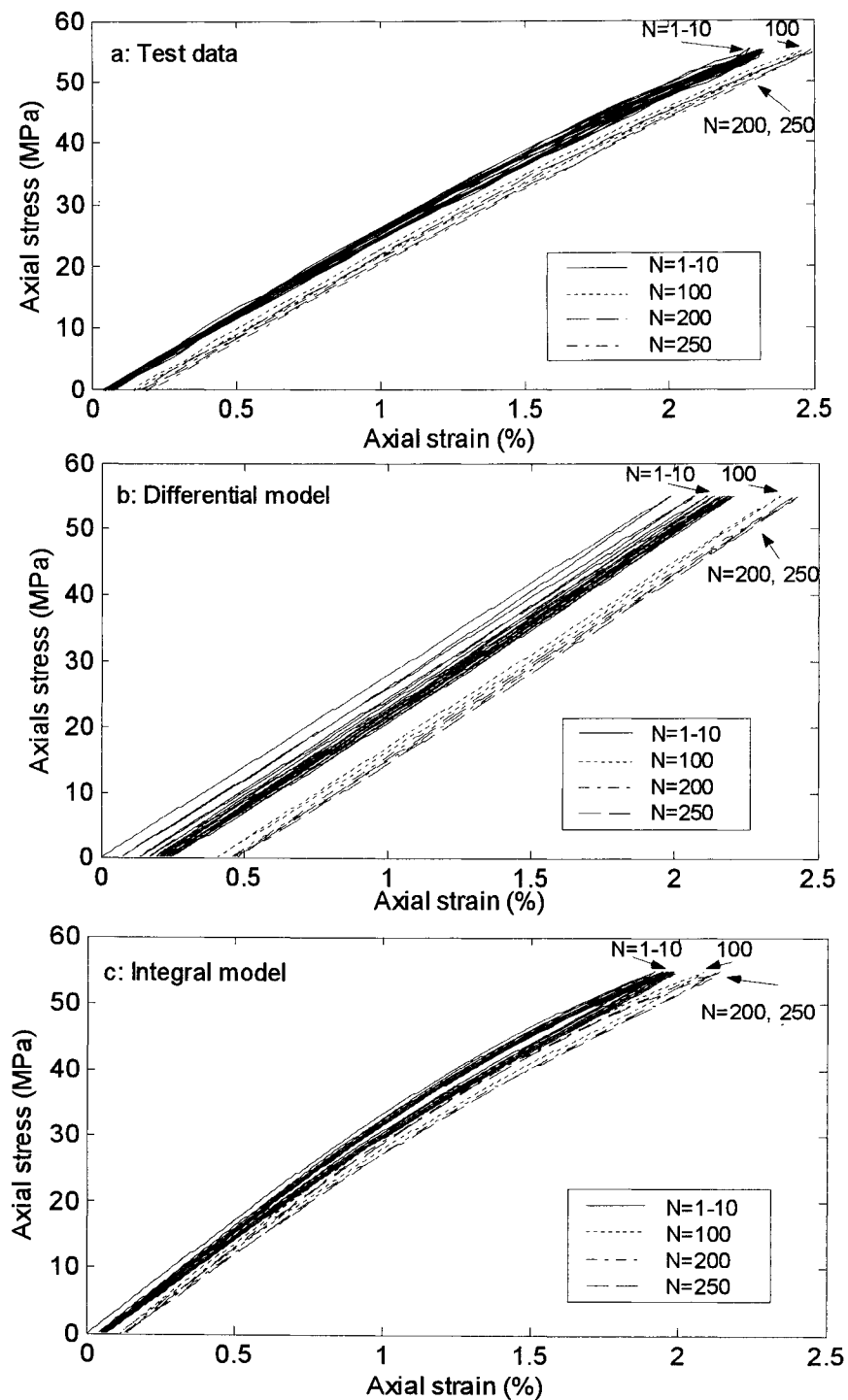


Figure 3.9 Stress-strain curves of stress-controlled test with a maximum applied stress of 55 MPa with a mean stress of 27.5 MPa and a stress rate of 24 MPa/s (a) test data, (b) differential model predictions and (c) integral model predictions.

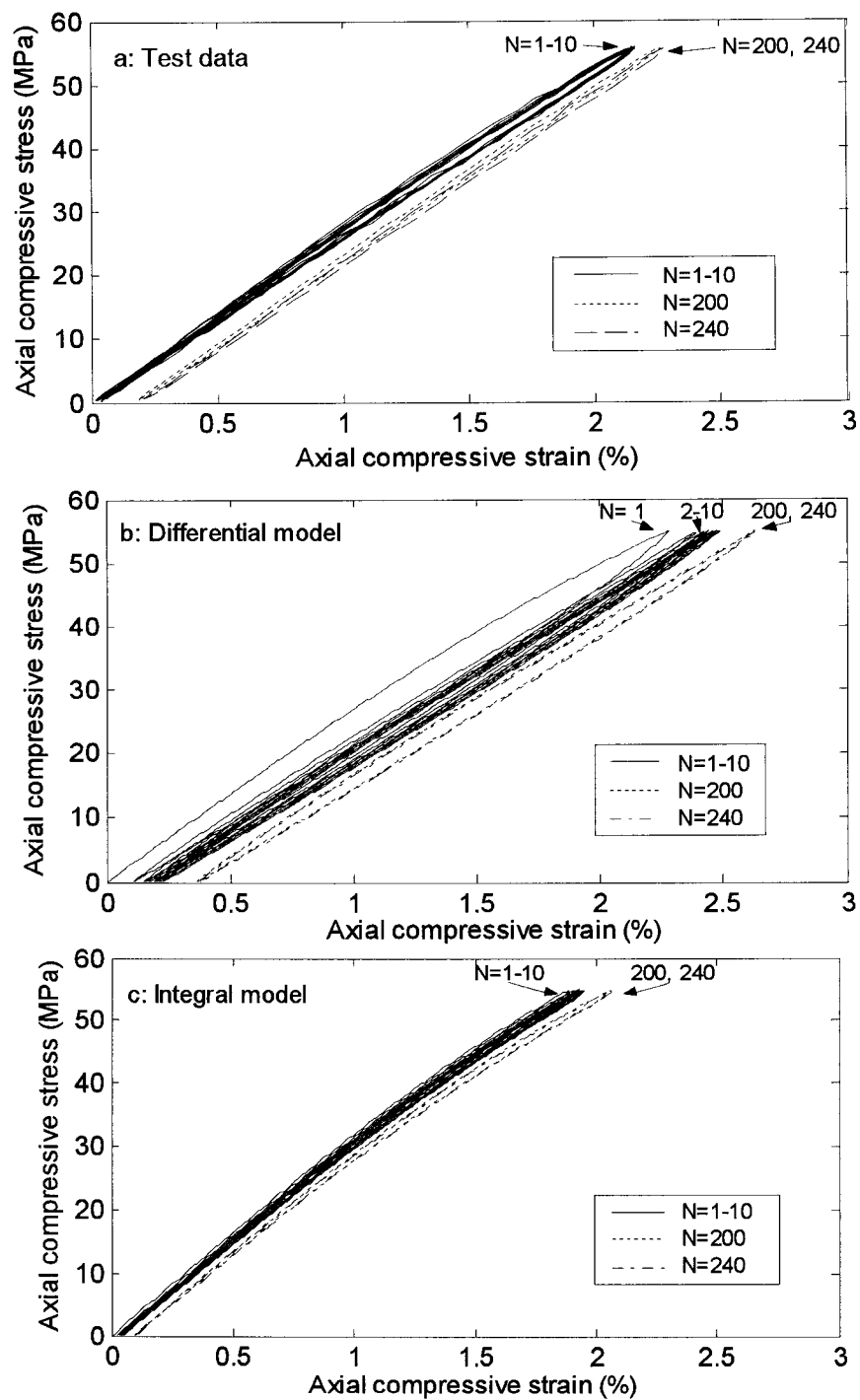


Figure 3.10 Stress-strain curves for a compressive cyclic loading with a stress range of 55 MPa and a mean stress of 27.5 MPa (a) test data, (b) differential model predictions and (c) integral model predictions.

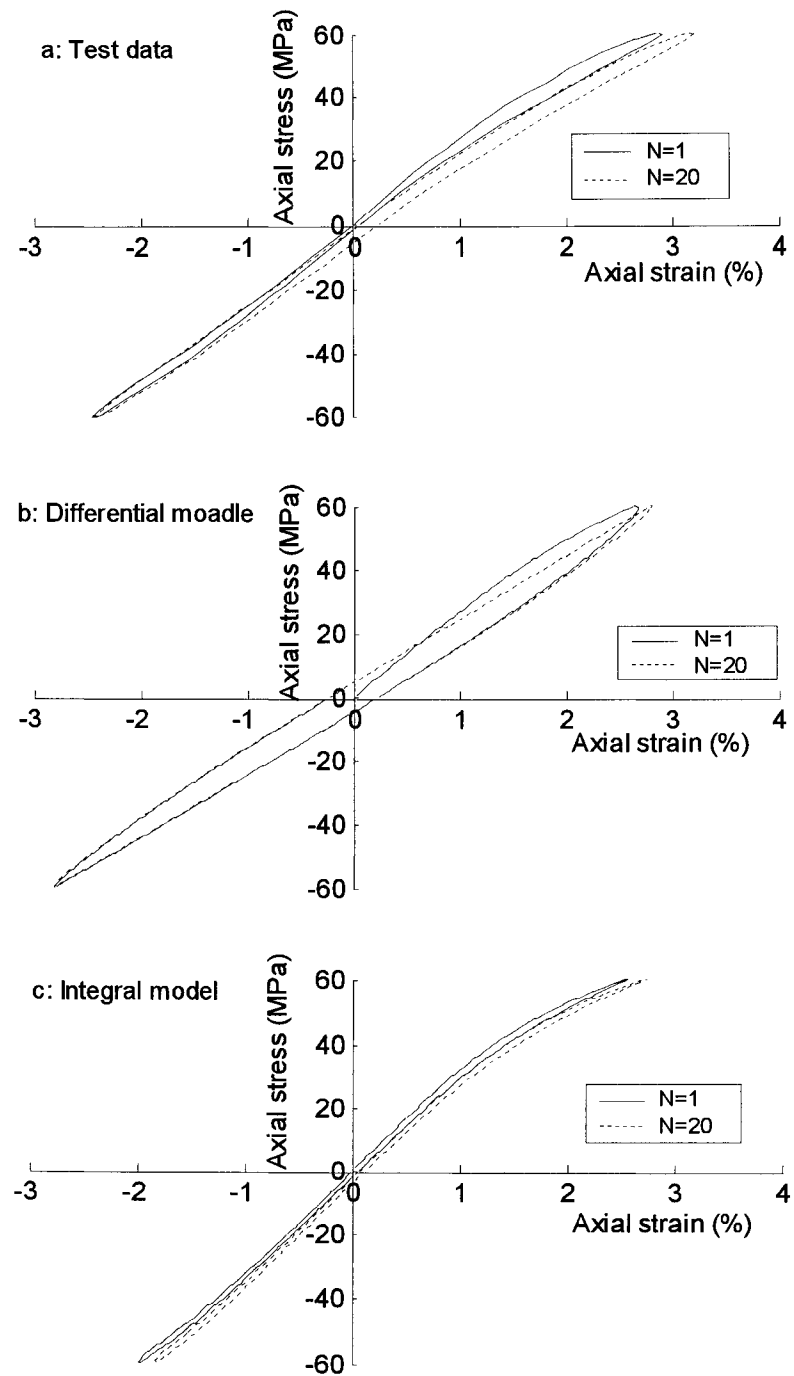


Figure 3.11 Stress-strain curves for a fully reversed cyclic loading with stress amplitude of 60 MPa (a) test data, (b) differential model predictions and (c) integral model predictions.

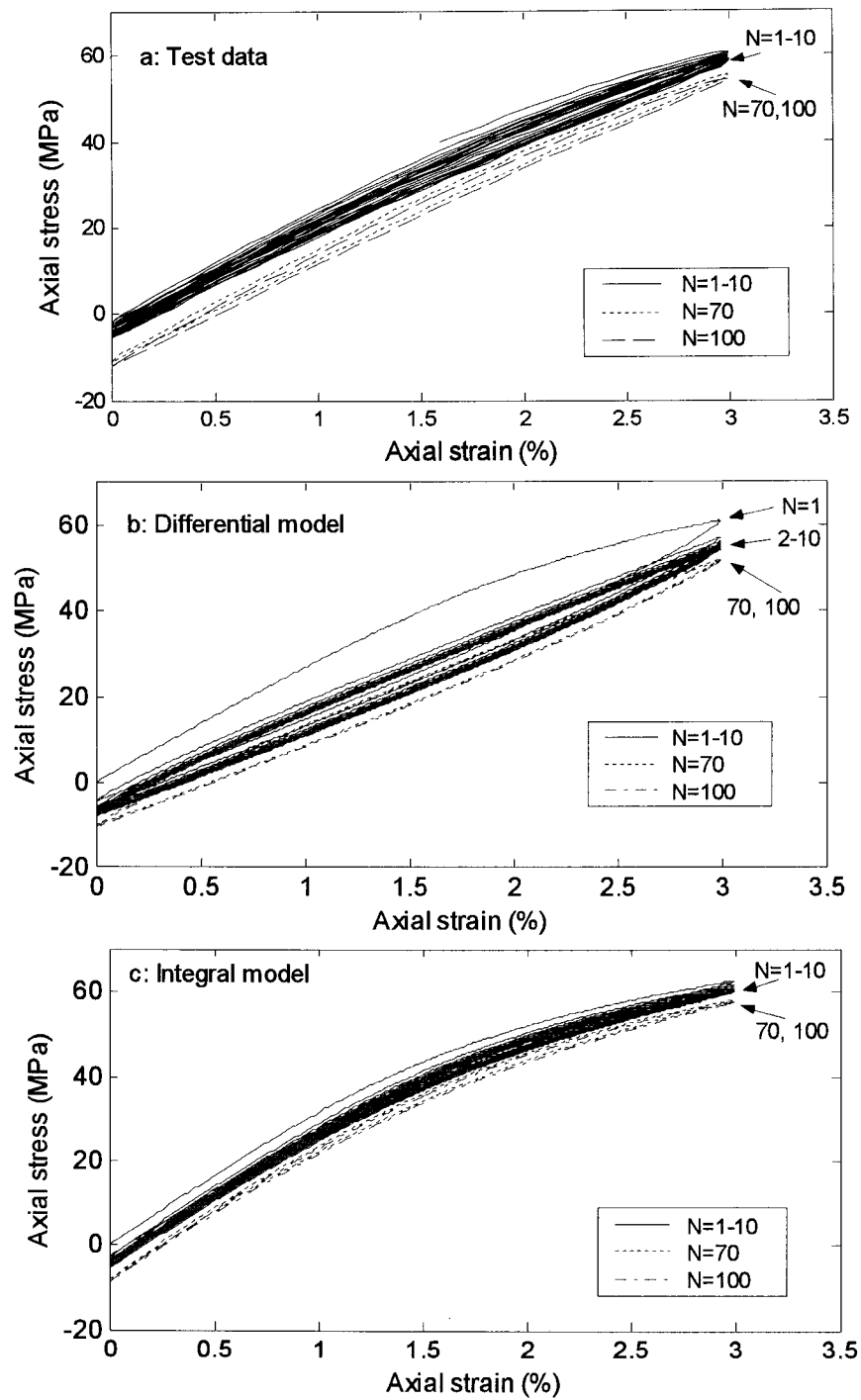


Figure 3.12 Stress-strain curves for a strain-controlled test with a maximum strain of 3% and a mean strain of 1.5% (a) test data, (b) differential model predictions and (c) integral model predictions.

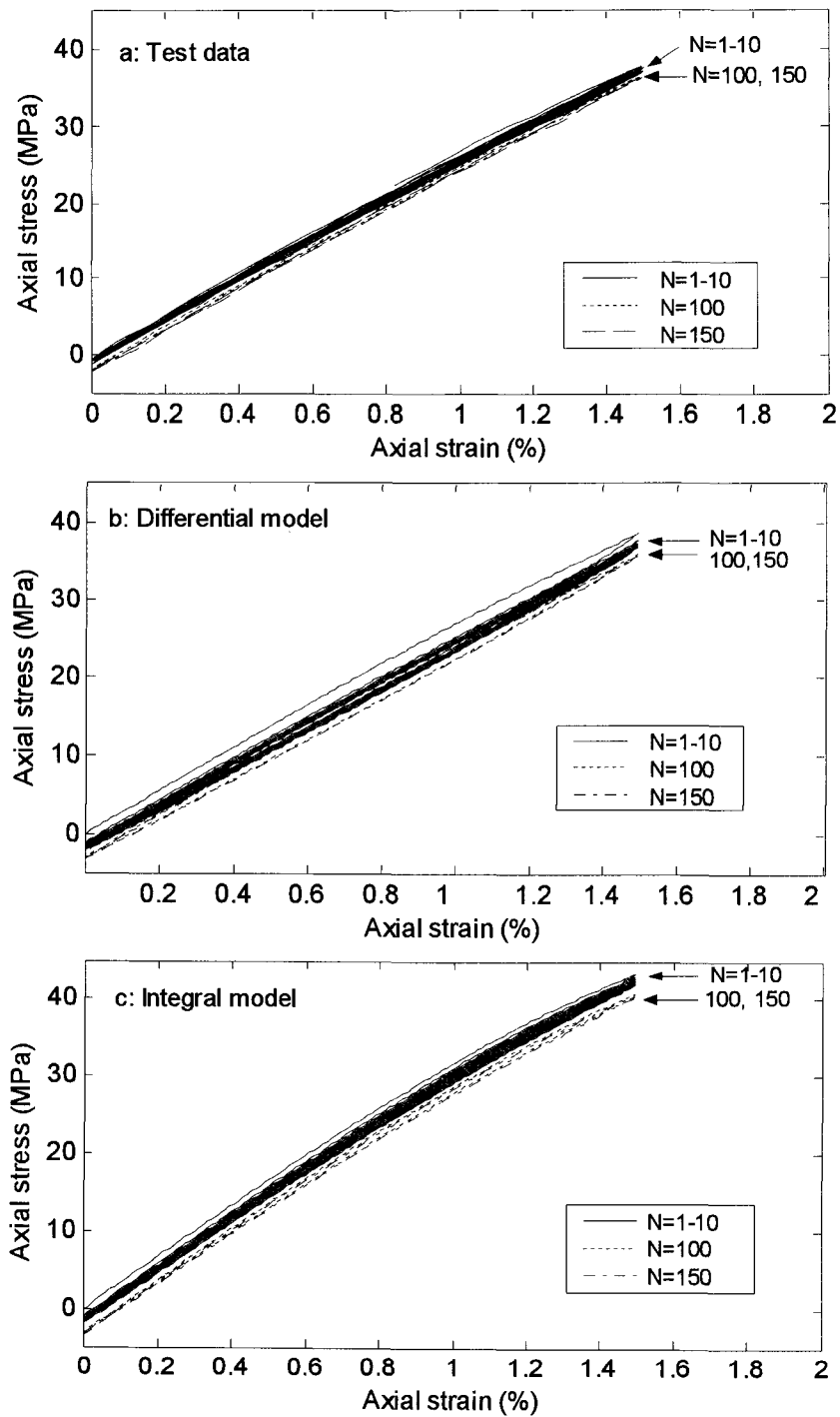


Figure 3.13 Stress-strain curves for a strain-controlled test with a maximum strain of 1.5% and a mean strain of 0.75% (a) test data, (b) differential model predictions and (c) integral model predictions.

Bibliography

1. K. W. Loh, A. A. O. Tay and S. H. Teoh, Effect of constitutive models on the numerical simulation of viscoelastic flow at an entry region. *Polym. Eng. Sci.*, **36**, 1990 (1996).
2. Ocsuki, T. Kajiwara and K. Funatsu, Numerical simulation of annular extrudate swell using various types of viscoelastic models. *Polym. Eng. Sci.*, **39**, 1969 (1999).
3. O. C. Zienkiewicz, M. Watson and I. P. King, A numerical method of visco-elastic stress analysis. *Int. J. Mech. Sci.*, **10**, 807 (1968).
4. D. G. Kubat, H. Bertilsson, J. Kubat, and S. Uggla, A simplified cooperative model of stress-relaxation and other consolidation processes in solids. *Rheol. Acta*, **31**, 390 (1992).
5. Z. Xia and F. Ellyin, Time-dependent behaviour and viscoelastic constitutive modelling of an epoxy polymer, *Polym. Polym. Compos.*, **6**, 75 (1998).
6. C. Zhang and I. D. Moore, Nonlinear mechanical response of high density polyethylene, Part II : uniaxial constitutive modeling. *Polym. Eng. Sci.*, **37**, 414 (1997).
7. Z. Xia, Y. Hu, and F. Ellyin, Deformation behavior of an epoxy resin subject to multiaxial loadings. Part II: constitutive modeling and predictions *Polym. Eng. Sci.*, **43**, 734 (2003).
8. R. A. Shapery, On the characterization of nonlinear viscoelastic materials. *Polym. Eng. Sci.*, **9**, 295 (1969).
9. J. Lai and A Bakker, 3-D schapery representation for non-linear viscoelasticity and finite element implementation, *Comput. Mech.*, **18**, 182 (1996).
10. K. G. Nolte and W. N. Findley, Multiple step, nonlinear creep of polyurethane predicted from constant stress creep by three integral representations. *Trans. Soc. Rheol.*, **15**, 111 (1971).
11. A. D. Drozdov and A. L. Kalamkarov, A constitutive model for non-linear viscoelastic behavior of polymers. *Polym. Eng. Sci.*, **36**, 1907 (1996).
12. A. A. Malmeister, Predicting the thermoviscoelastic strength of polymer materials in a complex stressed state. *Mech. Composite Mater.*, **21**, 768 (1985).
13. D. Peretz and Y. Weitsman, The nonlinear thermoviscoelastic characterizations of FM-73 Adhesives. *J. Rheol.* **27**, 97 (1983).
14. J. M. Augl, Nonlinear creep effects of physical aging, temperature and moisture of an epoxy

-
- resin. *J. Rheol.*, **31**, 1 (1987).
15. S. W. Park and R. A. Schapery, A viscoelastic constitutive model for particulate composites with growing damage. *Int. J. Solids Struct.*, **34**, 931 (1997).
 16. M. Henriksen, Nonlinear viscoelastic stress analysis – a finite element approach. *Comput. Struct.*, **18**, 133 (1984).
 17. Y. Hu, Z. Xia, and F. Ellyin, Deformation behavior of an epoxy resin subject to multiaxial loadings, Part I: experimental investigations. *Polym. Eng. Sci.*, **43**, 721 (2003).
 18. X. Shen, Z. Xia, and F. Ellyin, Cyclic deformation behavior of an epoxy polymer, Part I: experimental investigations. Submitted to *Polym. Eng. Sci.*.

Chapter 4

Biaxial Cyclic Deformation of an Epoxy Resin : Experiments and Constitutive Modeling

4.1 Introduction

Polymers and polymeric composites have become an important class of materials in engineering applications. Structures such as pressure vessels, piping and aircrafts, components like mountain bicycle frames and crankshafts are typical examples. In their service life, they are likely subjected to multiaxial stress state with complex loading histories and paths, and in many cases, loading is of a cyclic nature. Therefore, an adequate understanding of the deformation and failure behavior of polymeric materials is a prerequisite for an efficient design and optimal material utilization.

Due to the complex nonlinear viscoelastic nature of polymers, numerical simulations such as finite element method have been extensively used in the stress and deformation analyses of structures made of these materials. However, the reliability of such numerical predictions is highly dependent on the accuracy of the material's constitutive model used in the analysis [1-2]. Hence the development and verification of constitutive models is a matter of practical significance, and has attracted considerable research efforts in recent years, see e.g. refs. [3-7].

The material to be studied in this investigation is Epon 826/Epi-Cure Curing Agent 9551, a bisphenol-A epoxy resin and a non-MDA (methylene dianiline) polyamine system suitable for high performance composite parts manufactured by filament winding or resin transfer moulding. This epoxy system was chosen because it provides high strength, elongation and toughness, and therefore, is an appropriate matrix for high performance composite materials. The deformation behavior of this epoxy resin when subjected to quasi-static multiaxial loading and uniaxial cyclic loading, can be found in our previous investigations [8-9].

Although there have been numerous papers published concerning the multiaxial cyclic loading behavior of metals and alloys [10-12], the influence of such a loading condition on polymers has not been fully investigated. Experimental investigations on polymer behavior under cyclic loading were reported in refs. [13-16]. However, almost all of these investigations were for uniaxial cyclic tests on thermoplastic polymers. To the best of our knowledge, experimental data on the multiaxial cyclic deformation behavior of thermosetting polymers have not been reported in the open literature.

It is the objective of this chapter to present experimental data of the aforementioned epoxy resin under biaxial proportional and non-proportional cyclic loading conditions. The focus of the study is on the stress-strain response in axial and hoop directions and their dependency on the load control mode, stress or strain range and loading path. A viscoelastic constitutive model recently developed by Xia *et al.* [3] is briefly reviewed and used to simulate the experimental results. It will be seen later on that the constitutive model is capable of predicting the complex stress-strain response

and simulating most experimental observations under biaxial cyclic loading both qualitatively and quantitatively.

4.2 Test Set-up

4.2.1 Specimen and Testing Equipment

Thin-walled tubular specimens were used in this investigation. The procedure for the casting and preparation of specimens can be found in ref. [9]. Aluminum end tabs were glued to the tube ends so that the specimen can be inserted into the gripping system of the test machine without damaging the specimen extremities during the gripping process. Figure 4.1 shows the geometry of the tubular specimen with the aluminum end tabs.

All experiments were performed in a servo-controlled electro-hydraulic system, a modified MTS system. The system is capable of applying axial force; internal and external pressure separately or simultaneously. Thus, uniaxial or biaxial stress state can be generated in the specimen. Detailed description of the test system can be found in [17]. The strains were measured using in-house manufactured axial and diametral extensometers.

4.2.2 Experimental Program and Testing Procedure

The experimental program consisted of biaxial proportional (equi-biaxial) and non-proportional cyclic tests. Thin-walled tubular specimens were subjected to axial loading and internal pressure following predetermined strain or stress cyclic paths. The loading conditions for each type of test are summarized in Table 1.

For the proportional (equi-biaxial) cyclic tests with mean stresses or mean strains, the specimens were first loaded biaxially to the mean stress or mean strain level and then cyclic testing commenced. In addition, a triangular waveform was adopted in both channels (axial and hoop) for the proportional cyclic tests.

In the case of non-proportional cyclic loading, the test started from a stress-free (virgin) state. A quarter-circle sectorial non-proportional cyclic loading path was employed. The loading path and the corresponding input signals for axial and hoop directions are depicted in Fig. 4.2. The stress or strain waves can be represented by:

$$I_a = \begin{cases} A \sin\left(\frac{3\pi}{2} \omega t\right), & \left(\frac{n}{\omega} \leq t < \frac{2}{3\omega} + \frac{n}{\omega}\right) \\ 0, & \left(\frac{2}{3\omega} + \frac{n}{\omega} \leq t < \frac{n+1}{\omega}\right) \end{cases} \quad n = 0, 1, 2, 3 \dots \quad (1)$$

$$I_h = I_a\left(t - \frac{\pi}{2}\right) \quad (2)$$

Where I_a and I_h refer to the axial and hoop input signal, respectively. A is the amplitude of the stress or strain, ω is the frequency of oscillation and t is the time.

The loading rates for the tests were selected in a range that they allowed for the manifestation of the time-dependent behavior of the material yet avoided the excessive heating of the specimen during cycling. All the tests were conducted at room temperature under the laboratory environment. For most cyclic tests, the stress-strain hysteresis loops were recorded for the initial 10 cycles after which they were recorded at each 10-cycle interval until the specimen failure.

4.3 Test Results

4.3.1 Proportional (equi-biaxial) Cyclic Loading under Strain-control

Strain-controlled equi-biaxial cyclic tests were conducted with two different strain ranges, $\Delta\varepsilon_a = \Delta\varepsilon_h = 1.5\%$ and $\Delta\varepsilon_a = \Delta\varepsilon_h = 3\%$. A strain rate of $1.2 \times 10^{-4} \text{ s}^{-1}$ in both axial and hoop directions was adopted for these two tests. Figures 4.3a ; 4.3b and Figs. 4.4a ; 4.4b show the experimental stress-strain loops, respectively. For comparative purpose, the hysteresis loop of the first cycle and that of N=15 (last recorded cycle prior to specimen failure) for the large strain range test ($\Delta\varepsilon_a = \Delta\varepsilon_h = 3\%$) are depicted in Figs. 4.5a and 4.5b.

From these test results, we see that the hysteresis loops in the axial and hoop directions, as to be expected, are almost similar, indicating an isotropic property of the material. With the small strain range, Figs. 4.3a and 4.3b, the stress-strain loops exhibit an insignificant amount of nonlinear response and the specimen failed after 120 cycles. With the increasing number of cycles, the hysteresis loops became slimmer. This phenomenon is particularly evident with the higher strain range of 3%, Figs. 4.4a and 4.4b, which exhibited pronounced nonlinear response. One observed that the difference between the initial cycle and that of N=15 was a much slimmer and less nonlinear hysteresis loop prior to specimen failure compared to that of the initial cycle, c.f. Figs. 4.5a and 4.5b. For both tests, a mean stress relaxation occurred in both axial and hoop directions. With the increasing number of cycles, the mean stress appeared to approach an asymptotic value, indicating the attainment of a stable cyclic state. However, the magnitude of mean stress reduction is significantly different for the two tests. In the

case of the small strain range of $\Delta\varepsilon_a = \Delta\varepsilon_h = 1.5\%$, the mean stress drop was approximately 4 MPa during the entire cycling process, while for the higher strain range of $\Delta\varepsilon_a = \Delta\varepsilon_h = 3\%$, the mean stress was reduced by 12 MPa from approximately 34 MPa at the first cycle to about 22 MPa at $N=15$ (prior to fracture), c.f. Fig. 4.6.

4.3.2 Proportional (equi-biaxial) Cyclic Loading under Stress-control

Further stress-controlled equi-biaxial cyclic tests were performed with two different stress ranges, $\Delta\sigma_a = \Delta\sigma_h = 40\text{MPa}$ and $\Delta\sigma_a = \Delta\sigma_h = 60\text{MPa}$. The stress rates were chosen to achieve an approximate strain rate of $1.2 \times 10^{-4} \text{ s}^{-1}$ for the two tests. The stress-strain curves of these tests are shown in Figs. 4.7a ; 4.7b and Figs. 4.8a ; 4.8b. Again, the first hysteresis loop, that of the stable cyclic state and the one prior to the specimen fracture were depicted in Figs. 4.9a and 4.9b for the sake of comparison.

For both tests, it was observed that the ratcheting deformation (cyclic creep) accumulated in both axial and hoop directions from the onset of cyclic loading, but in a decreasing rate with the increasing number of cycles. After certain number of cycles ($N=200$ for the small stress range of $\Delta\sigma_a = \Delta\sigma_h = 40\text{MPa}$, and $N=60$ for the large stress range of $\Delta\sigma_a = \Delta\sigma_h = 60\text{MPa}$), the ratcheting rate tended to zero and a saturated stress-strain response was attained. It was also noticed that during the cycling process, the slope of the hysteresis loops in both axial and hoop directions did not decrease appreciably, i.e. the stiffness reduction was very small.

In comparing the stress-strain loops with two different stress ranges, it was observed that the higher the stress range, the higher is the accumulated ratcheting strain.

For the large stress range of $\Delta\sigma_a = \Delta\sigma_h = 60\text{MPa}$, the ratcheting strain at stable cyclic state reached approximately 0.5%, while it was less than 0.1% for the small stress range of $\Delta\sigma_a = \Delta\sigma_h = 40\text{MPa}$. It is seen from Figs. 4.7a and 4.7b that with the small stress range, the hysteresis loops are almost linear in shape throughout the test. The nonlinear stress-strain response was more pronounced for the applied stress range of 60 MPa in both principal directions, as shown in Figs. 4.8a and 4.8b. From Figs. 4.9a and 4.9b, one can also observe the difference between the stress-strain curves at the first cycle and that at the stable cyclic state. That is, there is an evolution of hysteresis loops towards a slimmer stable shape.

4.3.3 Non-proportional quarter-circle sectorial cyclic loading under strain-control

Figures 4.10a; 4.10b and Figures 4.11a; 4.11b show the hysteresis loops of the strain-controlled non-proportional cyclic loading with two different strain ranges, $\Delta\varepsilon_a = \Delta\varepsilon_h = 1.5\%$ and $\Delta\varepsilon_a = \Delta\varepsilon_h = 3\%$, respectively. As before, the first hysteresis loops and the last one prior to specimen failure with the higher strain range of $\Delta\varepsilon_a = \Delta\varepsilon_h = 3\%$ are depicted in Figs. 4.12a and 4.12b for a better comparison.

From the above test results, it is noted that there is anisotropy of stress-strain responses in axial and hoop directions induced by the non-proportional cyclic loading path. That is, the axial hysteresis loops are narrower in size than that of hoop ones, c.f. Figs 4.10a with 4.10b and Fig. 4.11a with 4.11b. This is particularly true with the high applied strain in Figs. 4.11 and 4.12. In addition, the axial and hoop hysteresis loops

rotate in opposite directions, i.e. axial loops rotate in the counter-clockwise while the hoop ones in the clockwise.

Under strain-controlled cyclic loading, the uncontrolled stress components gradually decrease in magnitude with the increasing number of cycles. They asymptotically reach a stable level after certain number of cycles (N=100 with the strain range of $\Delta\varepsilon_a = \Delta\varepsilon_h = 1.5\%$ and N=20 with that of $\Delta\varepsilon_a = \Delta\varepsilon_h = 3\%$). In the case of the test with the strain range of $\Delta\varepsilon_a = \Delta\varepsilon_h = 3\%$, Fig. 4.13a depicts the cyclic strain path and Fig. 4.13b shows the cone-shaped stress responses in the $\sigma_a - \sigma_h$ stress plane.

4.3.4 Non-proportional quarter-circle sectorial cyclic loading under stress-control

Stress-controlled non-proportional cyclic tests with two different stress ranges, $\Delta\sigma_a = \Delta\sigma_h = 40MPa$ and $\Delta\sigma_a = \Delta\sigma_h = 60MPa$, were performed. The hysteresis loops are shown in Figs. 4.14a ; 4.14b, and Figs. 4.15a ; 4.15b. One observes the anisotropy of stress-strain responses in axial and hoop directions induced by the non-proportional cyclic loading path. Again, the axial and hoop hysteresis loops rotate in opposite directions. Under this loading condition, the uncontrolled strain components show a fan-shaped response in $\varepsilon_a - \varepsilon_h$ plane as portrayed in Fig. 4.16b.

With the small applied stress range in Figs. 4.14a and 4.14b, a small ratcheting strain was accumulated in both axial and hoop directions. After about 200 cycles, a cyclic stable state was reached. The specimen did not fail even after 400 cycles. When the stress range was increased to $\Delta\sigma_a = \Delta\sigma_h = 60MPa$, Figs. 4.15a and 4.15b,

ratcheting became more significant, especially in the hoop direction. Due to the high cyclic stress range, the specimen failed after only 10 cycles. Neither a decreasing ratcheting rate nor a saturated stress-strain response was observed in this case.

4.4 Constitutive Modeling and Predictions

4.4.1 Description of Constitutive Model

A recently proposed rheological nonlinear viscoelastic constitutive model was employed in this study to simulate the experimental observations. The fundamental equations of the constitutive model will be reviewed and a criterion to distinguish loading/unloading will be discussed. This criterion has been found to play an important role in simulating material behavior under cyclic loading, see ref. [18]. Other details of the constitutive model can be found in [3].

The model is in differential form. It can be viewed as a combination of one linear spring and several nonlinear Kelvin (Voigt) elements in series in its uniaxial representation. It is assumed that the total strain rate, $\{\dot{\epsilon}_t\}$, is the sum of the elastic and the creep strain rates, $\{\dot{\epsilon}_e\}$ and $\{\dot{\epsilon}_c\}$, respectively, i.e.

$$\{\dot{\epsilon}_t\} = \{\dot{\epsilon}_e\} + \{\dot{\epsilon}_c\} \quad (3)$$

The elastic strain rate is calculated through the generalized Hooke's law,

$$\{\dot{\sigma}\} = E[A]^{-1}\{\dot{\epsilon}_e\} \quad (4)$$

where $[E]$ is the elastic modulus, $[A]$ is a matrix related to the value of Poisson's ratio and defined by

$$[A] = \begin{bmatrix} 1 & -\nu & -\nu & 0 & 0 & 0 \\ -\nu & 1 & -\nu & 0 & 0 & 0 \\ -\nu & -\nu & 1 & 0 & 0 & 0 \\ 0 & 0 & 0 & 1+\nu & 0 & 0 \\ 0 & 0 & 0 & 0 & 1+\nu & 0 \\ 0 & 0 & 0 & 0 & 0 & 1+\nu \end{bmatrix} \quad (5)$$

For a number of Kelvin (Voigt) elements connected in series, creep strain rate is the sum of the creep strain rate of each element, i.e.

$$\{\dot{\varepsilon}_c\} = \sum_{i=1}^n \{\dot{\varepsilon}_{ci}\} = \sum_{i=1}^n \left(\frac{[A]}{E_i \tau_i} \{\sigma\} - \frac{1}{\tau_i} \{\varepsilon_{ci}\} \right) \quad (6)$$

where $\tau_i = \eta_i / E_i$ denotes the retardation time, η_i is the dashpot viscosity and E_i is the spring stiffness for the i -th Kelvin (Voigt) element, respectively. It is to be noted that $E_i = E_1(\sigma_{eq})$, which has a damped exponential character as in an exponential-type function of the “equivalent” stress. We further introduce a time scale factor α , and assume

$$\tau_i = (\alpha)^{i-1} \tau_1. \text{ In this way all } \tau_i \text{ are related}$$

through the scale factor α . The anisotropy between tension and compression behavior of polymers is defined by R which is the ratio of the yield stress in compression to tension.

To suit more general (proportional or non-proportional) cyclic loading paths, a rule to distinguish loading/unloading is further modified by defining a stress memory surface (Fig. 4.17):

$$f_m^\sigma(\sigma_{ij}) - R_{\max}^2 = \frac{3}{2} s_{ij} s_{ij} - R_{\max}^2 = 0 \quad (7)$$

where $s_{ij} = \sigma_{ij} - \frac{1}{3}\sigma_{kk}$ is the deviatoric stress components. The radius of the memory surface, R_{mem} , is determined by the maximum von Mises equivalent stress level experienced by the material during its previous loading history, i.e.

$R_{mem} = \sqrt{\frac{3}{2}(s_{ij} s_{ij})_{max}}$. The following rules are adopted:

- if the current stress point is *on the memory surface* and $(\frac{\partial f}{\partial \sigma_{ij}})_{\sigma_{ij}^t} \cdot d\sigma_{ij}^t \geq 0$, this signifies a loading case;
- if the current stress point is *on the memory surface* and $(\frac{\partial f}{\partial \sigma_{ij}})_{\sigma_{ij}^t} \cdot d\sigma_{ij}^t < 0$, then a switch from loading to unloading occurs;
- if the current stress point is *inside the memory surface*, i.e. $f_m^\sigma(\sigma_{ij}^t) - R_{max}^2 < 0$, it is then an unloading case.

For the loading case the spring stiffness of the Kelvin elements is defined as a function of the equivalent stress, $E_i = E_1(\sigma_{eq})$. For the unloading case, it is assumed that E_i remains the same value during the entire unloading process, which is equal to the value of E_i at the switch point, where unloading takes place.

The detailed procedure for the determination of the material constants and the modulus function can be found in ref. [3]. The parameters used in this study are listed as follows:

$$E = 2800 \text{ MPa}, \nu = 0.42, \alpha = 10, \tau_1 = 6.116 \text{ s}, R = 1.15, n = 6 \text{ and}$$

$$E_1(\sigma) = 1.055 \times 10^5 e^{\frac{\sigma - 22.764}{18.000}} \text{ MPa}$$

4.4.2 Comparison with Experimental Data

The predicted stress-strain loops for the equi-biaxial strain-controlled loading conditions are depicted in Figs. 4.3c; 4.3d, 4.4c; 4.4d and 4.5c; 4.5d. The model predicts a mean stress relaxation in both axial and hoop directions. Quantitative comparison also shows a good agreement with the experimental data. As mentioned earlier, for the cyclic test with a mean stress or mean strain, the specimen was first loaded to the mean stress or mean strain level and thereafter cyclic loading commenced. Hence, in the Figs. 4.4 and 4.5, for example, the cycling process starts at the mean strain value of 1.5%, while the model predictions always start at the stress-free (virgin) state.

Figures 4.7-4.9 compares the experimental data with the predictions of the constitutive model in the case of stress-controlled equi-biaxial cyclic loading. It is observed that the constitutive model simulated well the ratcheting behavior, i.e. with the increasing number of cycles, the predicted ratcheting rate decreases and the stress-strain hysteresis loops gradually reach a saturated state, a phenomenon observed by experiments, c.f. Figs. 4.7c ; 4.7d with 4.7a ; 4.7b, and 4.8c ; 4.8d with 4.8a ; 4.8b. The predicted magnitudes of accumulated ratcheting strains are comparable with the experimental data. In addition, the predicted stress-strain evolution process, i.e. hysteresis loops becoming slimmer with cycling, is also consistent with the experimental observations, c.f. Figs. 4.9c ; 4.9d with 4.9a ; 4.9b.

The predictions of the non-proportional strain-controlled cyclic loading are depicted in Figs. 4.10-4.13. In contrast to the proportional (equi-biaxial) loading, one notes two different manifestations induced by the non-proportional cyclic path: (a) the axial and hoop stress-strain loops are different in size and shape, and; (b) the axial and hoop hysteresis loops rotate in opposite directions. The constitutive model did predict the above two characteristics for this non-proportional loading path. The model also correctly simulated the decrease of stress values with the increasing cycles, and the predicted magnitude of reduction of stress components was very close to the experimental data, c.f. Figs. 4.12c ; 4.12d with 4.12a ; 4.12b.

In the case of non-proportional cyclic loading under stress-controlled mode, Figs. 4.14-4.16, the predictions by the constitutive model are also satisfactory both with respect to the primary stress-strain responses (size and shape of hysteresis loops) and the ratcheting behavior. It should be pointed out that for the stress range of $\Delta\sigma_a = \Delta\sigma_h = 60\text{MPa}$, Fig. 4.15, the stress range in hoop direction of the first cycle in test, Fig. 4.16b, was approximately 53 MPa, below the desired value of 60 MPa, but it was subsequently corrected to achieve the desired value. The model prediction for the hoop direction in this case was simulated exactly as the experimental loading conditions.

In view of the above detailed comparison between model predictions and the test data, it is seen that the model is capable of simulating most of the features observed in experiments, such as ratcheting, mean stress relaxation, stress-strain curves evolution towards a cyclic stable regime and path-dependent behavior. In simulating the first hysteresis loop and loops close to or after the attainment of cyclic stable state,

qualitative and quantitative agreement between model prediction and the test data were observed, cf. 4.5 and Fig. 4.9. However, for cycles from two to ten, the model predictions did not match very well with the experimental data. According to the loading/unloading rule, in most loading cases, the unloading portions began when specimen reached maximum equivalent stress in the first loading cycle. Hence, in model predictions, a dramatic transition between the first and the second loop was followed by a thereafter gradual transition. In tests, the first hysteresis loop differed most from the second one, and from second one to the tenth cycle, the hysteresis loops differed less among them. However, the overall transition process in the first ten cycles was still smooth and gradual. Such discrepancy between model predictions and test data in predicting the first 10 cycles needs to be addressed in future modification of the constitutive model.

4.5 Conclusions

From the results of biaxial cyclic tests and the comparison of the constitutive model predictions with the test data, the following conclusions are drawn:

1. Under strain-controlled proportional (equi-biaxial) cyclic loading with mean strain, there is a mean stress relaxation in both axial and hoop directions. The mean stress of the cyclic straining as well as the hysteresis loops reaches a stable state with increasing number of cycles.
2. Under stress-controlled proportional (equi-biaxial) cyclic loading with a mean stress, ratcheting strains are accumulated in both axial and hoop directions. The ratcheting rate decreases with the increasing number of cycles and the hysteresis

loops become slimmer and less nonlinear until the attainment of a cyclic stable state.

3. Under non-proportional cyclic loading path, anisotropy in stress-strain responses in the axial and hoop directions is noted and these hysteresis loops rotate in opposite directions. Under strain-controlled cyclic loading, the uncontrolled stress components gradually decrease in magnitude with the increasing number of cycles. They asymptotically reach a stable level after certain number of cycles. Under stress-controlled cyclic loading, a mean stress relaxation occurs in both axial and hoop directions.
4. Test results were used to verify the predictive capabilities of a constitutive model. This comparison indicated that the constitutive model is capable of simulating most experimental observations, e.g. mean stress relaxation and ratcheting strain accumulation. Even in the case of complex non-proportional cyclic loading paths, the constitutive model simulated quite well the experimental results qualitatively and quantitatively.

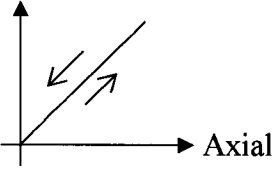
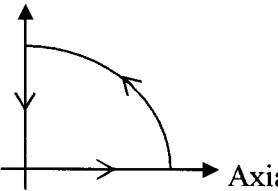
Loading path	Control mode	Stress or strain range	Mean stress or strain	Loading rate or frequency
Proportional (equi-biaxial) Hoop 	Strain control	1.5 %	0.75 %	$1.2 \times 10^{-4} \text{ s}^{-1}$
		3 %	1.5 %	$1.2 \times 10^{-4} \text{ s}^{-1}$
	Stress control	40 MPa	20 MPa	0.24 MPa/s
		60 MPa	30 MPa	0.32 MPa/s
Non-proportional Hoop 	Strain control	1.5 %	0.75 %	0.004 Hz
		3 %	1.5 %	0.002 Hz
	Stress control	40 MPa	20 MPa/s	0.004 Hz
		60 MPa	30 MPa/s	0.002 Hz

Table 4.1 Loading conditions of the biaxial cyclic test program.

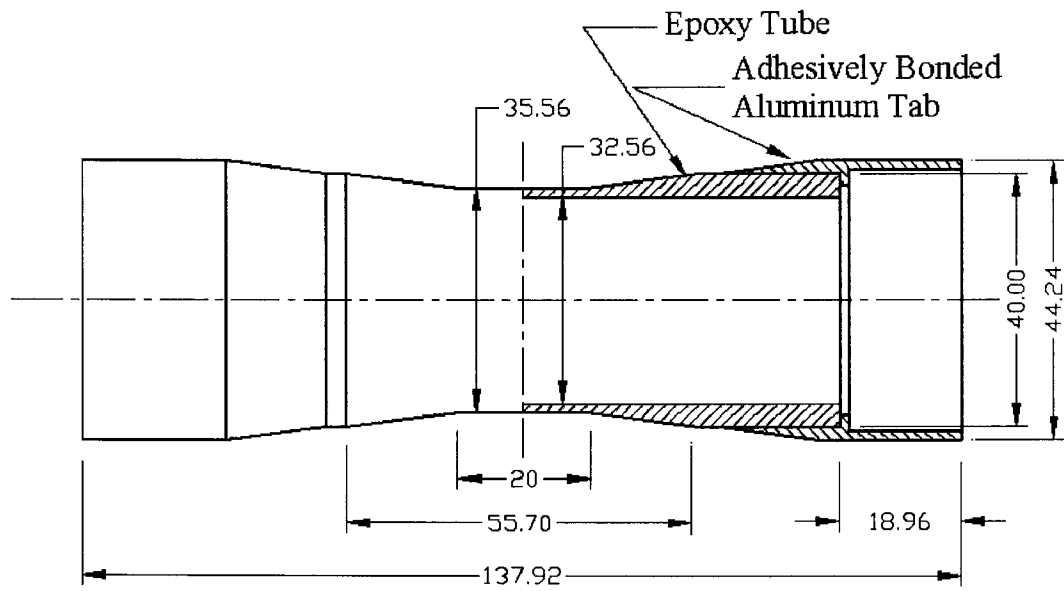


Figure 4.1 Geometry of tubular specimen with aluminum end tabs

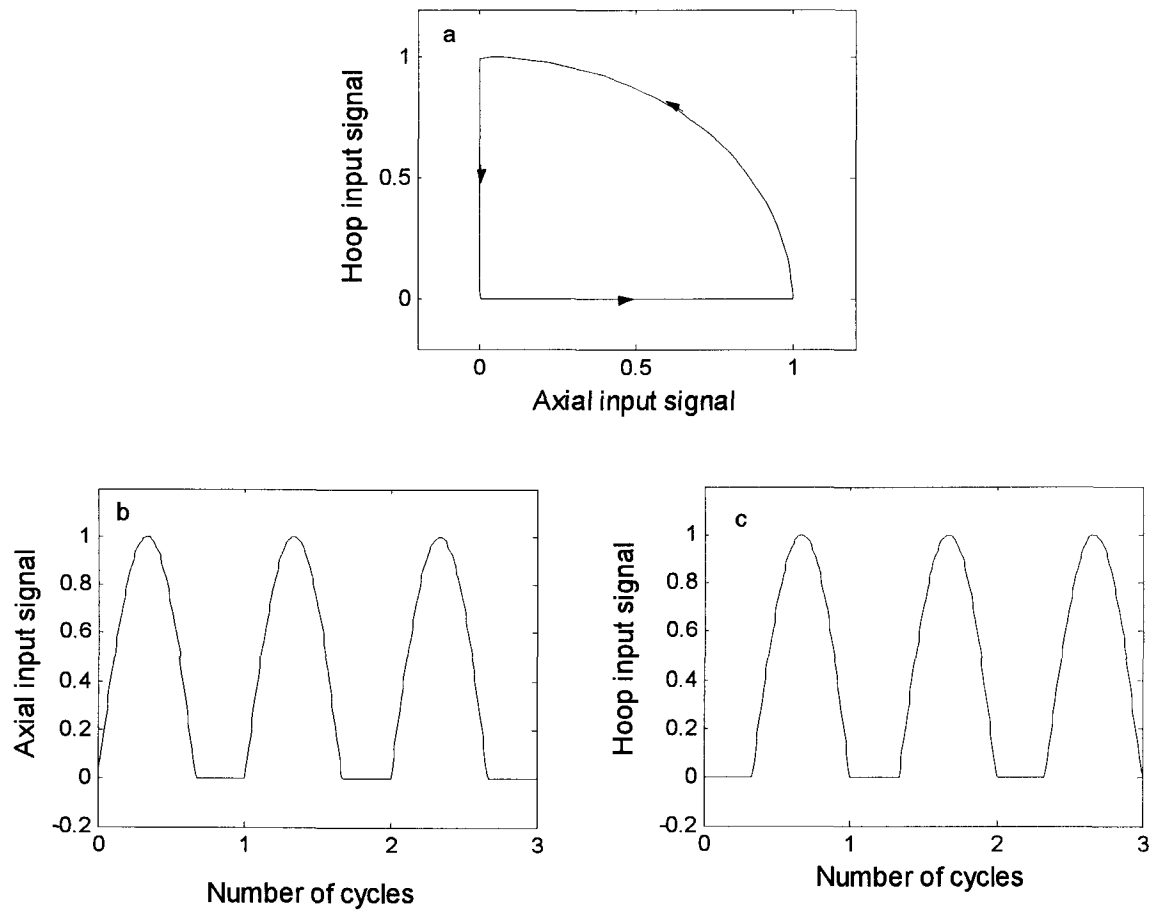


Figure 4.2 Non-proportional loading path and the corresponding input signals for axial and hoop directions: (a) quarter-circle sectorial cyclic loading path, (b) Axial input signal wave and (c) Hoop input signal wave

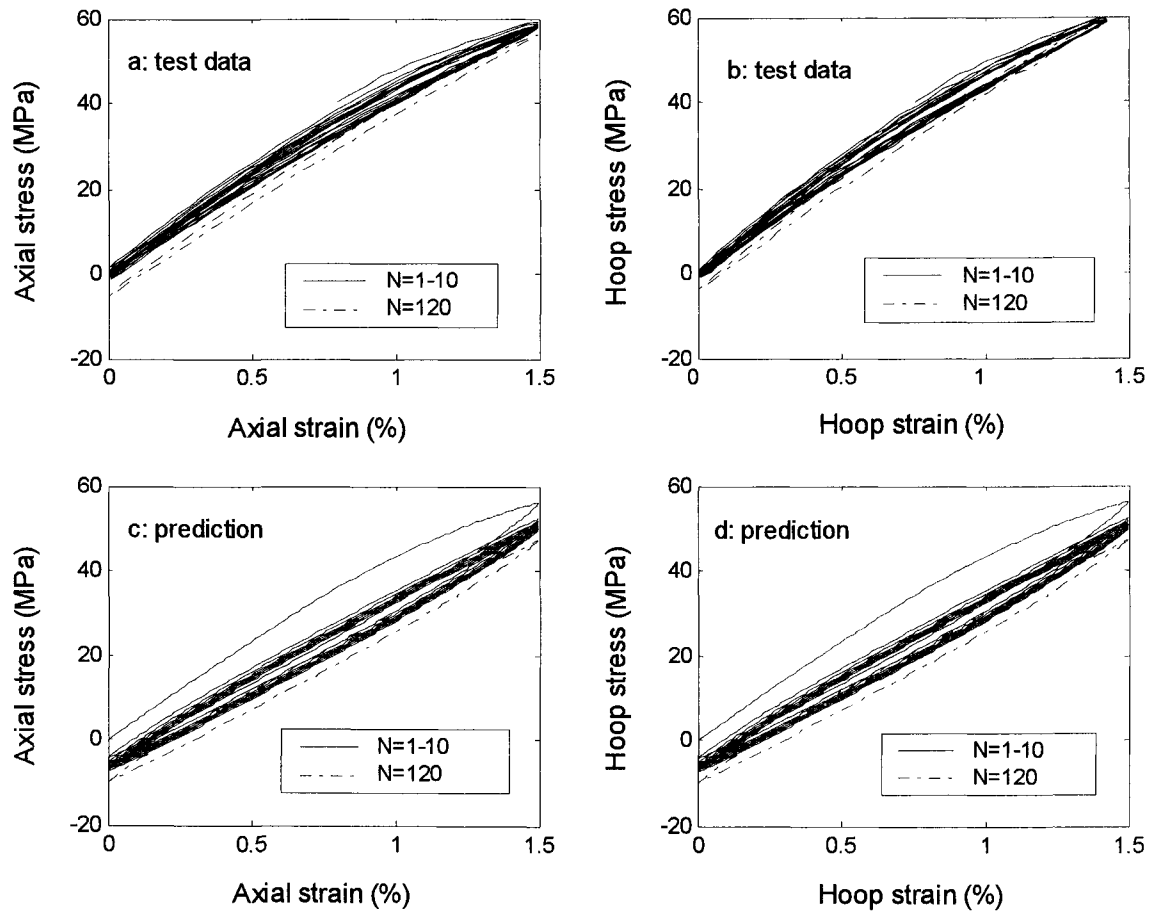


Figure 4.3 Strain-controlled proportional (equi-biaxial) cyclic loading with strain range of $\Delta\varepsilon_a = \Delta\varepsilon_h = 1.5\%$: (a) experimental axial stress-strain response, (b) experimental hoop stress-strain response, (c) predicted axial stress-strain response and (d) predicted hoop stress-strain response

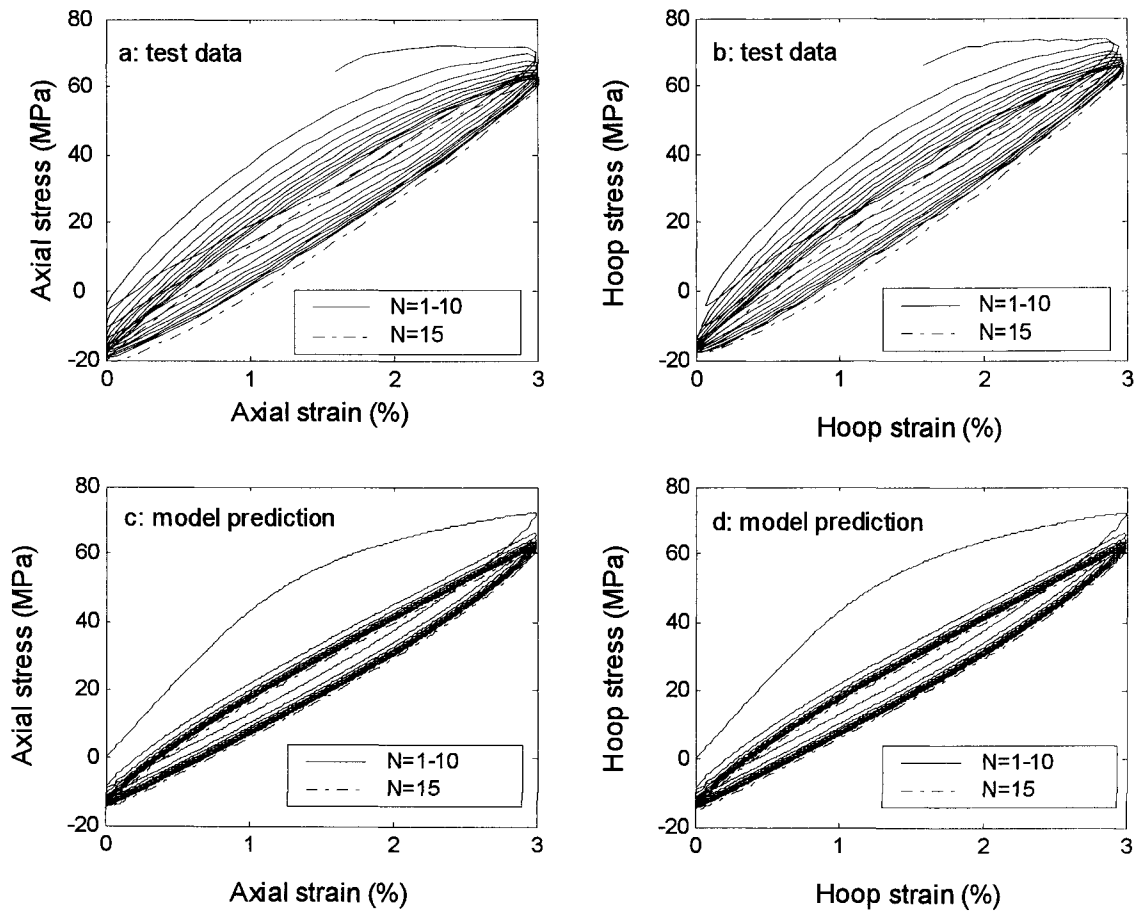


Figure 4.4 Strain-controlled proportional (equi-biaxial) cyclic loading with strain range of $\Delta\varepsilon_a = \Delta\varepsilon_h = 3\%$: (a) experimental axial stress-strain response, (b) experimental hoop stress-strain response, (c) predicted axial stress-strain response and (d) predicted hoop stress-strain response

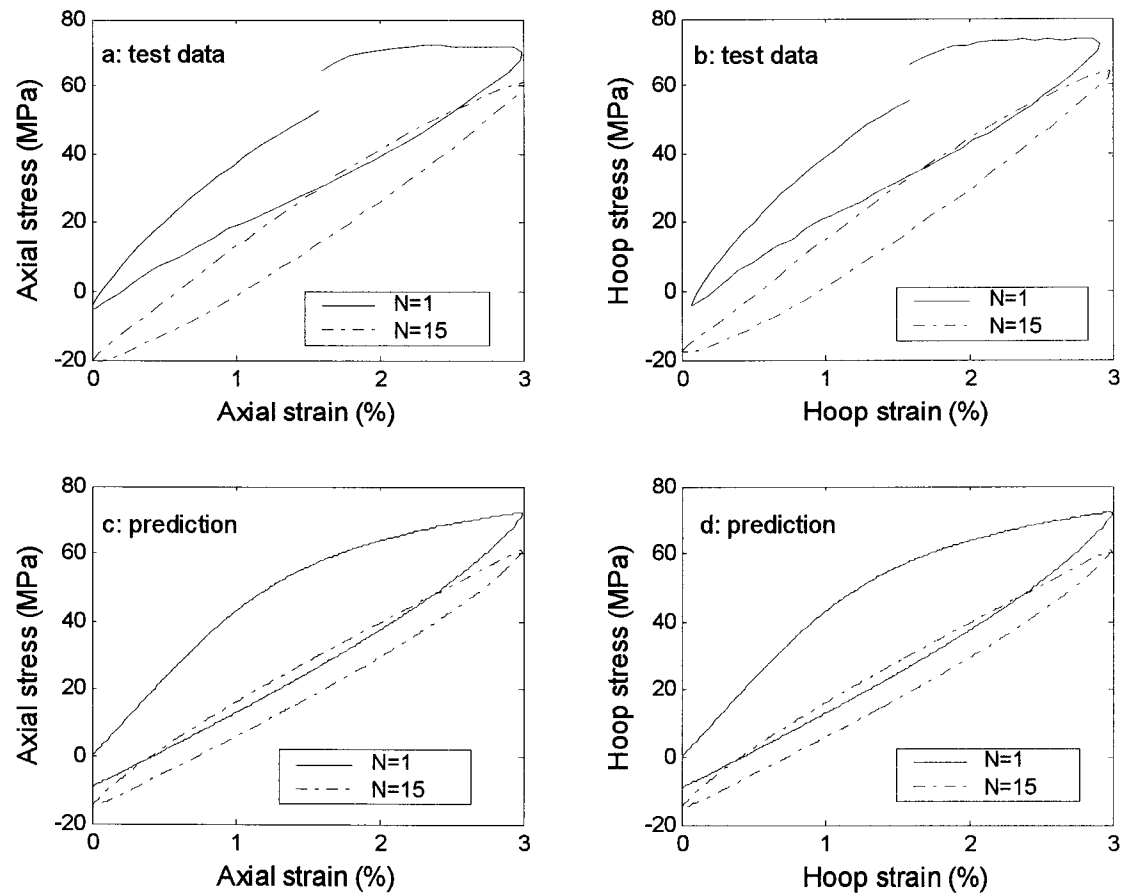


Figure 4.5 The first and the fifteenth stress-strain loops of the strain-controlled proportional (equi-biaxial) cyclic loading with strain range of $\Delta\varepsilon_a = \Delta\varepsilon_h = 3\%$: (a) experimental axial stress-strain loops, (b) experimental hoop stress-strain loops, (c) predicted axial stress-strain loops and (d) predicted hoop stress-strain loops

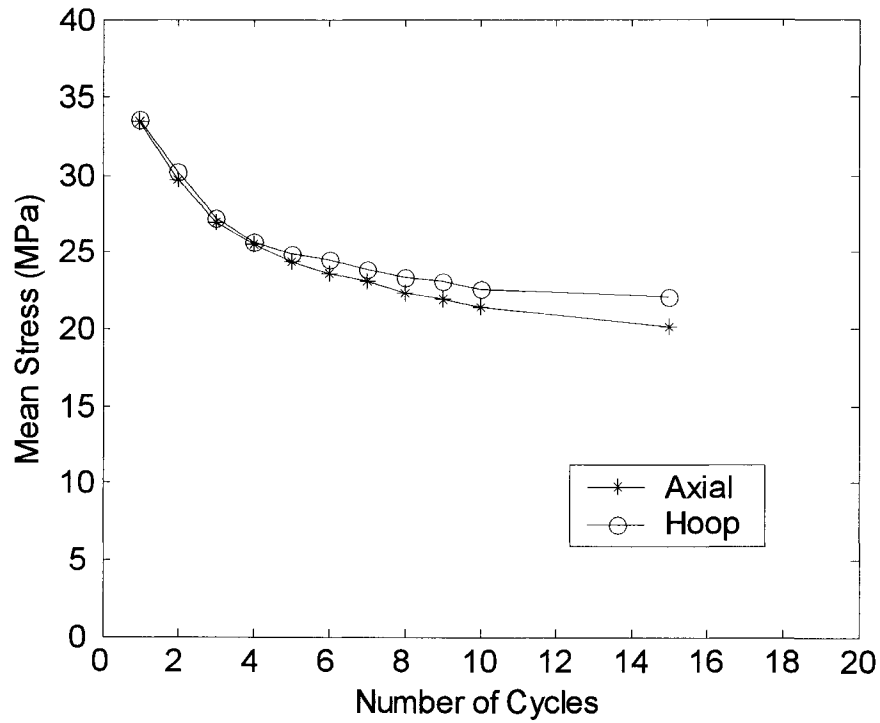


Figure 4.6 Mean stress relaxation vs. number of cycles for the strain-controlled proportional (equi-biaxial) cyclic loading with strain range of $\Delta\varepsilon_a = \Delta\varepsilon_h = 3\%$. Asterisk solid line: axial mean stress relaxation. Circle solid line: hoop mean stress relaxation

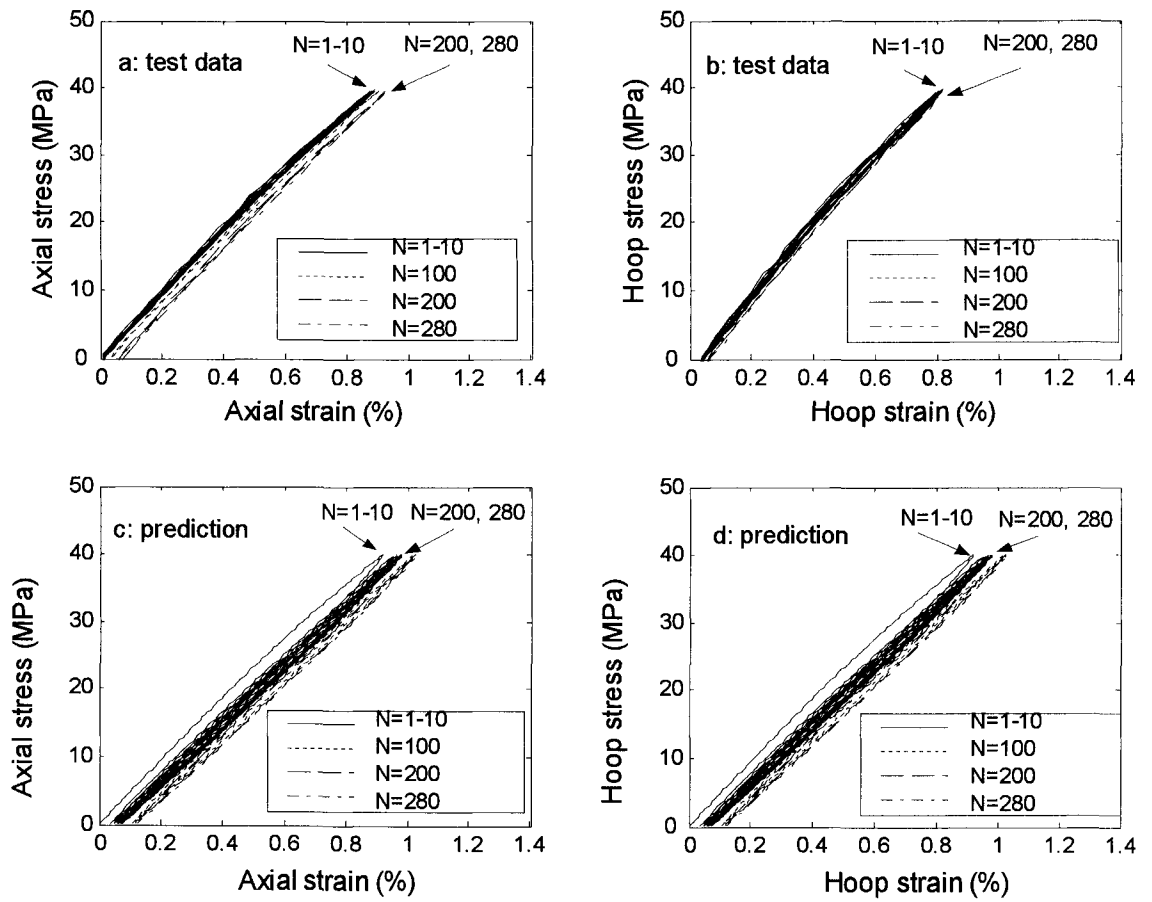


Figure 4.7 Stress-controlled proportional (equi-biaxial) cyclic loading with stress range of $\Delta\sigma_a = \Delta\sigma_h = 40\text{MPa}$: (a) experimental axial stress-strain response, (b) experimental hoop stress-strain response, (c) predicted axial stress-strain response and (d) predicted hoop stress-strain response

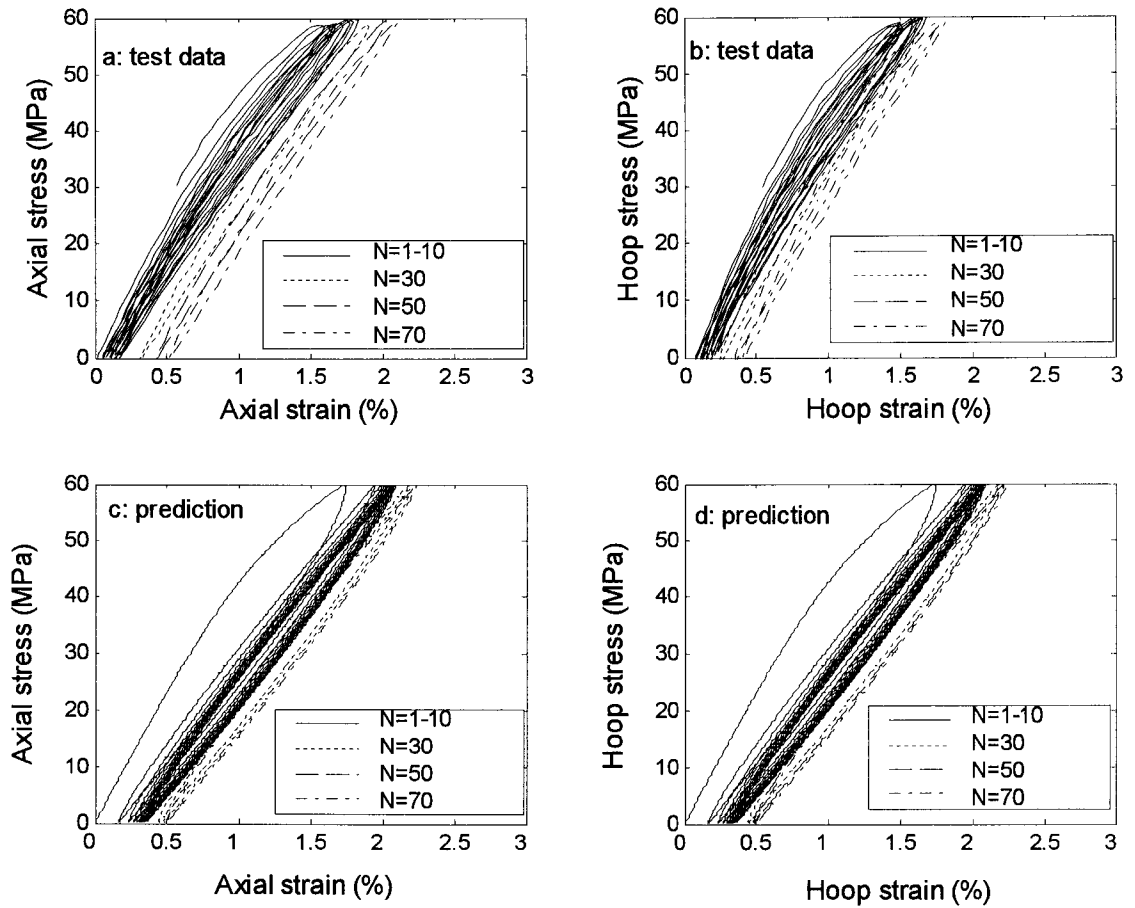


Figure 4.8 Stress-controlled proportional (equi-biaxial) cyclic loading with stress range of $\Delta\sigma_a = \Delta\sigma_h = 60\text{MPa}$: (a) experimental axial stress-strain response, (b) experimental hoop stress-strain response, (c) predicted axial stress-strain response and (d) predicted hoop stress-strain response

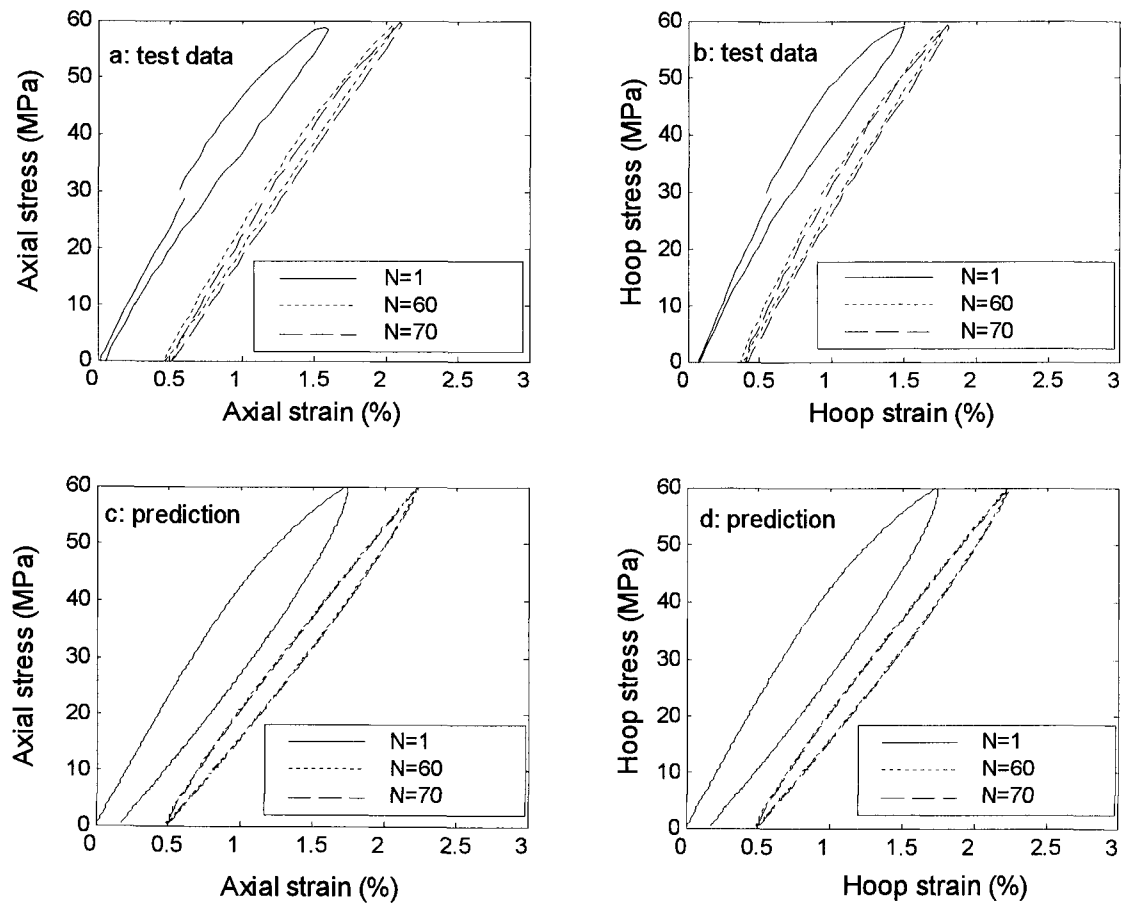


Figure 4.9 The first, the sixtieth and the seventieth hysteresis loops of stress-controlled proportional (equi-biaxial) cyclic loading with stress range of $\Delta\sigma_a = \Delta\sigma_h = 60\text{MPa}$: (a) experimental axial stress-strain loops, (b) experimental hoop stress-strain loops, (c) predicted axial stress-strain loops and (d) predicted hoop stress-strain loops

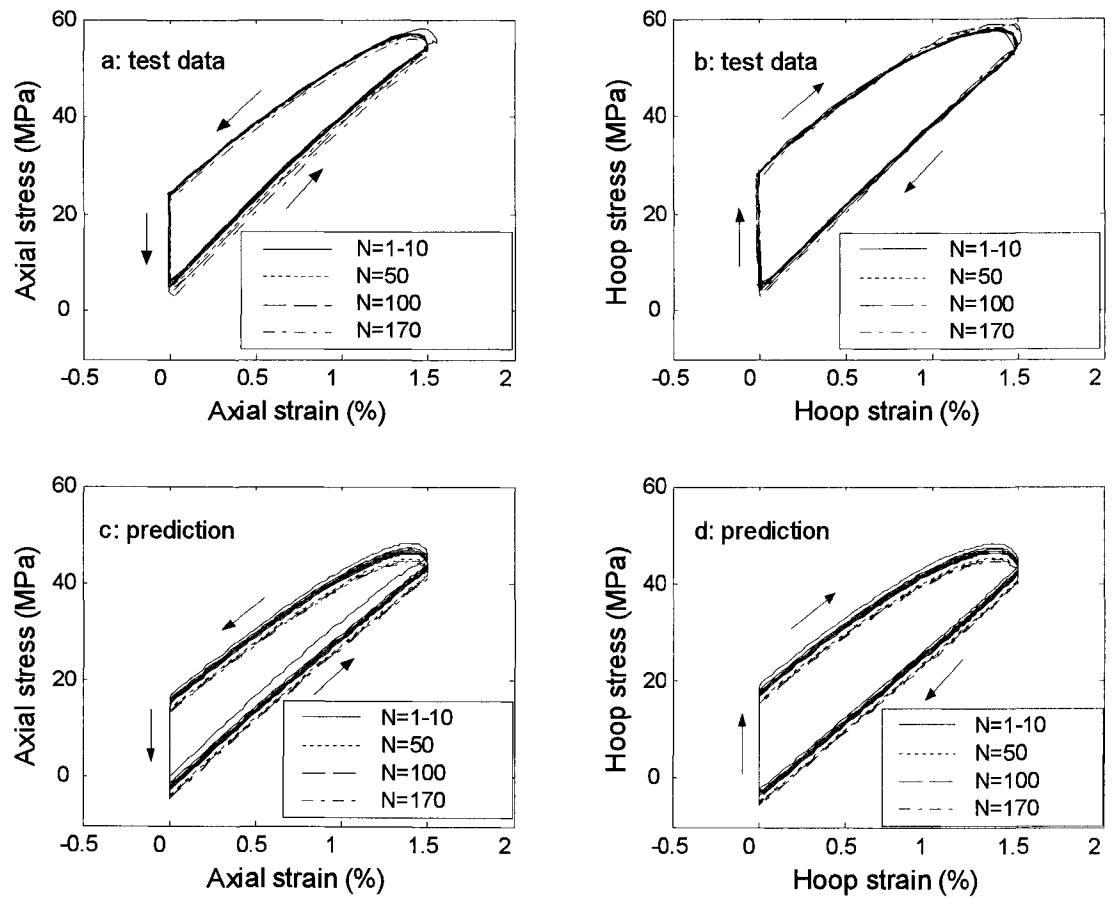


Figure 4.10 Strain-controlled non-proportional quarter-circle sectorial cyclic loading with strain range of $\Delta\varepsilon_a = \Delta\varepsilon_h = 1.5\%$: (a) experimental axial stress-strain response, (b) experimental hoop stress-strain response, (c) predicted axial stress-strain response and (d) predicted hoop stress-strain response

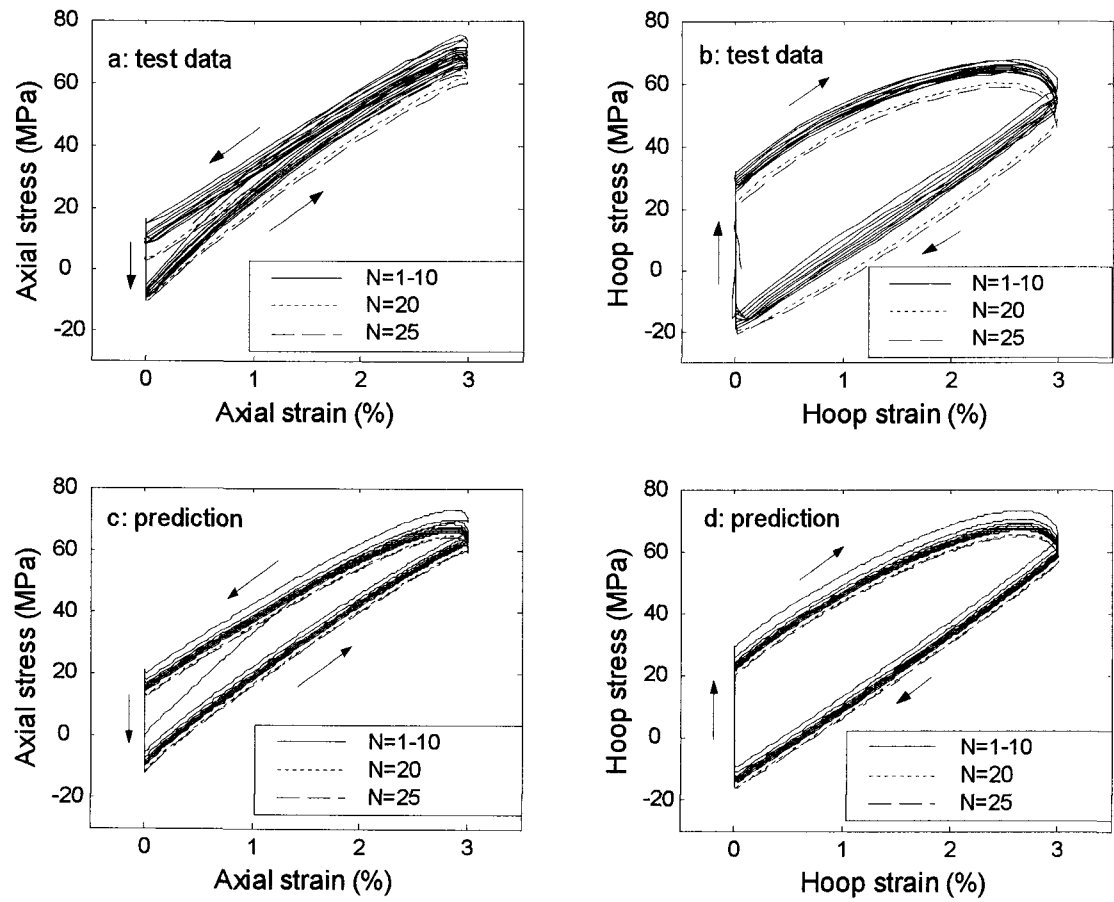


Figure 4.11 Strain-controlled non-proportional quarter-circle sectorial cyclic loading with strain range of $\Delta\varepsilon_a = \Delta\varepsilon_h = 3\%$: (a) experimental axial stress-strain response, (b) experimental hoop stress-strain response, (c) predicted axial stress-strain response and (d) predicted hoop stress-strain response

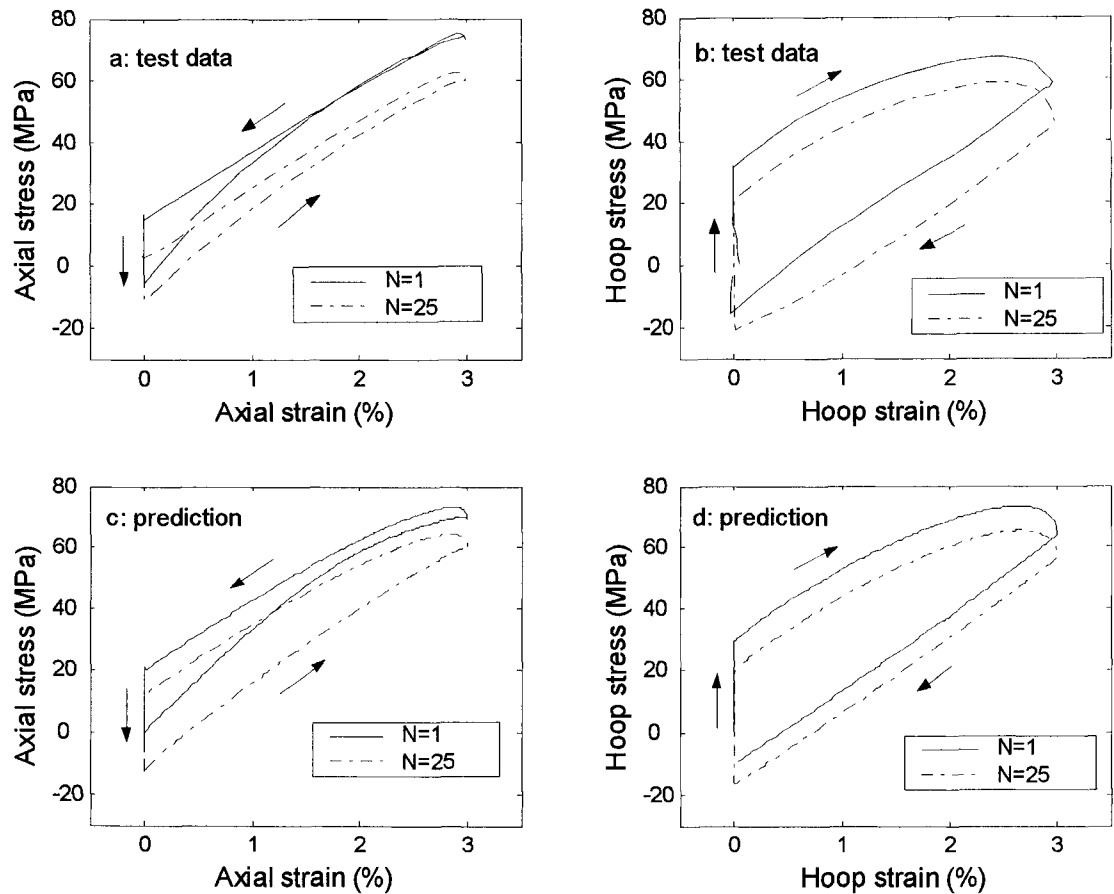


Figure 4.12 The first and the twenty-fifth hysteresis loops of strain-controlled non-proportional quarter-circle sectorial cyclic loading with strain range of $\Delta\varepsilon_a = \Delta\varepsilon_h = 3\%$: (a) experimental axial stress-strain loops, (b) experimental hoop stress-strain loops, (c) predicted axial stress-strain loops and (d) predicted hoop stress-strain loops

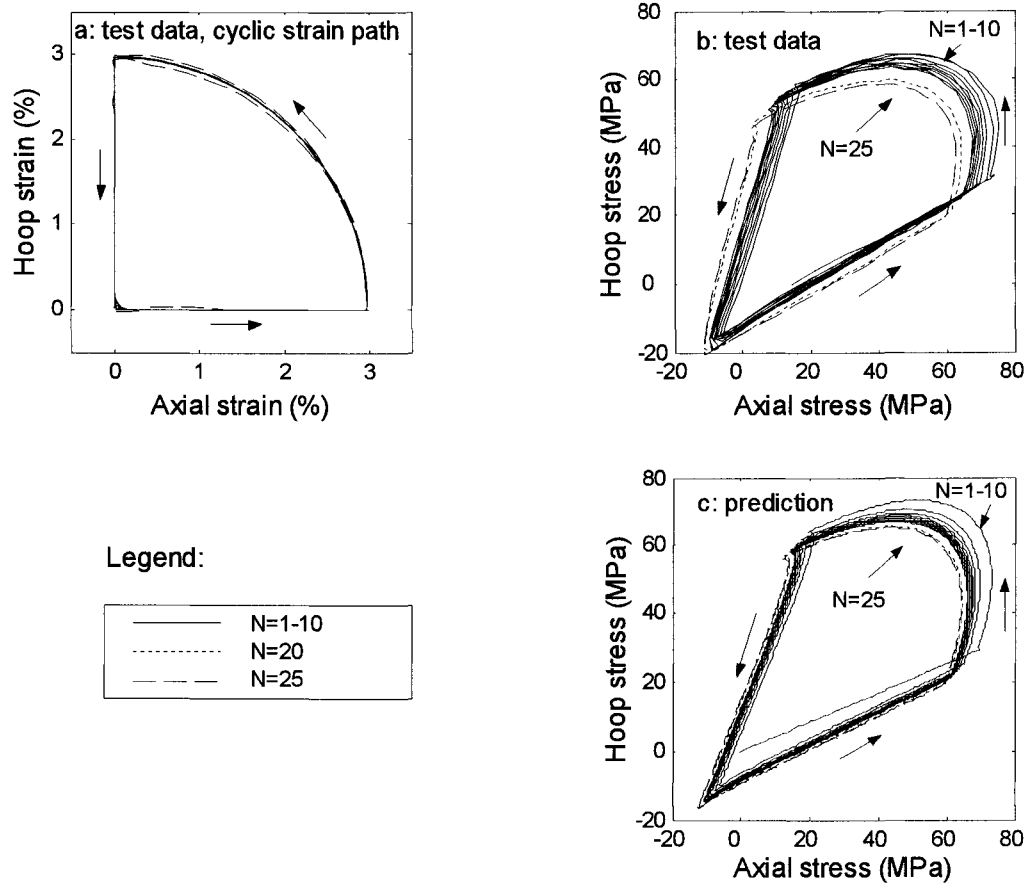


Figure 4.13 Strain-controlled non-proportional quarter-circle sectorial cyclic loading with strain range of $\Delta\varepsilon_a = \Delta\varepsilon_h = 1.5\%$: (a) experimental cyclic strain path, (b) experimental stress response and (c) predicted stress response

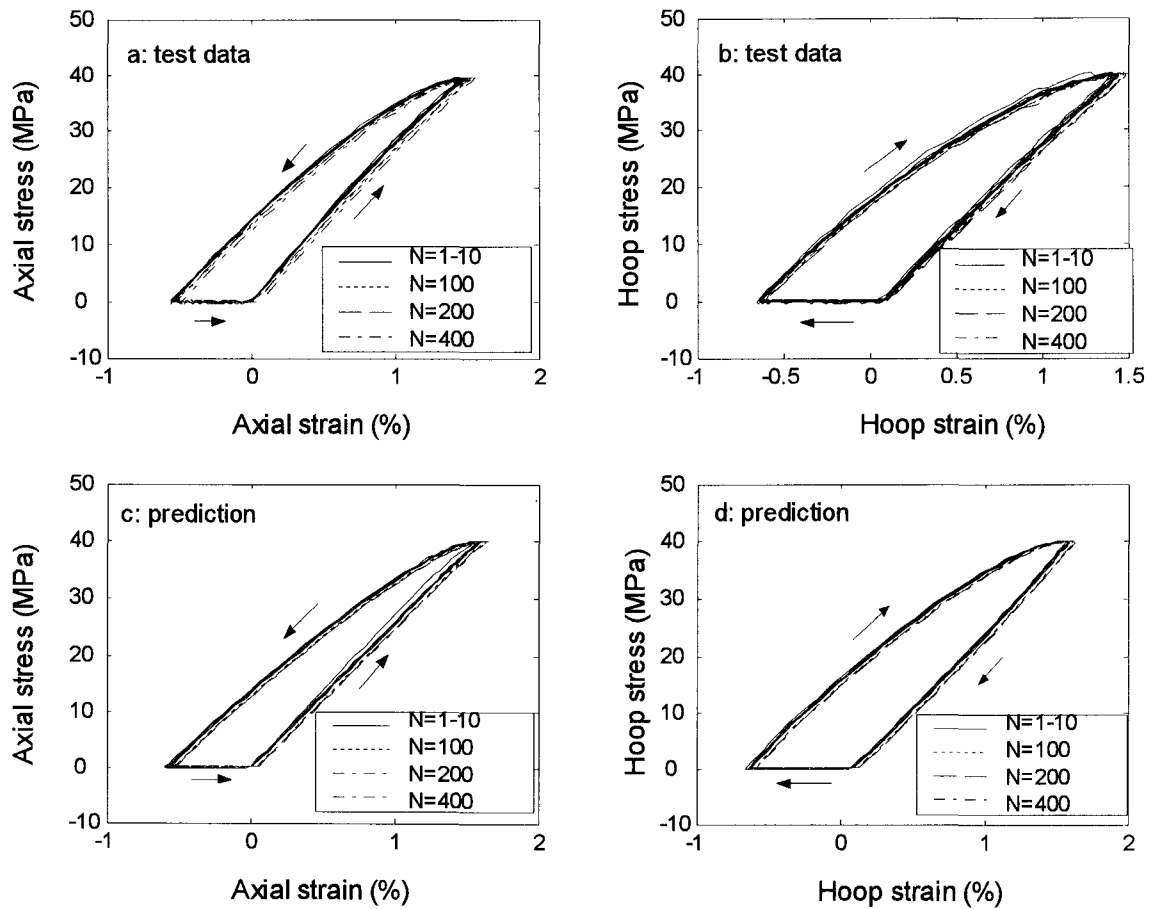


Figure 4.14 Stress-controlled non-proportional quarter-circle sectorial cyclic loading with stress range of $\Delta\sigma_a = \Delta\sigma_h = 40\text{MPa}$: (a) experimental axial stress-strain response, (b) experimental hoop stress-strain response, (c) predicted axial stress-strain response and (d) predicted hoop stress-strain response

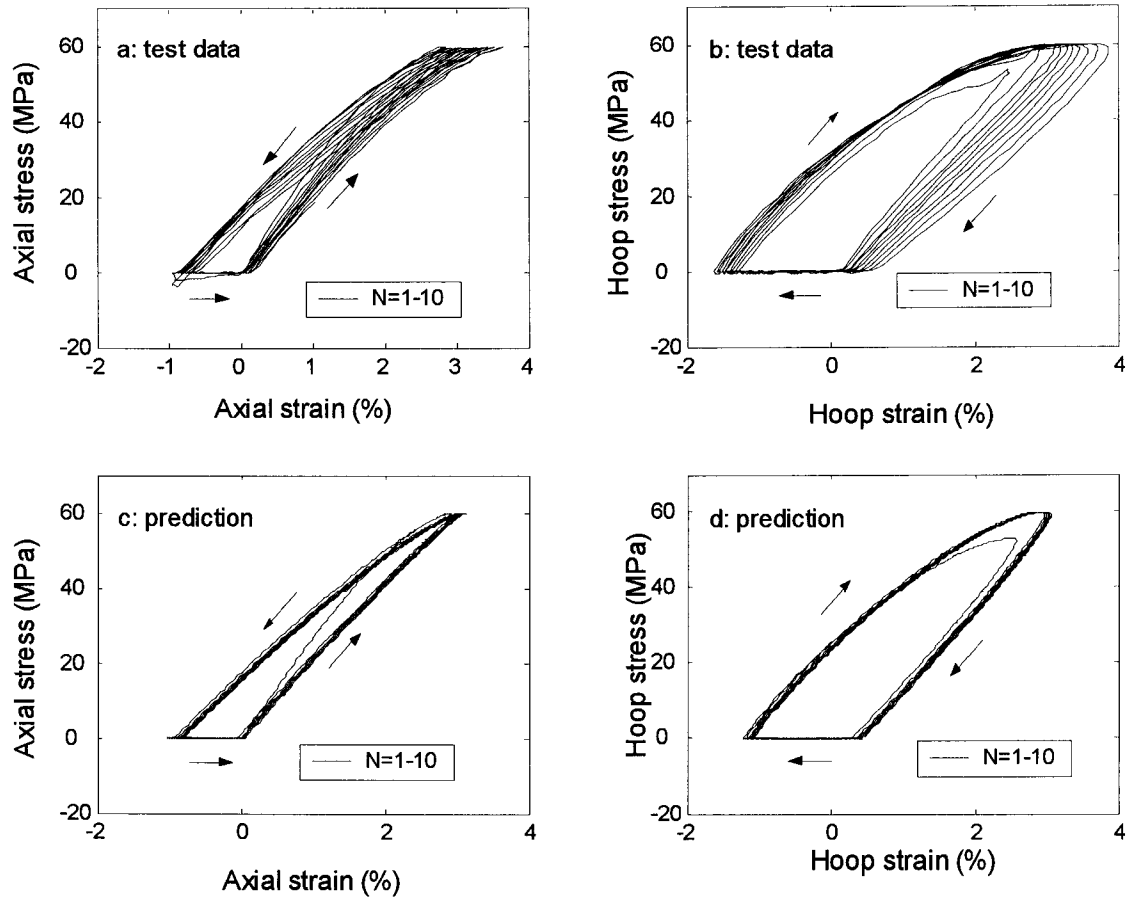


Figure 4.15 Stress-controlled non-proportional quarter-circle sectorial cyclic loading with stress range of $\Delta\sigma_a = \Delta\sigma_h = 60\text{MPa}$: (a) experimental axial stress-strain response, (b) experimental hoop stress-strain response and (c) predicted axial stress-strain response, (d) predicted hoop stress-strain response

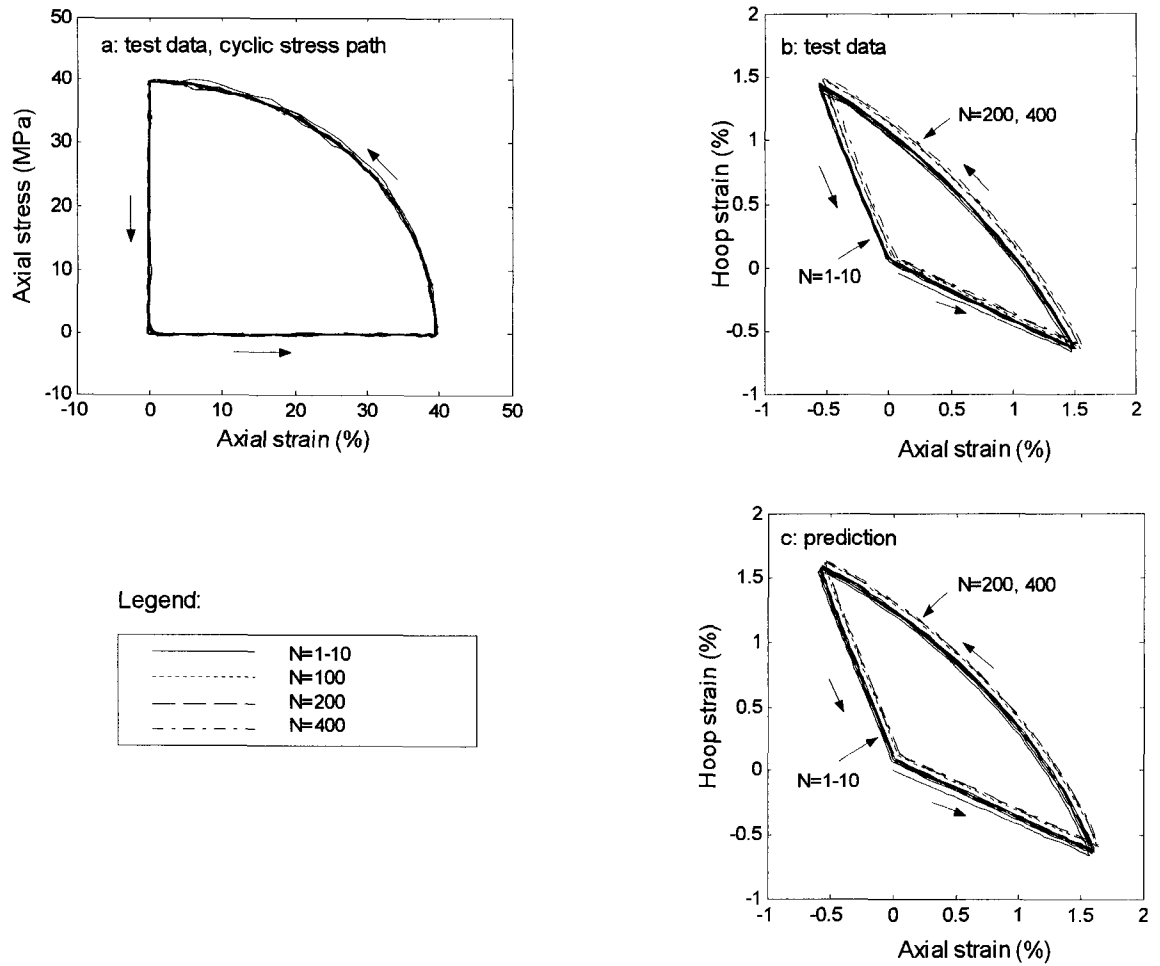


Figure 4.16 Stress-controlled non-proportional quarter-circle sectorial cyclic loading with stress range of $\Delta\sigma_a = \Delta\sigma_h = 40MPa$: (a) experimental cyclic stress path, (b) experimental strain response and (c) predicted strain response

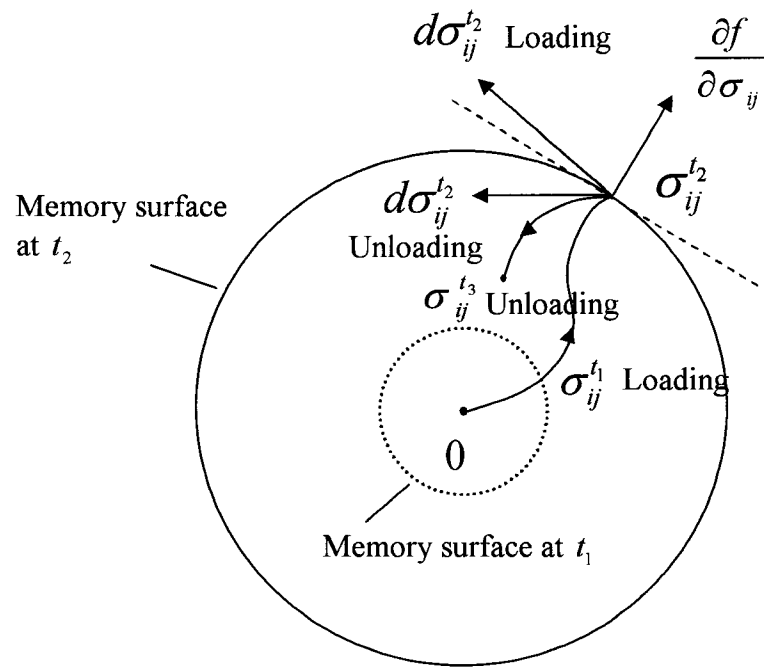


Fig. 17 Schematic representation of a current memory surface and the loading/unloading criterion

Bibliography

1. K. W. Loh, A. A. O. Tay and S. H. Teoh, Effect of constitutive models on the numerical simulation of viscoelastic flow at an entry region. *Polym. Eng. Sci.*, **36**, 1990 (1996).
2. Ocsuki, T. Kajiwara and K. Funatsu, Numerical simulation of annular extrudate swell using various types of viscoelastic models. *Polym. Eng. Sci.*, **39**, 1969 (1999).
3. Z. Xia, Y. Hu and F. Ellyin, Deformation behavior of an epoxy resin subject to multiaxial loadings. Part II: constitutive modeling and predictions. *Polym. Eng. Sci.*, **43**, 734 (2003).
4. C. Zhang and I. D. Moore, Nonlinear mechanical response of high density polyethylene, Part II : uniaxial constitutive modeling. *Polym. Eng. Sci.*, **37**, 414 (1997).
5. J. Lai and A Bakker, 3-D schapery representation for non-linear viscoelasticity and finite element implementation, *Comput. Mech.*, **18**, 182 (1996).
6. A. D. Drozdov and A. L. Kalamkarov, A constitutive model for non-linear viscoelastic behavior of polymers. *Polym. Eng. Sci.*, **36**, 1907 (1996).
7. R. A. Schapery, Nonlinear viscoelastic solids. *Int. J. Solids & Structures*, **37**, 359 (2000).
8. Y. Hu, Z. Xia and F. Ellyin, Deformation behavior of an epoxy resin subject to multiaxial loadings. Part I: experimental investigations. *Polym. Eng. Sci.*, **43**, 721 (2003).
9. X. Shen, Z. Xia and F. Ellyin, Cyclic deformation behavior of an epoxy polymer, Part I: experimental investigations. Submitted to *Polym. Eng. Sci.*.
10. Y. Jiang and H. Sehitoglu, Cyclic ratcheting of 1070 steel under multiaxial stress state. *Int. J. Plast.*, **10**, 579 (1994).
11. Z. Xia and F. Ellyin, Nonproportional multiaxial cyclic loading: experiments and constitute modeling. *J. Appl. Mech.*, **58**, 317 (1991).
12. G. Meijer Z. Xia and F. Ellyin, Biaxial cyclic analysis of $Al_2O_3/p - 6061 Al$ composite. *Acta mater.*, **45**, 3237 (1997).
13. S. Rabinowitz and P. Beardmore, Cyclic deformation and fracture of polymers. *J. Mater. Sci.*, **9**, 81 (1974).
14. D. J. Kizypow and C. M. Rimnac, Cyclic steady state stress-strain behavior of UHMW polyethylene. *Biomaterials*, **21**, 2081 (2000).

-
15. T. Ariyama, Cyclic deformation and relaxation characteristics in polypropylene. *Polym. Eng. Sci.*, **33**, 18 (1993).
 16. R. J. Scavuzzo, Oscillating stress on viscoelastic behavior of thermoplastic polymers. *J. Press. Vesel Tech.*, **122**, 386 (2000).
 17. F. Ellyin, *Fatigue Damage, Crack Growth, and Life Prediction*, Chapman & Hall, London, UK, Chapter 5. (1997).
 18. Z. Xia, X. Shen and F. Ellyin, Cyclic deformation behavior of an epoxy polymer, Part II: Predictions of Viscoelastic Constitutive Models. Submitted to *Polym. Eng. Sci.*.

Chapter 5

Conclusions

The primary objective of the present study was to investigate the cyclic deformation behavior of Epon 826/Epi-Cure 9551 resin system. Both uniaxial and biaxial cyclic tests were carried out through a comprehensive experimental program, which was designed to study the material's viscoelastic behavior, such as the amplitude- and rate-dependent behavior, mean stress/strain effect, loading mode effect, loading path effect, and the influence of multiaxial loading. The test results were further used to validate and/or compare the predictive capabilities of viscoelastic constitutive models.

Uniaxial cyclic tests were carried out on solid cylindrical specimens. The tests included stress-controlled cyclic loading with/without mean stress and strain-controlled cyclic tests with mean strain at various amplitudes and loading rates. Cyclic creep strain and anisotropy in cyclic tension and compression were also investigated. Experimental results reveal that:

- The cyclic stress-strain response of this material was amplitude dependent. The material showed a linear response at a low stress level. A nonlinear stress-strain hysteresis loop was observed at high cyclic stress levels and the nonlinearity was usually more pronounced in the first loading cycle. With increasing cycles,

hysteresis loops became slimmer and less nonlinear except at very high stress levels.

- The stress-strain loops were different at different loading rates. With increasing loading rates, the stress-strain response became less nonlinear which resulted in less accumulated ratcheting strain and more stable stress-strain response
- For stress-controlled cyclic loading with mean stress, ratcheting strain is accumulated, which was of a viscoelastic nature and this is confirmed by its full recovery after load removal. For strain-controlled cyclic loading with mean strain, the mean stress relaxation occurred, which contributed to the observed longer life in comparison to the stress-controlled cyclic loading with mean stress.
- Anisotropic response to tensile and compressive cyclic loading was noted. It was found that the material showed a better creep resistance in compression than in tension

The uniaxial cyclic test data were used to evaluate the predictive capabilities of two viscoelastic constitutive models. One of the models was in differential form and the other in integral form. Very few studies are available in the literature concerning the prediction of cyclic deformation of epoxy polymers. It was found that the differential model with a general rule to delineate the loading and unloading simulated well the experimental observations. In contrast, the integral model predicts the unloading case with a trend that was contrary to that observed experimentally. This was particularly evident when the applied cyclic stress/strain were high, which resulted in nonlinear behavior. The differential model was capable of simulating most experimental

observations both qualitatively and quantitatively. The integral model was able to predict general trends of the deformation behavior, such as ratcheting deformation under stress-controlled cyclic loading with a mean stress and mean stress relaxation under strain-controlled cyclic loading with mean strain; however, it could not correctly simulate the unloading behavior. Quantitative comparison with experimental data also revealed that the integral model predictions were not as good as that by the differential model.

Biaxial (proportional and non-proportional) cyclic tests were conducted on thin-walled tubular specimens. The focus was placed on the biaxial stress-strain response and their dependency on the load control mode, stress or strain range and loading path. Experimental results indicated that under strain-controlled equi-biaxial (proportional) cyclic loading, mean stress relaxation occurred in both axial and hoop directions; the mean stress of the cyclic straining as well as the hysteresis loops reached a stable state with increasing number of cycles. Under stress-controlled equi-biaxial cyclic loading, ratcheting strains accumulated in both principal directions. The ratcheting rate decreased with the increasing number of cycles and the hysteresis loops become slimmer and less nonlinear until the attainment of a cyclic stable state.

When the material was subjected to non-proportional cyclic loading, anisotropy in stress-strain responses was induced in both axial and hoop directions, and the axial and hoop hysteresis loops rotated in opposite directions. This was particularly evident at high stress or strain levels. Under strain-controlled non-proportional cyclic loading, the uncontrolled stress components gradually decreased in magnitude with the increasing

number of cycles. They asymptotically reached a stable level after certain number of cycles. Under stress-controlled non-proportional cyclic loading, a mean stress relaxation occurred in both axial and hoop directions.

The experimental results were further used to validate the predictive capabilities of the nonlinear differential viscoelastic constitutive model. Qualitative and quantitative comparison with the test data indicated a good agreement in predicting the complex stress-strain response under biaxial cyclic loading with various loading paths, applied stress or strain ranges and loading control modes.

Appendix

Differential model constants and functions:

$$E = 2800 \text{ MPa}, \nu = 0.42, \alpha = 10, \tau_1 = 6.116 \text{ s}, R = 1.15, n = 6 \text{ and}$$

$$E_1(\sigma_{eq}) = 1.055 \times 10^5 e^{\frac{\sigma_{eq} - 22.764}{18.000}} \text{ MPa}$$

Integral model constants and functions:

$$D_0 = 2.86 \times 10^{-4} (\text{MPa})^{-1}, D_1 = 9.819 \times 10^{-6} (\text{MPa})^{-1}, n = 0.145$$

$$g_i = C_i + A_i \left(\frac{\sigma}{\sigma_0} \right)^{B_i} \quad (i = 0, 1, 2)$$

$$a_\sigma = \begin{cases} 1 & \text{for } \sigma \leq \sigma_1 \\ C_\sigma + A_\sigma e^{-\frac{\sigma - \sigma_1}{B_\sigma}} & \text{for } \sigma > \sigma_1 \end{cases}$$

$$C_0 = 1.0, \quad A_0 = 0.3250, \quad B_0 = 4.462$$

$$C_1 = 1.0, \quad A_1 = 2.6629, \quad B_1 = 2.047$$

$$C_2 = 1.0, \quad A_2 = 3.7015, \quad B_2 = 2.947$$

$$C_\sigma = 0.2097, \quad A_\sigma = 0.7901, \quad B_\sigma = 13.845$$

$$\sigma_0 = 80.0 \quad \sigma_1 = 18.97$$